

Atomistic Modeling of Processing Issues for Transparent Polycrystalline Alumina

THÈSE N° 6019 (2013)

PRÉSENTÉE LE 29 NOVEMBRE 2013

À LA FACULTÉ DES SCIENCES ET TECHNIQUES DE L'INGÉNIEUR
LABORATOIRE DE TECHNOLOGIE DES POUDRES
PROGRAMME DOCTORAL EN SCIENCE ET GÉNIE DES MATÉRIAUX

ÉCOLE POLYTECHNIQUE FÉDÉRALE DE LAUSANNE

POUR L'OBTENTION DU GRADE DE DOCTEUR ÈS SCIENCES

PAR

Abhishek TEWARI

acceptée sur proposition du jury:

Prof. K. Scrivener, présidente du jury
Dr P. Bowen, directeur de thèse
Dr U. Aschauer, rapporteur
Prof. N. Marzari, rapporteur
Prof. S. Parker, rapporteur



ÉCOLE POLYTECHNIQUE
FÉDÉRALE DE LAUSANNE

Suisse
2013

Dedicated to my parents

Happiness is the only motivation in life.

Acknowledgements

गुरुर्ब्रह्मा गुरुर्विष्णु गुरुर्देवो महेश्वरः ।

गुरु साक्षात् परब्रह्म तस्मै श्री गुरुवे नमः ॥

(The Guru is Brahma (the creator), Lord Vishnu (the preserver), and Lord Shiva (the destroyer). To that very Guru I bow, for He is the Supreme Being, right before my eyes.)

First of all, I would like to thank my thesis director and guru Dr. Paul Bowen. He has been a great source of motivation and encouragement during the course of my entire thesis. I cherish the freedom of experimentation and flexibility of working, which I got with him. I always enjoyed his pragmatic approach towards science as well as numerous interesting discussions we had on sports and life in general. I am also thankful to him for supporting me to go to various conferences and to collaborate with different groups.

I would also like to thank my thesis jury members for examining my thesis and giving useful feedback and comments to improve my thesis and gain further insights into my work.

I would also like to thank my colleague and friend Sandra Galmarini for being a continuous support during my thesis. Critical discussion with her always helped me refine my work. It was a pleasure to work with Dr. Uli Aschauer on various topics during my PhD thesis, who helped me learning new simulation methods. I would also like to thank Prof. Steve Parker for welcoming me at University of Bath and getting me started with general grain boundary calculations.

I am also grateful to Prof. Hofmann and Prof. Jacques Lemaitre for welcoming me at LTP and providing a very conducive environment for research at LTP, and our lab secretary Ruth Gacoin who made the administrative work much easier.

The experience of the PhD would have been much lesser if not for the wonderful friends and colleagues I met at LTP. Arthur, Henning, Lionel, Gaby, Kat, June, Vianney, Piyak, Vanessa, Goldy, Saso, Sandra all made my PhD stay at LTP more enriching and joyous. I think numerous discussions over lunch and coffee breaks ranging from science, economics and politics to society and religion have helped me broaden my outlook about life in general.

I also consider myself fortunate to have wonderful friends around me. Big thanks to my best friends Paula, Nishanth and Kat for being there to share my life in happy as well as depressing moments. I have learnt lots of important lessons to face the

Acknowledgements

situations in life thanks to them. Ram, Suri, Soni, Devika, Swati are few other names, which I can not forget to mention here. Being so far away from home, it was very nice to have such a vibrant and active Indian community at EPFL. The events and festivals celebrated by Indian association at EPFL made us miss the home less on those important occasions.

I would also like to thank my spiritual guru Shri Ganesh Bagaria for initiating the curiosity within me to understand myself better. The knowledge I have gained from him has helped me set my priorities in life straight and better understanding of human values and relationships.

Last but not the least by any means, I would like to express my highest gratitude to my parents and my family. The hardships and difficulties my late father and my mother went through to provide me the best possible education is the reason that I am where I am today. I can never thank them enough for their unconditional love and support. The kind of confidence and belief my family had in me has always pushed me to do my best in my endeavor to be a better human being.

I am sure there might be many more people to thank. I am sorry if I have forgotten to mention them here.

Lausanne, 18 Novemeber 2013

Abstract

Transparent polycrystalline alumina has many possible promising areas of application from jewelry and the watch industry to wave guides, energy economical lamp envelopes, and optical windows. Ultrahigh density, submicron sized grains and/or oriented microstructures have been identified as the key requirements to synthesize transparent alumina. The highest real inline transmittance (RIT) aluminas reported in the literature are still not good enough to be used for transparent applications.

The goal of the present thesis was to use atomistic modeling to understand the basic mechanisms of the physical/chemical phenomena involved in the various issues pertaining the processing of transparent alumina. The three main issues which were addressed in the present work are: segregation of cation-dopants/anion-impurities to the alumina interfaces, solid state oxygen diffusion in alumina, and adsorption of polymers on alumina surfaces.

Doping of alumina with transition elements (e.g. Y, Mg, La) has been used in the literature for grain growth reduction and creep enhancement. Codoping with a combination of dopants (e.g. Mg-La) has been reported to be more effective. However the atomistic level effects of codoping on alumina microstructure and hence on properties are not very well understood. The energy minimization method was used to calculate the segregation energies and the relaxed atomistic structures of as many as 9 codoped (Y-La, Mg-La, Mg-Y) surfaces and twin grain boundaries (GBs). Only codoping with a combination of bivalent-trivalent (Mg-La and Mg-Y) dopants was found to be energetically more favorable than single doping. Disparity in the ionic sizes was identified as the key reason for the favorable codoping with Mg. Effects of the dopants type and concentration on the GB atomistic structures have been discussed in the light of the GB complexion transitions and GB packing. Coordination number calculations were made to analyze the GB chemical environment.

The existence of anion impurities such as chlorides and sulphates in industrial alumina powder synthesis is well known. But its effects on the processing of alumina ceramics have been grossly neglected. Energy minimization calculations showed that the segregation of Cl is 4-6 times stronger than the cation dopants. Cl-Al coordination number analysis suggests strong adhesion of Cl on the powder surface, making the removal of Cl ions difficult at low temperatures.

Oxygen diffusion plays an important role in grain growth and densification during the sintering of alumina ceramics and governs high temperature processes such as creep. The atomistic mechanism for oxygen diffusion in alumina is however still debated. The calculations are usually performed for perfectly pure crystals, whereas virtually every experimental alumina sample contains a significant fraction of impurity/dopants ions. In the present study atomistic defect cluster and nudged elastic band calculations have been used to model the effect of Mg impurities/dopants on defect binding energies and migration barriers. It was found that oxygen vacancies can form energetically favorable clusters with Mg, which reduces the number of mobile species. Moreover diffusive jumps leading away from Mg have migration energies up to twice the value in pure alumina, whereas those approaching Mg are lowered by up to a factor of four, which will slow down the kinetics of diffusion. Other effects of Mg such as vacancy destabilization and the vacancy-vacancy interactions have also been discussed in detail.

Majority of the computational segregation studies are done on the highly symmetrical twin grain boundaries. However, the fraction of special twin grain boundaries found in sintered alumina samples is reported to be very small. Therefore, to fulfill the ultimate goal of the simulations, i.e. linking the simulations with the experiments, experimentally characterized general GBs were simulated using near coincidence GB approach and the energy minimization method. Although the segregation of Y was found to be energetically favorable, dopants were found to be occupying only 25% cation sites on the GB. GB complexion phases, which are less favorable to grain growth reduction, were found to be more probable on the general GBs in contrast to the twin GBs.

Controlling the agglomeration of ultrafine powders is a big challenge in the processing of nano scaled ceramics. Understanding of the conformation of adsorbed dispersants and the interplay of the adsorption with powder surface characteristics is still limited and requires further work on a rather fundamental level. The present thesis could not address this issue in detail due to the unavailability of an adequate force field. The preliminary results on the development of such a force field as well as the progress made so far are discussed in the last chapter of the thesis.

The present thesis helps understand basic fundamental issues pertaining to the processing-microstructure-property relationship in transparent alumina which should help overcome the major roadblocks in the progress of the field of transparent alumina ceramics. The work is generic and the methods can be successfully applied to other ceramic systems.

Keywords: Atomistic modeling, alumina, segregation, defects, impurities, diffusion.

Résumé

L'Alumine polycristalline transparente a de nombreux domaines d'application possibles prometteurs allant des bijoux à l'industrie horlogère en passant par les guides d'ondes, les enveloppes des lampes à économie d'énergie ou les fenêtres optiques. L'ultra densité, les grains de tailles submicroniques et / ou les microstructures orientées ont été identifiés comme les besoins principaux pour synthétiser de l'alumine transparente. Les plus hautes valeurs de transmittance (RIT) des aluminés rapportées dans la littérature ne sont pas encore assez bonnes pour être utilisées pour des applications transparentes.

L'objectif de cette thèse a donc été d'utiliser la modélisation atomistique pour comprendre les mécanismes de base des phénomènes physicochimiques impliqués dans les diverses questions relatives au traitement de l'alumine transparente. Les trois principales questions qui ont été abordées dans le présent ouvrage sont: la ségrégation des dopants-cationiques/impuretés-anioniques aux interfaces de l'alumine, l'état de diffusion de l'oxygène dans l'alumine à l'état solide et l'adsorption des polymères sur des surfaces d'alumine.

Le dopage de l'alumine avec des éléments de transition (par exemple Y, Mg, La) sont utilisés pour la réduction de la croissance des grains et de l'amélioration du fluage. Le co-dopage avec une combinaison de dopants (par exemple Mg-La) semble être la plus efficace. Toutefois, les effets des co-dopages, au niveau atomistique, sur la microstructure d'alumine et donc sur ses propriétés ne sont pas très bien comprises. La méthode de minimisation de l'énergie a été utilisée pour calculer les énergies de ségrégation et les structures atomiques détendues de 9 surfaces co-dopées (Y-La, Mg-La, Mg-Y) et de joints de grains miroirs (GBs). Le co-dopage avec seulement des combinaisons de dopants bivalents ou trivalents (Mg-La et Mg-Y) a démontré être énergétiquement plus favorable que le dopage unique. La raison principale de l'efficacité d'un co-dopage au Mg semble être la disparité des tailles ioniques. Les effets du type de dopants et de leur concentration sur les structures atomiques ont été discutés par les transitions de complexion et de compactage des GBs. Des calculs de nombres de coordination analysèrent l'environnement chimique des GBs.

L'existence d'impuretés anioniques telles que les chlorures et les sulfates dans la synthèse industrielle de poudre d'alumine est bien connue. Mais ses effets sur le traitement des céramiques d'alumine sont mal compris. Des calculs de minimisation de l'énergie ont montré que la ségrégation des Cl est 4 à 6 fois plus forte que les dopages cationiques. L'analyse du nombre de coordination Cl-Al suggère une forte adhérence des Cl sur la surface de la poudre, rendant leur élimination difficile.

La diffusion de l'oxygène joue un rôle important dans la croissance et la densification des grains lors du frittage des alumines régissant les processus à haute température tel que le fluage. Le mécanisme atomistique de diffusion de l'oxygène dans l'alumine est cependant toujours débattu. Les calculs sont généralement effectués pour des cristaux parfaitement purs, alors que pratiquement tous les échantillons expérimentaux d'alumine contiennent une fraction importante d'impuretés ou d'ions de dopants. Dans cette étude, des clusters de défaut atomiques et des calculs sur les liaisons élastiques ont été utilisés pour modéliser l'effet des impuretés de Mg / dopants sur les défauts d'énergies de liaison et les obstacles de migration. Il a été constaté que les lacunes d'oxygène peuvent former avec le Mg des amas énergétiquement favorables réduisant le nombre d'espèces mobiles. De plus les sauts diffusants s'éloignant du Mg ont des énergies de migration deux fois plus grande que pour l'alumine pure, quand ceux s'approchant du Mg sont diminués d'un facteur quatre, ralentissant leur cinétique. D'autres effets du Mg comme la déstabilisation de lacunes et les interactions lacune - inoccupation ont été examinés.

La majorité des calculs des études de ségrégation sont effectués sur les limites symétriques de grains miroirs. Cependant, la fraction des joints de grains miroirs spéciaux dans l'alumine frittée est très faible. Par conséquent, pour atteindre l'objectif final de la simulation (relier les simulations aux expériences) des GBs caractérisés expérimentalement ont été simulés en utilisant l'approche GB de coïncidence et la méthode de minimisation de l'énergie de proximité. Bien que la ségrégation des Y s'est avéré être énergétiquement favorable, seuls 25% des sites cationiques des GBs sont occupés. Leurs phases de complexion, moins favorables à la réduction de la croissance des grains, sont plus probables sur le GBs général que sur les miroirs.

Le contrôle de l'agglomération des poudres ultrafines est un grand défi dans le traitement des nanocéramiques. La compréhension de la conformation des dispersants adsorbées et de l'interaction de l'adsorption avec les propriétés de surface est encore limitée, nécessitant des études plus fondamentales. Dans cette thèse cette question n'a pas été traitée en détail due à l'indisponibilité d'un champ de force adéquat. Les résultats préliminaires et les progrès réalisés sur l'élaboration de ce champ de force sont toutefois abordés dans le dernier chapitre.

Cette thèse permet de comprendre les facteurs fondamentaux relatifs aux relations traitement, microstructure et propriété pour l'alumine transparente permettant ainsi d'aider à surmonter les principaux obstacles à l'avancement du domaine de la céramique d'alumine transparente. Ce travail étant générique, les méthodes peuvent également être appliquées avec succès à d'autres systèmes céramiques.

Mots Clefs: Modélisation atomistique, Alumine, ségrégation, défauts, impuretés, diffusion.

Contents

1. Introduction	1
1.1. Transparent Polycrystalline Alumina	1
1.2. Light Transmission in Polycrystalline Alumina	2
1.3. Key Processing Developments	4
1.3.1. Defect free green body processing	4
1.3.2. Use of modern sintering methods and sintering aids	5
1.4. Need and Scope of the Present Thesis.....	6
1.4.1. Adsorption of dispersants on Alumina Surface.....	6
1.4.2. Grain Boundary Segregation of Dopants.....	7
1.4.3. Solid State Diffusion of Oxygen in Alumina.....	7
1.5. Objectives.....	8
2. Computational Methods.....	10
2.1. Force Field Description.....	10
2.1.1. Bonded interaction.....	11
2.1.2. Non-bonded interactions	12
2.1.2.1. Electrostatic interaction.....	13
2.1.2.2. Short Range Interactions	14
2.1.2.3. Polarisability.....	15
2.1.3. Force Filed Optimization	16
2.2. Simulation Cell Constructions	17
2.2.1. Bulk cell.....	17
2.2.2. Slab construction	17
2.2.3. Surface construction.....	19
2.2.4. Twin grain boundary construction	19
2.2.5. Near coincidence grain boundary construction	20
2.3. Energy Minimization	22
2.3.1. Steepest descent method.....	24
2.3.2. Conjugate gradient method	24
2.3.3. Newton Raphson method	25
2.4. Molecular Dynamics.....	27

2.5. Nudged Elastic Band.....	27
2.6. Metadynamics	30
2.7. Kinetic Monte Carlo.....	31
2.8. Summary of the methods used in the present work	32
3. Dopant Segregation in Codoped α -Alumina	34
3.1. Introduction.....	34
3.2. Approach	37
3.3. Theoretical Consideration	41
3.3.1. Mackrodt and Tasker formula derivation for codoping	41
3.3.2. Codoping versus single doping segregation energies	43
3.4. Results and Discussion	44
3.4.1. Segregation Energies	44
3.4.1.1. La-Y Codoping	44
3.4.1.2. Mg-La Codoping	48
3.4.1.3. Mg-Y Codoping.....	49
3.4.1.4. Cosegregation versus single dopant segregation energies.....	51
3.4.2. Interface specific segregation.....	54
3.4.3. Complexion transition with dopant concentration.....	57
3.4.4. Oxygen vacancies at the grain boundaries.....	58
3.4.5. Atomistic structure characteristics: Codoping vs. single doping.....	59
3.4.6. Coupling Effect.....	62
3.4.7. Dopant Oxygen Coordination Number.....	63
3.5. Conclusions and Outlook.....	64
4. Segregation of Anion Impurities	67
4.1. Introduction.....	67
4.2. Approach	69
4.3. Results and Discussion	70
4.3.1. Experimental evidence of Cl at GB's.....	70
4.3.2. Segregation energies (ΔH_{seg})	71
4.3.3. Interface atomistic structures	73
4.3.4. Coordination numbers.....	75
4.4. Conclusions and Outlook.....	76

5. Effect of Mg on Solid State Oxygen Diffusion	78
5.1. Introduction.....	78
5.2. Approach	81
5.2.1. Calculation of defect binding energies.....	82
5.2.2. Calculation of migration barriers.....	82
5.2.3. Calculation of diffusion coefficient.....	84
5.3. Results and Discussion	85
5.3.1. Migration barriers in pure alumina	85
5.3.2. Binding energy of oxygen vacancies.....	87
5.3.3. Effect of Mg on migration barriers	90
5.3.4. Effect of the c-axis length	92
5.3.4.1. Migration Barrier variations.....	92
5.3.4.2. Relative Changes	94
5.3.5. Vacancy destabilization	94
5.3.6. Vacancy-vacancy interaction effects	96
5.3.7. Diffusion Coefficients	97
5.4. Conclusions and Outlook.....	99
6. Linking Modeling with Experiments.....	101
6.1. Introduction.....	101
6.2. Approach	102
6.3. Results and Discussion	103
6.3.1. Microstructural characterization of grain boundaries	103
6.3.2. Segregation Energies (ΔH_{seg})	104
6.3.3. Atomistic Structures	107
6.4. Conclusions and Outlook.....	109
7. Preliminary Work: Surface Adsorption of Dispersants	110
7.1. Introduction.....	110
7.2. Approach and Implementation Issues	111
8. Conclusions & Outlook.....	114
8.1. Cation Segregation	114
8.2. Anion Segregation	116
8.3. Oxygen Diffusion	116

Contents

8.4. Outlook.....	117
A1. DFT Calculation of Migration Barriers	119
A2. Force Field Parameters	120
A2.1. Lewis-Catlow Potential for Alumina	120
A2.2. Binks Potential for Alumina	120
A2.3. PAA-Alumina-Water (TIP3P) Force Field.....	121
A2.4. PAA-Alumina-Water (De Leeuw) Force Field	130
References.....	133

List of Figures

Figure 1.1. Surfaces, grain boundaries and pores are the sources of light scattering a polycrystalline material.....	2
Figure 2.1. Schematic diagram of various types of bonded interaction potentials and their function form, (a) bonded potential, (b) angle potential, and (c) torsion potential.....	12
Figure 2.2. Functional form of two main types of non-bonded dispersion interactions, (a) Buckingham potential for Al-O and O-O pairs, and (b) typical shape of a Lenard-Jones potential	15
Figure 2.3. (a) Surface cut along the desired orientation of the slab surface, and (b) refilling of the left out atoms after the surface cut into the slab cell	18
Figure 2.4. 2-D periodic boundary conditions are applied in the surface plane of the slab and the repetition of the slab unit cell is done along the direction normal to the surface to construct a slab cell.	18
Figure 2.5. A surface cell consists of 2 regions. Atoms in the region 1 are allowed to relax, while the atoms in the region 2 are kept fixed during energy minimization. ...	19
Figure 2.6. A mirror twin grain boundary consists of 2 surfaces with the same miller index back to back and region 1 and region 2 in each block are similar as in the case of the surface cell.....	20
Figure 2.7. Schematic representation of a general grain boundary with different interplanar spacing in each grain for hexagonal systems.....	22
Figure 2.8. In steepest decent method, the search direction is normal to the force, while the conjugate gradient method mixes the previous search direction with the direction of the force to speed up the convergence [44].....	25
Figure 2.9. Newton Raphson method for energy minimization uses both the force as well as the curvature of the energy surface to find the search direction. It finds the root of the equation ($dE/dx=0$).	26
Figure 2.10. Activation energy (ΔE) for a reaction is calculated using nudged elastic band method as the difference of the energy between the saddle point state and the initial state.	28
Figure 2.11. NEB is a method to find minimum energy path for the transition from a known initial state to a known final state. The diagrams shows the various forces acting on the elastic band during energy minimization of the elastic band. [49]	29

Figure 2.12. Time evolution of the metadynamics potential. Thick solid line is the the starting potential and it is steadily filled with Gaussians (dotted lines). The dynamic evolution is labeled by the number of dynamical iterations. [51]	31
Figure 3.1. (a) single site substitution, (b) permutation of lowest energy sites for multiple dopant configurations, (c) codoping configuration as a combination of respective single dopant configurations.....	38
Figure 3.2. Comparison of probabilistic codoping with randomly chosen configurations, (a) Mg doped, (b) Y doped, and (c) La-Y doped.....	40
Figure 3.3. Representative segregation energy plots for La-Y codoped surfaces. The lines serve as visual guides only.....	46
Figure 3.4. Representative segregation energy plots for La-Y codoped GB's. The lines serve as visual guides only.	47
Figure 3.5. Representative segregation energy plots for Mg-La codoped a) (00.1) surface, b) (11.0) surface, c) (01.2) GB, d) (11.3) GB. Lines are just visual guides only.	50
Figure 3.6. Representative segregation energy plots for Mg-Y codoped, (a) (00.1) surface, (b) (11.3) surface, (c) (01.2) GB, (d) (11.1) GB. Lines are just visual guides..	52
Figure 3.7. Codoping segregation energy comparison for three doping combinations for (a) (11.1) surface, and (b) (11.1) GB. The lines are visual guides only.....	54
Figure 3.8. Interface structure dependent cosegregation and atomic arrangement of La-Y codoped α -alumina surfaces. All the atomistic structures are shown from the side view parallel to the grain boundary/surface plane with the white lines showing roughly the position of the grain boundary or surface plane. Oxygen ions are shown in red, aluminum ions in violet, Y in light blue and La in dark blue.....	56
Figure 3.9. Interface structure dependent cosegregation and atomic arrangement of La-Y codoped α -alumina grain boundaries. All the atomistic structures are shown from the side view parallel to the grain boundary/surface plane with the white lines showing roughly the position of the grain boundary or surface plane. Oxygen ions are shown in red, aluminum ions in violet, Y in light blue and La in dark blue.	57
Figure 3.10. Complexion transition in La-Y codoped (11.1) grain boundary with the increasing dopant concentration. a) 1.93 at./nm ² , b) 3.86 at./nm ² , c) 5.79 at./nm ² , d) 7.72 at./nm ² , e) 9.65 at./nm ² , f) 11.58 at./nm ² , and g) 13.51 at./nm ² . La is dark blue and Y is light blue. All the grain boundaries are viewed parallel to the GB plane. Line at the grain boundary is only a rough estimate of the grain boundary position.	59
Figure 3.11. Energetic probabilities of oxygen vacancy formation at the grain boundaries. The sites with smaller and lighter color atoms have higher probability and darkest and largest one have the least possibility. All the grain boundaries are viewed parallel to the GB plane.....	60

Figure 3.12. Formation of dopant atomic layer on Y-La codoped (01.2) grain boundary with increasing dopant concentration. Oxygen ions are shown in red, aluminum ions in violet, Y in light blue and La in dark blue.	61
Figure 3.13. Comparison of single doped and codoped (11.1) grain boundaries (a) Mg doped, (b) La doped, (c) Y- doped, (d) Mg-La codoped, (e) Mg-Y codoped, and (f) La-Y codoped (Concentration=7.74 at./nm ²). Oxygen ions are shown in red, aluminum ions in violet, Y in light blue, La in dark blue and Mg in green.	61
Figure 3.14. (11.1) Y-La codoped surface looked from the top perpendicular to the surface. Specific coordinative arrangement/coupling effect is seen, where oxygen atom is always surrounded by two different types of dopant ions.	62
Figure 4.1. STEM-EDX spectroscopy results showing the presence of Cl impurities at a grain boundary and the triple points.	71
Figure 4.2. Representative segregation energy plots for Cl segregated (a) (01.2) surface, and (b) (11.1) surface. Lines are just visual guides.	72
Figure 4.3. Representative segregation energy plots for Cl segregated (a) (01.2) GB, and (b) (11.1) GB. Lines are just visual guides.	73
Figure 4.4. Atomistic structures of the interface at their respective characteristic concentrations as mentioned in the table 2, (a) (01.2), (b) (10.0), (c) (11.1) surfaces, and (d) (11.1), (e) (10.1), (f) (01.2) GB's. All the structures are seen parallel to the interface plane. Al atoms are in pink, Oxygen in red and Cl atoms are in green.	74
Figure 4.5. Evolution of the atomistic structure of a (11.1) GB with the increasing concentration of Cl ions, (a) 2.8 at./nm ² , (b) 5.6 at./nm ² , (c) 8.3 at./nm ² , (d) 11.11 at./nm ² , and (e) 13.90 at./nm ² . All the structures are seen parallel to the grain boundary plane. Al atoms are in pink, Oxygen in red and Cl atoms are in green.	75
Figure 5.1. Migration barrier of a class III jump was calculated for 5 supercell sizes. The migration barrier is seen to be converging for a 3x3x1 supercell.	83
Figure 5.2. NEB calculations were done with 10, 20 and 30 intermediate images. Activation energy is shown to be converging with 10 intermediate images.	83
Figure 5.3. Migration barriers for the three classes of primary jumps, computed using the nudged elastic band (NEB, solid lines) and metadynamics (MTD, dashed lines) methods. For NEB the whole minimum energy pathway is given, while for MTD only the height of the saddle point is indicated.	86
Figure 5.4. Binding energy of the V _O and Mg _{Al} as a function of their distance calculated by the Mott Littleton method. The blue line is a 1/d fit to the data.	88
Figure 5.5. Binding energy of the V _O and Mg _{Al} as a function of their distance calculated by the energy minimization method.	88

Figure 5.6. Binding energy per V_O for defect clusters of one Mg_{Al} and one to four V_O . Negative values indicate energetically favorable binding.	89
Figure 5.7. Migration barriers for the diffusive jumps of oxygen vacancies as a function of the initial distance of the oxygen vacancy from Mg for primary jumps of (a) class I (2.42 Å), (b) class II (2.54 Å) and (c) class III (2.65 Å). Dashed lines are the migration barriers in pure alumina for the respective class of jumps.	90
Figure 5.8. Migration barriers of class III diffusive jumps as a function of the difference in the initial and final distance of the V_O from Mg_{Al} . Negative values on the x-axis represent jumps where V_O approaches Mg_{Al} . The dashed line is the migration barrier in pure alumina.	91
Figure 5.9. Migration barriers of three classes of jumps computed at two different c-axis lengths, keeping the potential parameters constant.	93
Figure 5.10. Migration barriers computed using the Lewis setup, compared to results obtained with the Binks potential and DFT calculations.	93
Figure 5.11. Change in migration barrier induced by the presence of Mg close to an oxygen vacancy. Results shown are for a small set of test cases.	94
Figure 5.12. Minimum energy pathways for jumps starting from vacancy positions, which became unstable due to the presence of Mg_{Al} . The inset shows a schematic view of the relaxation process leading from the metastable (m) position to the new initial (i) position. Going from the new initial (i) position to the final (f) position now requires two diffusive jumps going via the intermediate metastable (m) state. This two-step nature is reflected by the two barriers observed in the minimum energy pathways (MEPs). The lines are cubic splines interpolated between NEB images. Red and blue solid curves are the MEPs of the highest barrier class II and class III jumps, respectively from this initial position.	95
Figure 5.13. Minimum energy pathways showing the effect of V_O - V_O interaction by addition of a second V_O at different nearest neighbor sites. The dashed horizontal line is the migration barrier of the jump without a second V_O . Pathways with a destabilized initial position are shown in black, those with an increase in barrier in red, the one with an unaffected barrier in grey and the one with a lower barrier in blue. The lines are cubic splines interpolated between NEB images.	96
Figure 5.14. a) Mean square displacement versus time plots for oxygen atomic migration at different temperatures calculated using kinetic Monte Carlo simulations, b) Diffusion coefficients plots versus inverse of temperature to calculate macroscopic atomic diffusion law.	98
Figure 6.1. STEM-EDX spectroscopy results showing the presence of dopants and impurities at a grain boundary, (a) Aluminum, (b) Chlorine, (c) Lanthanum, and (d) Yttrium.	104

Figure 6.2. Line scan quantitative EDX analysis of a GB showing the presence of La and Y in the narrow region of the GB.	105
Figure 6.3. Segregation energy for single yttrium dopant sites situated at different depths from the near coincidence GB with (00.1) and (01.3) as GB parallel planes.	106
Figure 6.4. Segregation energy versus dopant concentration plot for the near coincidence GB with (00.1) and (01.3) as GB parallel planes.	106
Figure 6.5. Atomistic structures of a Y segregated near coincidence GB at different Y-dopant concentrations, (a) 0.60 at./nm ² , (b) 1.60 at./nm ² , (c) 2.59 at./nm ² , and (d) 3.59 at./nm ² . All the atomistic structures are seen parallel to the GB plane. Yttrium atoms are in blue, oxygen red and aluminum atoms are in pink.	108
Figure 7.1. Conformations of the PAA molecule on hydroxylated alumina surface in vacuum at (a) t=0, (b) t=0.017 ns (tail configurations), (c) t=0.059 ns (loop configurations), and (d) t=0.069 ns (train configuration). Green atoms in the polymer molecule are hydroxyl O, pink are the backbone carbon atoms, blue are Na counter ions.	112
Figure 7.2. Unstable hydroxylated alumina surface in water, (a) hydroxyl atoms detach from the surface in MD simulations with De Leeuw water, while (b) Al atoms detach with TIP3P water. Al is green, H white and O atoms are in red.	113

List of Tables

Table 3.1. Sigma values of the twin grain boundaries, surface area (A) of the cells used for the calculations and interfacial energies of grain boundaries (γ_{GB}) and surfaces (γ_{surf}) calculated in the present work. Sigma values is the ratio of the lattice points in the unit cell of coincident site lattice and the original lattice.	41
Table 3.2. Asymptotic/local minimum Segregation energy values (ΔH_{seg}) and corresponding concentration (C) for La-Y Codoped surfaces and grain boundaries. [§] Asymptotic ΔH_{seg} and C, *Value of ΔH_{seg} and C at a local minima; [#] neither asymptotic value nor minima is observed; [¥] change in the slope of the energy curve	48
Table 3.3. Segregation energy values (ΔH_{seg}) and corresponding concentration (C_1 and C_2) for Mg-La Codoped surfaces and grain boundaries. C_1 and C_2 are the interface dopant concentrations when 4 and 8 dopant atoms are put on the interface respectively.	49
Table 3.4. Segregation energy values (ΔH_{seg}) and corresponding concentration (C_1 and C_2) for Mg-Y Codoped surfaces and grain boundaries. C_1 and C_2 are the interface dopant concentrations when 4 and 8 dopant atoms are put on the interface respectively	51
Table 3.5. Packing fractions of the single and codoped grain boundaries (Grain boundary width for packing fraction calculation was taken 10 \AA^0 for La-Y, La and Y doping, while 6 \AA^0 for Mg-Y, Mg-La and Mg doped grain boundaries).	56
Table 3.6. Dopant-Oxygen coordination number (CN) and nearest neighbor (NN) distance for different codoping combinations	63
Table 4.1. Results of the Al-Cl Buckingham potential parameter optimization. The experimental and the fitted lattice parameter along with the error are listed in the table.	69
Table 4.2. Chlorine segregation energies are listed for alumina surfaces and grain boundaries at the concentration where the slope changes in the segregation energy plot. Corresponding characteristic concentrations are also given for each interface.	72
Table 4.3. Cl-Al coordination numbers of different interfaces are given with corresponding nearest neighbor distances.	76
Table 5.1. Details of the three primary classes of diffusive jumps of oxygen in alumina	87
Table 6.1. Concentrations of the Y and La dopants at three grain boundaries determined using EDX line scan analysis. It also gives the parallel planes of the adjacent grains and the misorientation angle of the GBs.	104

Table 6.2. Summary of the ΔH_{seg} at experimentally observed concentration and coordination number (CN) and near neighbor distance (NN).	108
---	-----

1. Introduction

This chapter sets the background for the present thesis. In this chapter we first discuss the theory of light transmission in polycrystalline alumina and then outline the key microstructural requirements to manufacture highly transparent polycrystalline alumina. The developments in the processing of transparent alumina in the last few decades are detailed out next. We identify the key processing issues, better fundamental understanding of which will help bridge the gap between knowledge and practice of processing of transparent alumina and lead to a knowledge based development of transparent alumina ceramics. At last, we state the goals and objectives of the present thesis.

1.1. Transparent Polycrystalline Alumina

Sapphire has excellent physical properties such as high strength, high temperature chemical inertness, and high degree of transparency. But high production costs and limitations in shapes and sizes prevent its use for wider potential applications such as wave guides, armor windows, high temperature refractory windows, watches, jewelry etc. On the other hand, polycrystalline alumina (PCA) has excellent mechanical properties and flexibility in shapes and sizes, but can't be used for transparent applications due to its inferior radiant energy transmission. The quest for combining the properties of both, led Coble to discover translucent alumina in 1962 using the hot isostatic pressing (HIP) technique [1]. Since then several attempts have been made in this direction. A breakthrough was claimed when Krell et al. [2] and Apetz and Bruggen [3] reported real inline transmittance (RIT) values as high as 70% in isolated attempts using slip casting and HIP. But no follow up commercial development on these promising results leads to the suspicion that either the processing method is not robust enough or it is too expensive. In the last decade, the spark plasma sintering (SPS) technique has been investigated in order to make the processing of alumina simpler and reproducible [4,5,6,7]. Roussel et al. [4] and Stuer

et al. [5] achieved 70% and 55% RIT values respectively, using standard SPS and transient element doping. But the dream of commercial scale application of transparent polycrystalline alumina still waits to see the light of day.

1.2. Light Transmission in Polycrystalline Alumina

First, we need to understand the light transmission mechanism in a polycrystalline material in order to identify the structural requirements to achieve high RIT values in a material. The three main sources of light scattering in a polycrystalline material are surfaces, grain boundaries and pores (Figure 1.1).

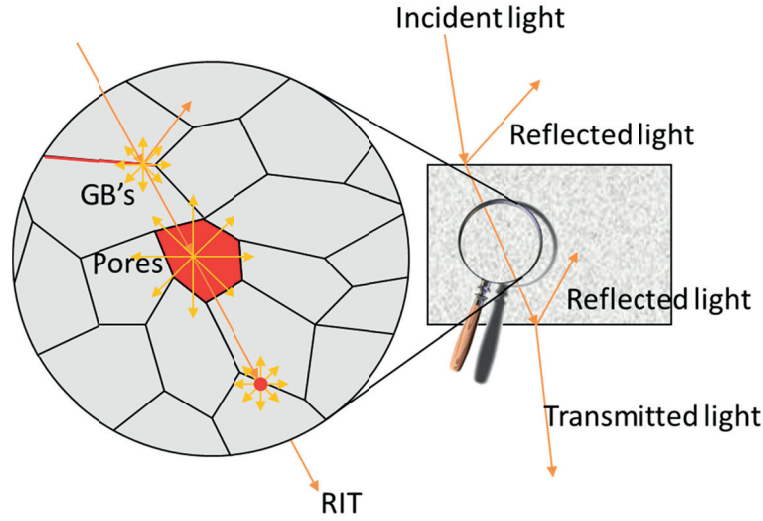


Figure 1.1. Surfaces, grain boundaries and pores are the sources of light scattering a polycrystalline material.

The RIT, i.e. the fraction of light which passes the material without adsorption or scattering, is described by the Lambert Beer Law:

$$RIT = (1 - R_s) \exp(-\gamma_{tot} d) \quad \text{Eq.1.1}$$

$$R_s = \frac{2R'}{1 + R'} \quad \text{Eq.1.2}$$

$$R' = \left(\frac{n-1}{n+1} \right)^2 \quad \text{Eq.1.3}$$

Where R_s is the loss due to the reflection (14% for alumina), n is the refractive index of the sample, d is the thickness of the sample, and γ_{tot} is the total scattering coefficient. γ_{tot} can be defined as the sum of the grain boundary and pore scattering contributions:

$$\gamma_{tot} = \gamma_{pore} + \gamma_{gb} \quad \text{Eq.1.4}$$

The scattering contribution by pores was described by Peelen & Matselaar [8] as:

$$\gamma_{pore,Peelen} = \frac{3V_p Q_{eff}}{4r_m \exp(3.5\sigma^2)} \quad \text{Eq.1.5}$$

Where V_p is the specific pore volume, r_m is the radius of the mode of the volume pore size distribution, σ is the standard deviation factor for a lognormal distribution of pores, and Q_{eff} is the effective dimensionless scattering efficiency of the pores defined as:

$$Q_{eff} = \left(\int_0^{\infty} Q_{sca}(r) f(r) r^2 dr \right) \left(\int_0^{\infty} f(r) r^2 dr \right)^{-1} \quad \text{Eq.1.6}$$

Where Q_{sca} is the scattering efficiency factor given by Mie theory and $f(r)$ is the log normal pore size distribution.

Apetz and Bruggen [3] derived a numerical expression for the grain boundary scattering coefficient approximating polycrystalline alumina with randomly distributed mono-dispersed spherical grains in a homogeneous matrix, which is given as:

$$\gamma_{gb,Apetz} = 3 \frac{\pi^2 r}{\lambda_0^2} \Delta n^2 \quad \text{Eq.1.7}$$

Where $2r$ is the grain size, λ_0 is the wavelength of the incident light, and Δn is the mean absolute difference in the refractive index of the sample.

As can be seen from Eq.1.5 and Eq.1.7, ***the microstructural requirements for higher RIT are: ultrahigh density, small grain sizes, grain alignment, and minimum pore volume.***

Above mentioned models have been used to numerically predict the RIT values of the transparent ceramics for several years. However, Stuer et al. [9] did an extensive experimental study of transparent alumina to link the observed transparency with measured porosity and defect size. They found that the previously developed models [3,8] overestimate the pore scattering. They used their experimental data to show that a more recent model developed by Pecharrroman et al. [10] explained the experimental data better than the previously developed models. The Pecharrroman scattering coefficients are given as follows,

$$\gamma_{gb,Pechorroman} = \frac{6\Pi^2 \alpha(\xi) \langle \alpha_g \rangle}{\lambda_0^2} \Delta n^2 \quad \text{Eq.1.8}$$

$$\gamma_{pore, Pechorroman} = \frac{32f\Pi^4 \langle \alpha_p^3 \rangle}{\lambda_0^4} \left(\frac{n^2 - 1}{n^2 + 2} \right)^2 \quad \text{Eq.1.9}$$

Where, $\alpha(\xi)$ being a texture function depending on the preferential texture direction of the sample, f being the pore volume fraction and n the average refractive index of the sample. $\langle \alpha_g \rangle$ and $\langle \alpha_p \rangle$ are the characteristic pore and grain radii, respectively, given as,

$$\langle \alpha_g \rangle = \sum_i \alpha_{g,i} f_i = \frac{\sum_i \alpha_{g,i}^4}{\sum_i \alpha_{g,i}^3} \quad \text{Eq.1.10}$$

$$\langle \alpha_p^3 \rangle = \frac{\sum_i \alpha_{p,i}^6}{\sum_i \alpha_{p,i}^3} \quad \text{Eq.1.11}$$

Where, $\alpha_{g,i}$ and $\alpha_{p,i}$ are the grain and pore radius, respectively, of the i^{th} class of the size distribution, f_i is the fraction of the grain with radius $\alpha_{g,i}$. In the Pechorroman model, the expression for grain boundary scattering coefficient is very similar to earlier proposed by Apetz as mentioned in Eq.1.7 except the separation of texturing function from Δn . However, the pore scattering coefficient is significantly different from the one proposed by Peelen as mentioned in Eq.1.5. Stuer et al. [9] showed that with the new definition of characteristic pore size, the pores smaller than certain pore size do not contribute significantly to the pore scattering coefficient. It is rather only the bigger size pores which contribute to the pore scattering. Therefore, it can be implied that smaller size pores do not hurt the transparency of the ceramic, and hence the requirement of ultrahigh density could be more flexible.

1.3. Key Processing Developments

Having identified the high density and submicron size and/or oriented grains as the requirements for the transparent alumina, we give an overview of the developments in the processing of transparent alumina over the last few decades to progress in this direction in the following section. Majority of the work has been focused on two important aspects of the processing: developing the methods for defect free green body processing and efficient sintering methods to limit the grain growth in the final stages of sintering while maintaining the high density.

1.3.1. Defect free green body processing

Uniaxial and isostatic pressing techniques were used in the initial investigations on the synthesis of transparent/translucent alumina [1]. These techniques continue to be used by some researchers even in some recent works [7,11,12]. However, Schmidt et al. [13] emphasized on the need for the processing techniques which can

produce defect-free green bodies and can build defect healing mechanism during sintering for the synthesis and processing of nanoscaled ceramics. The study concluded that nanoscaled ceramic powders can be effective in separating the densification from the grain growth provided the surface interaction of the small particles can be controlled during colloidal processing. In a series of papers by Krell et al. [2,14,15], it was pointed out that defect free green bodies with homogeneous particle coordination are essential to achieve the highest density at low temperatures and thereby limit grain growth. Wet processing routes (slip/gel casting) with high solid content but low viscosity have been found to be the most effective green body processing methods to obtain homogeneous and highly dense green bodies [3,4,5,15,16]. The difficulty of controlling interactions increases as the particle sizes become smaller. Preparing a uniform stable suspension of ultrafine ceramic powders is very difficult due to the tendency of agglomeration of high specific surface area fine ceramic powders. Organic polymer molecules are often used in the wet processing techniques in order to control the stability of the colloidal suspension of alumina nano particles [17]. Short chain polymer molecules containing easily dissociable functional groups mostly provide electrostatic stabilization, while medium molecular weight polymer molecules ($10000 < MW < 25,000$) can provide steric as well as electrosteric stabilization based on solution condition and conformation of the polymer molecule [18]. Dolapix [15], ammonium polymethacrylate [2], Carboxylic acids [13] have been used in the literature to stabilize the alumina nano particle suspensions.

1.3.2. Use of modern sintering methods and sintering aids

Until the last decade, researchers have focused on conventional sintering methods and hot isostatic pressing (HIP) to obtain fully dense transparent alumina [1,19]. Krell et al. [14,20] and Apetz and Bruggen [3] employed a pressureless pre sintering followed by HIP to obtain fully dense alumina with a grain size in the submicron range. In the recent times microwave sintering [12] as well as spark plasma sintering [4,5,6] have been successfully used to obtain fully dense transparent alumina with RIT values up to 70%. In addition to defect free green body processing and new sintering techniques, sintering additives such as, Y, La, and Mg, have also been used to control the grain growth during the final stages of sintering [4,5,21]. It has been shown in the studies focusing on creep enhancement as well as transparent ceramics that the addition of dopants results into smaller grain size. In addition, it has been observed that codoping, i.e. combination of dopants, results in smaller grains, higher RIT's and higher creep resistance in comparison to singly doped alumina [5,22,23,24,25]. In 2003 two separate groups reported an RIT value of about 70% without using any dopants [2,3]. However, there has not been any follow up work on that so far. Since then there have been several studies on the effect of dopants on the RIT enhancement in alumina [4,5,11,19]. The best results in RIT enhancement of

transparent alumina with sintering agents were reported very recently by Roussel et al. [4], who achieved an RIT value of 71% with La doping and spark plasma sintering method. Stuer et al. [5] studied the effect of single doping as well as codoping on the transparency of alumina. They reported the best RIT values with La and Y codoped alumina in comparison to singly doped Y, La or Mg.

1.4. Need and Scope of the Present Thesis

In the following section we discuss the existing gaps between knowledge and practice of the transparent alumina processing, which are essentially the topics of investigation of the present thesis. As mentioned in the previous section, the two major advancements in the processing of transparent alumina have been colloidal processing of alumina nano particles to form the green bodies and use of sintering additives to limit the grain growth during sintering. Adsorption mechanism of the dispersants which are used in the colloidal processing of alumina is not very well understood at the atomic scale. On the sintering side, better understanding of the effects of dopants segregation on the grain boundary structure and solid state oxygen diffusion mechanism in alumina could help in achieving the microstructural requirements for transparent alumina.

1.4.1. Adsorption of dispersants on Alumina Surface

Controlling the agglomeration of ultrafine powders in a colloidal suspension is a challenge in the wet processing of nano scaled ceramic powders. Carboxylic acids/polymers, e.g. acetic acid, citric acid, polyacrylic acid (PAA), have been used as the dispersants for achieving the well dispersed suspensions of ultrafine alumina powders [2,13]. Recently carboxylic dispersants have also been tested to induce the particle surface orientation and hence grain alignment in the sintered alumina under the influence of magnetic field [26]. It is known that the charged dispersants are chemisorbed on the alumina surface and thereby stabilize the suspension due to double layer interaction as well as steric hindrance between the particles [27,28]. However, adsorption of a polyelectrolyte on the powder surface is a complex process to understand experimentally due to the very small thickness of the adsorbed layer, in the range of few nanometers, and the difficulty of characterization methods for wet samples. The rheology of the suspension becomes further complex when using ultrafine powders in solutions of high ionic strength, which is a consequence of dopant addition during the colloidal processing of alumina. Adsorption behavior of dispersants on alumina surface is the deciding factor for its effectiveness, which depends on solvent conditions [29], powder surface characteristics [30], as well as conformational entropy of the polymer [31]. Experimental studies have helped to understand the overall effect of dispersants on the colloidal stability of alumina and have proposed possible hypothesis for polymer adsorption. However, due to the lack of the definitive fundamental understanding of

adsorption mechanisms of polymer molecules on alumina surfaces the control on colloidal processing and its parameters is still very limited. Atomistic simulation is a promising approach to extend the understanding of the basic issues due to its approachable length scales, time efficiency and ease to control different parameters individually. The goal of this part of the work was to understand the adsorption mechanism of polymer dispersant, poly-acrylic acid, at the atomic level. Preliminary work was done on the effect of the substrate surface on the adsorption mechanism of organic molecules, dependence of the conformational arrangement of dispersants on the alumina surface characteristics. Adsorption of PAA was simulated on the characteristic, morphology dominating alumina surfaces using the molecular dynamics approach based on empirical force fields.

1.4.2. Grain Boundary Segregation of Dopants

In addition to the defect free green body processing, limiting the grain growth in the final stages of sintering is another big challenge to achieve fully dense transparent alumina with minimal grain coarsening. Various rare earth elements (La, Mg, and Y) have been employed in the past as sintering aids/dopants for the sintering of transparent alumina [4,5,11,21]. The larger dopants have very low solubility in the bulk alumina and segregate to the grain boundaries, thereby reducing the rate of densification and grain size/sintered density ratio [32,33]. Recently, codoping of alumina with rare earth elements (e.g. La-Y, Y-Mg, Mg-La) has been reported to further reduce the creep rates of alumina [24,34], as well as to increase the RIT in alumina [5]. Several propositions have been made to explain the additive effect of codoping over single doping [21,32,35]. But, the basic mechanism behind the additive effect of codoping over single doping is far from well understood and conclusive. Therefore, the second objective of the current thesis was to improve the understanding of the atomistic mechanisms behind doping and codoping using classical atomistic modeling methods. Energy minimization method based on empirical potentials was used to calculate the relaxed surfaces and grain boundaries. The effect of doping and codoping was studied on 9 surfaces and 8 grain boundaries for three codoping combinations: La-Y, La-Mg and Mg-Y. These results will give interesting insights into interfacial energies and consequent grain growth for better control of microstructures toward transparent ceramics.

1.4.3. Solid State Diffusion of Oxygen in Alumina

Knowledge of diffusion in alumina is crucial for understanding high temperature processes such as, diffusional creep, sintering of polycrystals, plastic deformation of single crystals, and alumina scale formation in Al containing alloys. Tracer diffusion experiments are conducted with O^{18} to determine the oxygen diffusion coefficient of alumina at different temperatures. The activation energy and pre-exponential constant are calculated using the Arrhenius equation $D = D_0 \exp(-E_a / RT)$. The

activation energy of oxygen diffusion in alumina via vacancy mechanism has been reported to be 5-6 eV in several experimental studies [36]. On the other hand, several computational methods have been used to simulate the solid state oxygen diffusion in alumina using force field as well as ab-initio methods. However, the atomistic simulation studies report the activation energy of oxygen vacancy diffusion in pure alumina to be 1-2.5 eV, not being able to capture the experimental values [37,38]. This is also popularly known as the conundrum of oxygen diffusion in alumina, a phrase coined in ref [39]. Diffusion process in undoped alumina is controlled by oxygen vacancy diffusion since the rate of diffusion of Al^{3+} is much faster than O^{2-} [38,39]. As mentioned earlier, alumina is often doped with transition elements (e.g. La, Y, Mg) to enhance its mechanical and optical properties, which also affects the diffusion process. In addition to the difficulty in simulating oxygen diffusion in bulk alumina due to its multiscale nature, the presence of impurity/dopants makes it an even more complex problem to handle in atomistic simulation. The objective of this part of the work was to devise a methodology to simulate accurately and efficiently multiscale problem of oxygen diffusion in bulk alumina. In the present work, nudged elastic band method [40] based on empirical force field was used to study the effect of Mg on the oxygen diffusion in alumina. Binding energies and migration barriers of diffusive jumps in the neighborhood of Mg were calculated to gain an insight into the defect cluster formation, migration pathways, and defect destabilization. Understanding of diffusion mechanism and effect of Mg on diffusion in alumina will be very useful to understand the mass transport and grain growth process during the sintering of transparent alumina and in turn provide a better control over the doping process of alumina.

1.5. Objectives

To summarize what has been discussed so far, polycrystalline alumina with submicron size grains, high density and oriented grains needs to be synthesized. Polymer dispersants are used to form stable colloidal suspension of alumina nano powders. But their efficiency and utility can be enhanced with the better understanding of their adsorption mechanism on particle surfaces. Further insights into the surface specific adsorption behavior of polymer additives at the atomic level needs to be gained using the atomistic simulation methods, which could help forming green bodies with controlled particle orientation, and sintered piece with desired grain orientation thereafter. On the sintering aspect, the grain growth should be minimized in the final stages of sintering while ensuring the high density of alumina. The doping of alumina has been shown to be effective in limiting the grain growth. However, it seems to have reached a stagnation phase, where no more tangible benefits are possible with the same doping methods. Better fundamental atomic level understanding of the effects of dopants type, concentration and doping

strategy (single/co/multiple doping) on the grain boundary structure is required to devise new doping methods to increase the efficiency of doping in limiting the grain growth and controlling the microstructure. Finally, the discrepancy in the activation energy of the solid state oxygen diffusion between simulation and experiments calls for taking into account the real system phenomena e.g. effects of dopants/impurities on the oxygen diffusion in alumina. Resolution of this issue will not only enhance our understanding of high temperature sintering of alumina ceramics but many high temperature processes, e.g. diffusional creep, sintering of ceramics, plastic deformation of single crystals and alumina scale formation in Al containing alloys.

2. Computational Methods

This chapter gives the brief description of the computational methods used in the current work. Full details of these methods are out of the scope of the present work, but the following chapter should serve well as an introduction to the most commonly used atomistic simulation methods and the references provided can be followed for a deeper understanding. All the methods used in the present work are based on the classical description of energy via empirically derived analytical functions and fitting parameters. The chapter also gives the details of the construction of the different types of simulation cells, boundary conditions, and the limitations of the methods used in the present work.

2.1. Force Field Description

To start with the atomistic simulations, the first basic requirement is to have an accurate force field. The accuracy of any force field based simulation depends heavily on the accuracy of the force field. A force field is essentially a mathematical function used to describe the potential energy of the system in combination with the parameters to fit the mathematical form for various atom types present in the system. The entire force field approach is based on the Born-Oppenheimer approximation that the effect of electrons can be embodied into a single potential energy function which depends only on the nuclear positions. The potential energy of a system can be described as a combination of the bonded and non-bonded interactions (Eq.2.1). Bonded interaction depends on angles and torsion as well as the chemical bond (Eq.2.2). Non-bonded interaction consists of long range electrostatic interaction and short range van der Waals interactions (Eq.2.3).

$$E_{total} = E_{bonded} + E_{non-bonded} \quad \text{Eq.2.1}$$

$$E_{bonded} = E_{bond} + E_{angle} + E_{dihedral} \quad \text{Eq.2.2}$$

$$E_{non-bonded} = E_{electrostatic} + E_{vanderWalls} \quad \text{Eq.2.3}$$

2.1.2. Bonded interaction

The force between the atoms which are connected by covalent bonds is represented by bonded potentials. Bonded potential consists of mainly three components: Bond energy, bond angle energy, and bond torsion energy.

Bond potential is the energy associated with the stretching of the bonds. It is represented in the form of a spring potential. The energy of the bond is,

$$E_{bond}^{harmonic} = k_l (r - r_0)^2 \quad \text{Eq.2.4}$$

k_l is the spring constant for the bond potential and r_0 is the equilibrium bond distances. This means that the bond energy increase if the bond stretched or compressed, and keeps on increasing as the bond is stretched further as shown in the Figure 2.1. However, in the real molecules, the bond will break if the bond is stretched sufficiently, which is not predicted in this approach. However this model fits well around the equilibrium bond length. Therefore, other mathematical forms have been developed to fit better to the real molecular bonds. The Morse potential is one of the very commonly used amongst them. It is given as,

$$E_{bond}^{morse} = D \left[\left(1 - e^{-\alpha(r-r_0)} \right)^2 - 1 \right] \quad \text{Eq.2.5}$$

Where, D is the dissociation energy of the bond and α is a parameter to describe the anharmonicity of the bond. Figure 2.1 shows that the Morse potential captures the anharmonicity of the bond well and hence can be applied in wider situations than the simple harmonic potential.

Energy associated with the bending of the bond angles from their equilibrium position is again modeled using the harmonic approximation,

$$E_{angle} = k_\theta (\theta - \theta_0)^2 \quad \text{Eq.2.6}$$

k_θ is the spring constant for the bond angle potential, θ and θ_0 are the bond angle and equilibrium bond angles, respectively. Once again, the harmonic approximation for the bond angle potential fits best close to the equilibrium bond angle. But, it is more adequate to use in this case since the bond angles do not change much.

Energy associated with the torsion (rotation around the bond axis) of the bond is represented by a periodic cosine function for the torsion potentials,

$$E_{\text{torsion}} = k_{\phi} (1 + \cos(n\phi - \phi_0))$$

Eq.2.7

k_{ϕ} is the force constant to twist bond around the bond axis, n is a scaling parameter to describe the number of oscillations within one complete revolution.

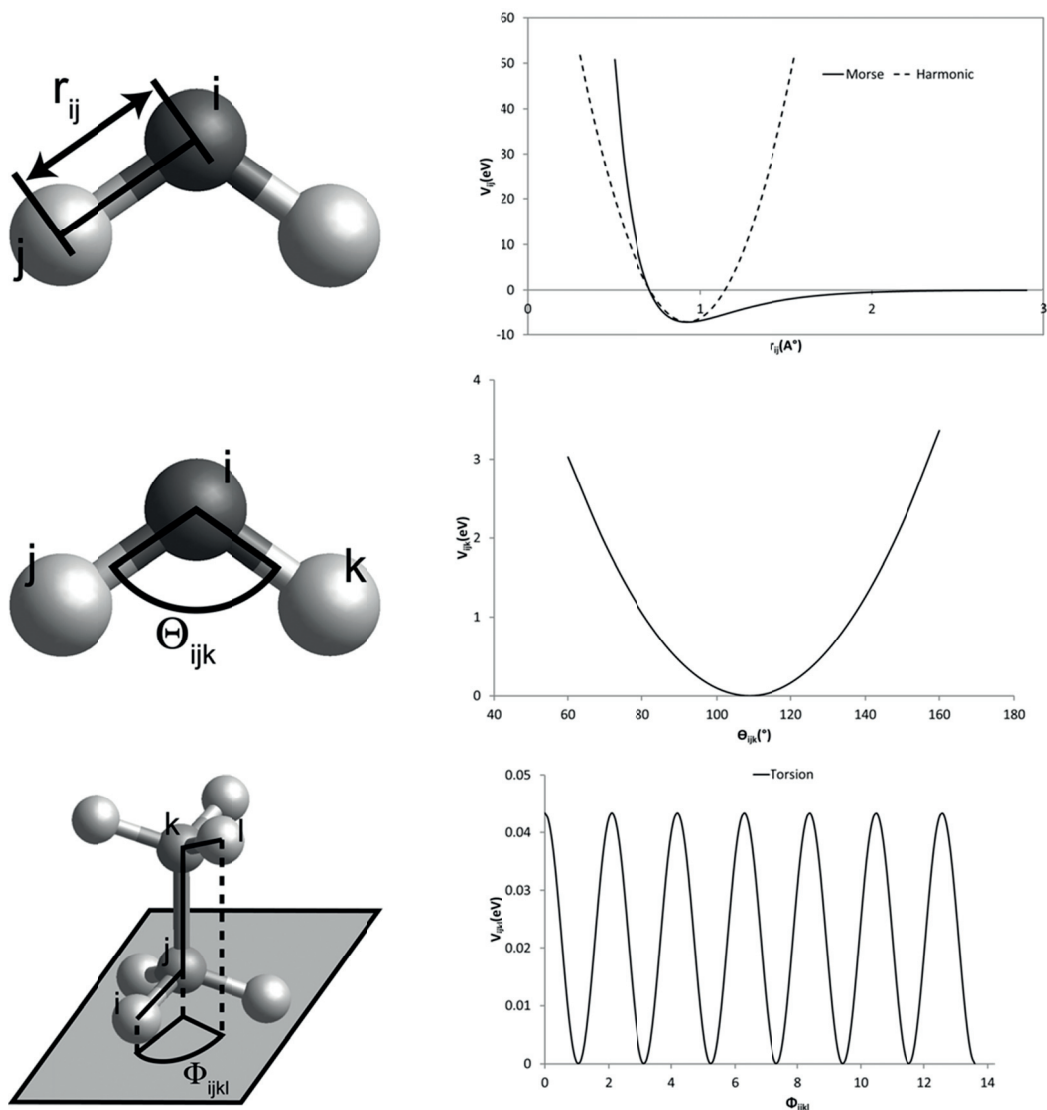


Figure 2.1. Schematic diagram of various types of bonded interaction potentials and their function form, (a) bonded potential, (b) angle potential, and (c) torsion potential

2.1.3. Non-bonded interactions

Non-bonded interactions are the sum of long range electrostatic energy and short range van der Waals interactions.

2.1.3.1. Electrostatic interaction

Electrostatic potential energy between two charged ions is given by,

$$E_{ij,electrostatic} = \frac{q_i q_j}{4\pi\epsilon_0 r_{ij}} \quad \text{Eq.2.8}$$

q_i and q_j are the charges on ions i and j respectively, and ϵ_0 is the permittivity of vacuum. The electrostatic potential energy decays as the inverse power of r , but the number of interacting ions increases as the power of r^2 . Hence, the energy density increases with the distance instead of decreasing, which makes it difficult to integrate the electrostatic interaction energy over all the pairs of ions using a standard integration mechanism.

The most commonly used method to address this problem is the Ewald summation method [41]. It first applies a Laplace transformation to the coulomb term to accelerate the evaluation and then is separated into two terms. One of these terms converges quickly in the real space and the second decays quickly in the reciprocal space. The self-energy term is subtracted in order to evaluate the interaction correctly.

$$E_{Coulomb} = E_{real} + E_{reciprocal} + E_{self} \quad \text{Eq.2.9}$$

$$E_{real} = \frac{1}{2} \sum_{i=1}^N \sum_{j=1}^N \frac{q_i q_j}{r_{ij}} \text{erfc} \left(\eta^{\frac{1}{2}} r_{ij} \right) \quad \text{Eq.2.10}$$

$$E_{reciprocal} = \frac{1}{2} \sum_{i=1}^N \sum_{j=1}^N \sum_G \frac{4\pi}{V} q_i q_j \exp(iG \cdot r_{ij}) \frac{\exp \left(-\frac{G^2}{4\eta} \right)}{G^2} \quad \text{Eq.2.11}$$

$$E_{self} = - \sum_{i=1}^N q_i^2 \left(\frac{\eta}{\pi} \right)^{\frac{1}{2}} \quad \text{Eq.2.12}$$

Here q is the charge on an ion, G is the reciprocal lattice vector, V is the volume of the unit cell, and η is the parameter which divides the work between real and reciprocal space. The cut off distance (R_{max} and G_{max}) is applied in calculating both real as well reciprocal terms. One of the criteria to optimize the values of R_{max} , η and G_{max} is to minimize the number of terms in both summations. For a given accuracy A , R_{max} , η and G_{max} are given as,

$$\eta_{opt} = \left(\frac{Nw\pi^3}{V} \right)^{\frac{1}{3}} \quad \text{Eq.2.13}$$

$$r_{\max} = \left(\frac{-\ln A}{\eta} \right)^{\frac{1}{2}} \quad \text{Eq.2.14}$$

$$G_{\max} = 2\eta^{\frac{1}{2}} (-\ln A)^{\frac{1}{2}} \quad \text{Eq.2.15}$$

w is the parameter which defines the relative computational cost of real and reciprocal term calculation.

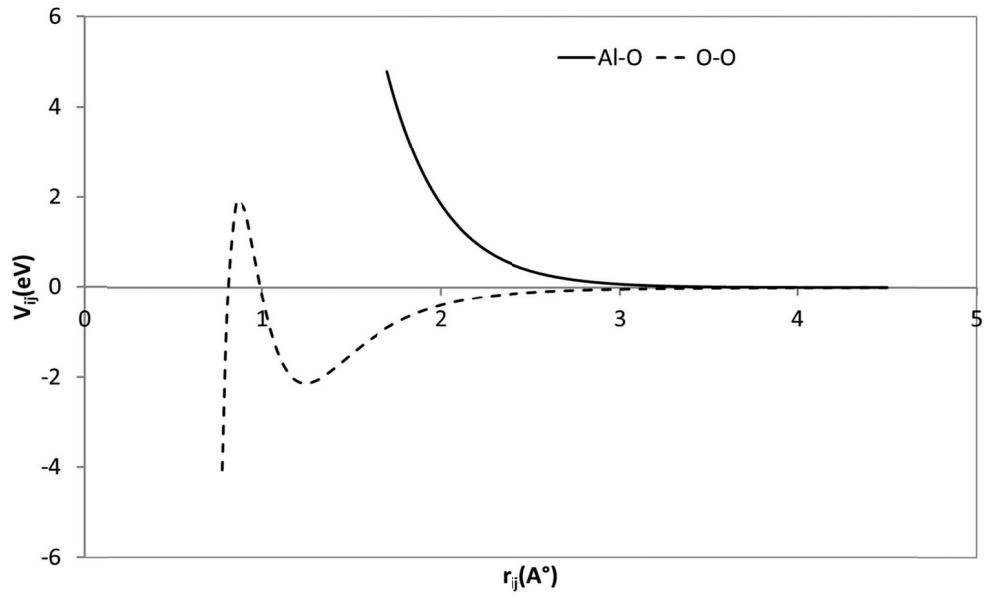
2.1.3.2. Short Range Interactions

Short range interaction becomes important when the atoms are in the immediate coordination shells. Short range attractive term is an interaction due to the instantaneous dipole- instantaneous dipole interaction energy which comes from quantum mechanics and is represented by the r^6 inverse term. The repulsive term is introduced in order to avoid the electron cloud overlapping. For the ionic cases, it is either represented by a positive term which varies inversely with distance, or an exponential form. The first one is called the Lenard-Jones potential (Figure 2.2b) and the second one is called the Buckingham potential (Figure 2.2a),

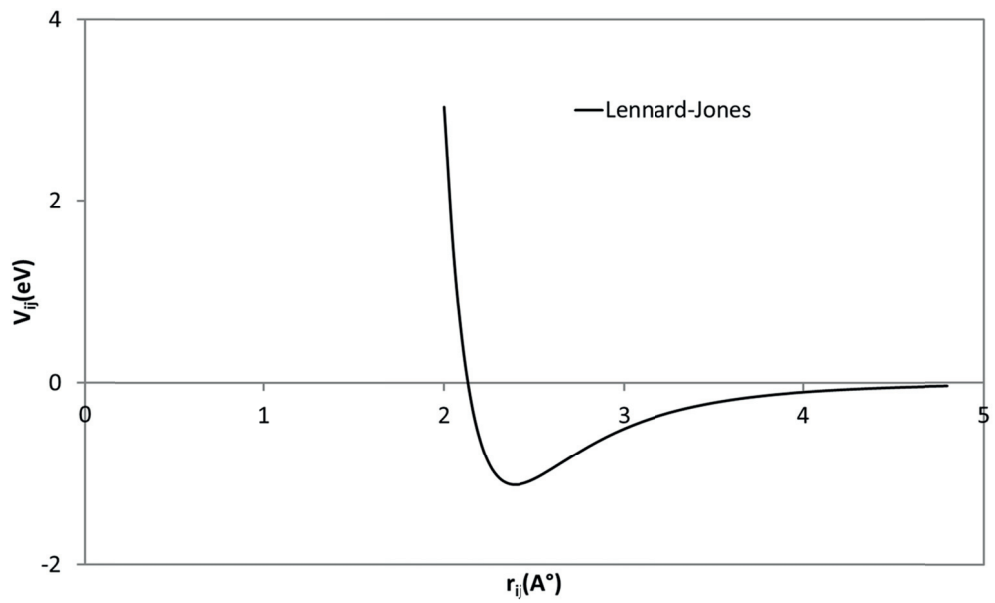
$$E_{\text{buckingham}} = A \exp\left(-\frac{r_{ij}}{\rho}\right) - \frac{C_6}{r_{ij}^6} \quad \text{Eq.2.16}$$

$$E_{\text{Lenard-Jones}} = \frac{C_m}{r_{ij}^m} - \frac{C_6}{r_{ij}^6} \quad \text{Eq.2.17}$$

A , ρ , C_6 and C_m are the parameters which are fitted with experimental and/or quantum mechanical data of properties.



(a)



(b)

Figure 2.2. Functional form of two main types of non-bonded dispersion interactions, (a) Buckingham potential for Al-O and O-O pairs, and (b) typical shape of a Lennard-Jones potential

2.1.3.3. Polarisability

Polarisability of atoms can be taken into account by a core-shell model proposed by Dick and Overhauser [42]. In this model a massless shell is attached to the core of

the atom with a spring. The core consists of the nucleus and the inner shell of the electrons, while the shell consists of the valence electrons. The potential energy between the core and the shell is given by a harmonic spring potential,

$$E_{spring} = \frac{1}{2} k_{c-s} r_{c-s}^2 \quad \text{Eq.2.18}$$

k_{c-s} represents the rigidity of the atom and r_{c-s} is the distance between the core and the shell. Conventionally, short range forces act only on the core, while the electrostatic force acts on the core as well as the shell. Due to this discrepancy in the forces on the core and the shell, the environment also plays a role in the polarisability of the atoms. While performing molecular dynamics (section 2.4) with core-shell model, shells are needed to be given special treatment because the approach fails with the massless shells. The problem is addressed either by assigning a small mass to the shells allowing the shells to follow the normal Newton's laws of motion. Another approach is to treat shells adiabatically, where the shell positions are optimized after every time step. However, this model takes into account only the dipole-dipole interaction into account. There can be higher orders of ion distortions which can be important in certain cases, especially in high symmetry structures.

2.1.4. Force Filed Optimization

To develop the force field for a material or for a particular modeling problem, first task is to identify the right functional form to correctly represent the potential energy of the function, which depends mostly on the material characteristics. Once the functional form is chosen, the parameters of the functional form need to be optimized. The optimization procedure depends on the desired accuracy and goal of the modeling task. Direct transfer of the known parameters from one system to another similar system by analogy is the minimal form of optimization. It is fast and easy. E.g. If the force field for alumina is known and we want to simulate the grain boundary segregation of Cl, but we don't know the interaction potential parameters for Al-Cl. Keeping rest of the potential parameters constant, only the Al-Cl interaction parameters can be fitted to the lattice properties of AlCl_3 , a compound which has both Al and Cl and whose experimental properties or abinitio calculations are available in the literature. Properties to be fitted vary depending on the goal of the simulation task.

On the other hand, in a maximal approach the parameters of the force field are derived from the scratch. It is much more time consuming and requires appropriate target data to be fitted with, but it is more accurate and precise for the goal of the calculation. Not only the parameters of a functional form have to be optimized, but also the process of optimization starts with identifying the functional form itself.

Once the functional form is set the parameters are fitted with free energies, density, heat capacity, lattice parameters, heats of sublimation/vaporization etc.

2.2. Simulation Cell Constructions

Once the force field has been determined, the next requirement is to construct the simulation cell. Simulation cell is the set of the initial coordinates of the atoms to represent the system of interest. Size of the simulation cell for various simulations is important so as to avoid any finite cell size effects, but at the same time keep the requirements of computational power to the practical limits. There are three main types of simulation cells used in the current work: bulk, surfaces, and grain boundaries. The construction method for each of them will be explained below.

2.2.1. Bulk cell

Construction of the bulk cell requires crystallographic information of the material: unit cell parameters and the basis vectors for the atoms. These details are usually obtained by x-ray crystallography experiments. The bulk structure is minimized using the force field. The properties of the simulated bulk cell, e.g. lattice parameters, elastic constants, dielectric constants etc., are usually compared with the experimental values in order to validate the potential parameters. The three dimensional boundary conditions are applied in the simulation of the bulk cell. Usually, larger supercells are used instead of a single unit cell in order to avoid finite size effects.

2.2.2. Slab construction

To simulate surfaces and interfaces a slab of a material is constructed which has two surfaces and a sandwich of bulk like properties in the middle. The cell dimension in the direction perpendicular to the surface is chosen to be large enough so that the atoms in the center of the slab do not feel significant interaction from the surface atoms and hence have bulk like surroundings. The slab construction is often used in the molecular dynamic simulations of the surface adsorption, as well as for solid-solid interfaces e.g. the grain boundaries to be studied in this thesis

To create a slab, the bulk cell is rotated to get the right orientation for the slab surface. Then, several surface cuts are generated at different heights and the lowest possible energy cut is chosen for the further minimization of the simulation cell. As shown in the Figure 2.3, the atoms left out of the slab cell after the rotation and surface cut are periodically refilled in the slab cell of the same volume as the bulk cell. Two dimensional periodic boundary conditions are applied in the plane of the surface and the slab unit cell is repeated in the normal direction to the surface cell to get a large enough slab thickness (Figure 2.4). A large enough gap is created on top

of the surfaces to avoid the surface-surface interaction. This gap can be filled with liquid, gas or another solid to simulate the interfaces.

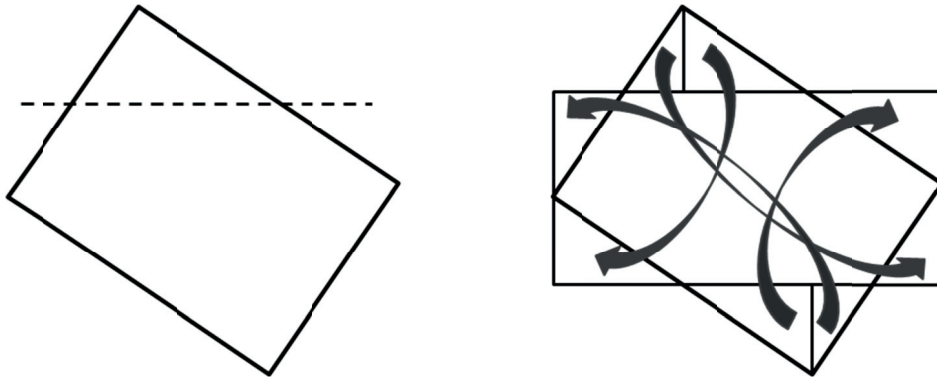


Figure 2.3. (a) Surface cut along the desired orientation of the slab surface, and (b) refilling of the left out atoms after the surface cut into the slab cell

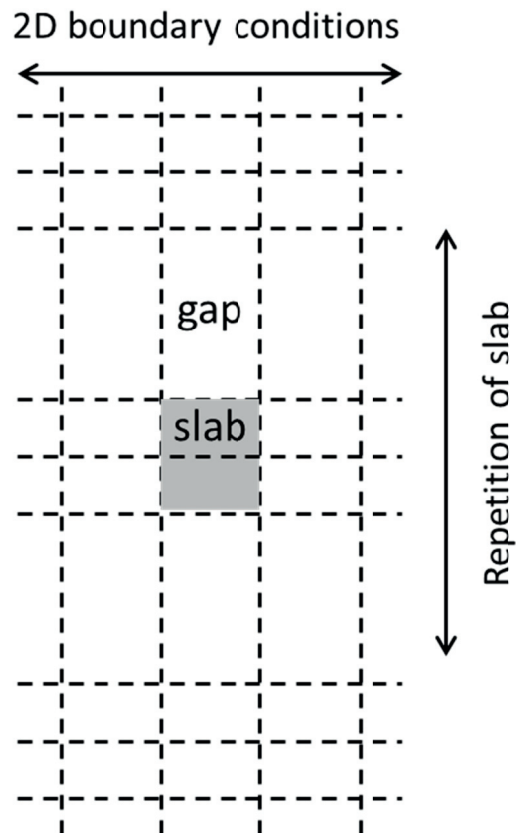


Figure 2.4. 2-D periodic boundary conditions are applied in the surface plane of the slab and the repetition of the slab unit cell is done along the direction normal to the surface to construct a slab cell.

2.2.3. Surface construction

A surface cell has only one surface in comparison to the two exposed surfaces in case of a slab. To generate a surface cell, first a single slab is created as described in the previous section. Two dimensional periodic conditions are applied in the plane of the surface. The single slab cell is repeated ($m+n$) times in the normal direction to the surface plane. The surface cell is divided into two regions consisting of m and n single slab cell widths perpendicular to the surface plane (Figure 2.5). The atoms in the region 1 close to the surface are allowed to relax during energy minimization, while atoms in the region 2 are kept fixed. The width of the region 1 (m) is chosen such that the atoms in the bottom most layer of the region 1 do not relax at all during the energy minimization of the surface. The width of the region 2 (n) is chosen such that the top most atoms of the region 2 feel negligible interaction from the bottom most atoms of the region 2.

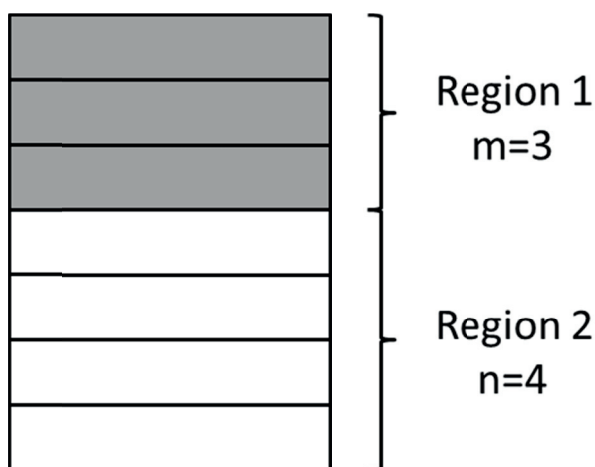


Figure 2.5. A surface cell consists of 2 regions. Atoms in the region 1 are allowed to relax, while the atoms in the region 2 are kept fixed during energy minimization.

2.2.4. Twin grain boundary construction

A tilt grain boundary is formed between two grains with the identical miller indices, which are rotated about an axis which is perpendicular to the grain boundary plane normal. Tilt grain boundary is essentially a configuration of edge dislocations between two grains. This is the simplest type of grain boundary to simulate in atomistic modeling. To create the simulation cell for a tilt grain boundary, two surfaces with the identical miller indices are put back to back (Figure 2.6). For each grain boundary under actually external conditions such as pressure, temperature, and chemical composition, there are a few relative rigid body translations parallel and perpendicular to the grain boundary plane, which correspond to the minimum energy interface structure. To explore these minimum energy positions, top surface scans in small steps over the lower surface can be made while keeping the lower one

fixed. The lowest energy translation is selected for the final grain boundary structure. The interface energy of such a grain boundary can be calculated using following equation,

$$\gamma = \frac{E_{region1} - E_{region1-region2} - mE_{bulk}}{A} \quad \text{Eq.2.19}$$

Where $E_{region1}$ is the energy of the region 1 of both the grains, $E_{region1-region2}$ is the energy of the region1-2 boundary, E_{bulk} is the energy of the bulk and A is the area of the interface.

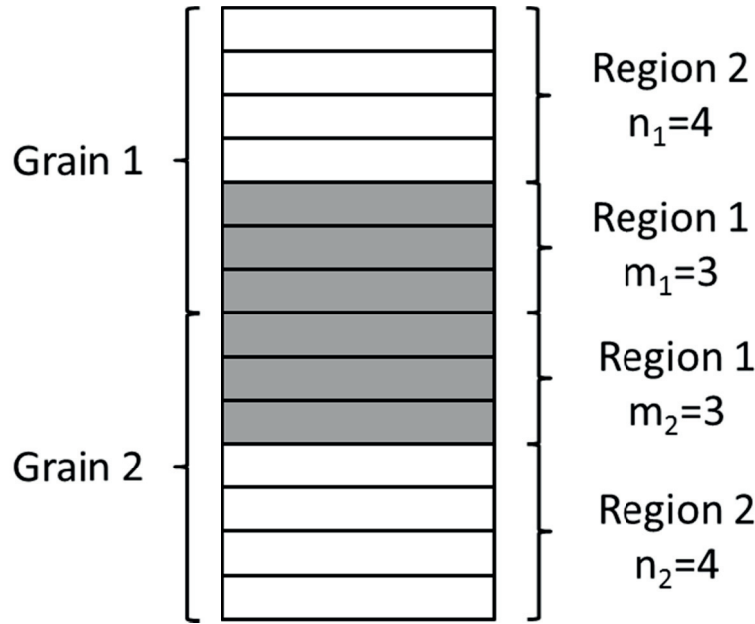


Figure 2.6. A mirror twin grain boundary consists of 2 surfaces with the same miller index back to back and region 1 and region 2 in each block are similar as in the case of the surface cell.

2.2.5. Near coincidence grain boundary construction

The interphase boundary (grain boundary) between two grains with different miller indices can be considered as two dimensional hexagonal lattices for hexagonal systems. A Two dimensional coincidence site lattice is produced by rotating one lattice with respect to the other lattice about an axis perpendicular to the grain boundary plane until three lattice sites of the two grains are in common (Figure 2.7). The condition for exact coincidence is,

$$\left(\frac{a_1}{a_2}\right)^2 = \left(\frac{m^2 + n^2 + mn}{k^2 + l^2 + kl}\right) \quad \text{Eq.2.20}$$

where, k , l , m and n are integers. The rotation angle required to bring the two grains into exact coincidence is given by,

$$\theta = \sin^{-1} \frac{(\sqrt{3}/2)k}{(k^2 + l^2 + kl)^{1/2}} \pm \sin^{-1} \frac{(\sqrt{3}/2)m}{(m^2 + n^2 + mn)^{1/2}} \quad \text{Eq.2.21}$$

The value of θ varies between 0° and 60° . However, exact coincidence occurs only when the lattice parameters of the planar lattice are same for both the grains, i.e. $a_1=a_2$ [43]. But for grains with different miller indices, and hence different planar lattice parameters, it can never be satisfied exactly. The misfit (F) due to the different planar lattice parameters of the two grains is given by,

$$F = 2 \frac{\left[a_1 \left(\sum P_1 \right)^{1/2} - a_2 \left(\sum P_2 \right)^{1/2} \right]}{a_1 \left(\sum P_1 \right)^{1/2} + a_2 \left(\sum P_2 \right)^{1/2}} \quad \text{Eq.2.22}$$

Where, the planar reciprocal coincidence densities at the interface $\sum P_1$ and $\sum P_2$ are given by,

$$\sum P_1 = m^2 + n^2 + mn \quad \text{Eq.2.23}$$

$$\sum P_2 = k^2 + l^2 + kl \quad \text{Eq.2.24}$$

As evident from Eq.2.22, the misfit can be minimized and the density of planar coincidence sites ($1/\sum P_1$ or $1/\sum P_2$) can be maximized by increasing the size of $\sum P_1$ and $\sum P_2$. However, it may result in increasing the size of the resulting primitive unit cell of the coincidence site lattice, which may be too expensive computationally. Therefore, a good compromise is needed between the misfit F and the size of the primitive unit cell.

In constructing the simulation cell for a near coincidence grain boundary, first task is to find the appropriate scaling vectors (m , n , k and l), which can minimize the misfit keeping the size of the primitive unit cell under manageable computational cost. Once the scaling vectors are determined, two surfaces are put back to back and

scanning is performed parallel and perpendicular to the plane of the grain boundary to get the minimum energy shift between the two surfaces. Similar to the twin grain boundary, near coincidence grain boundary cell consists of 2 blocks, each having a fixed and a flexible region for relaxation.

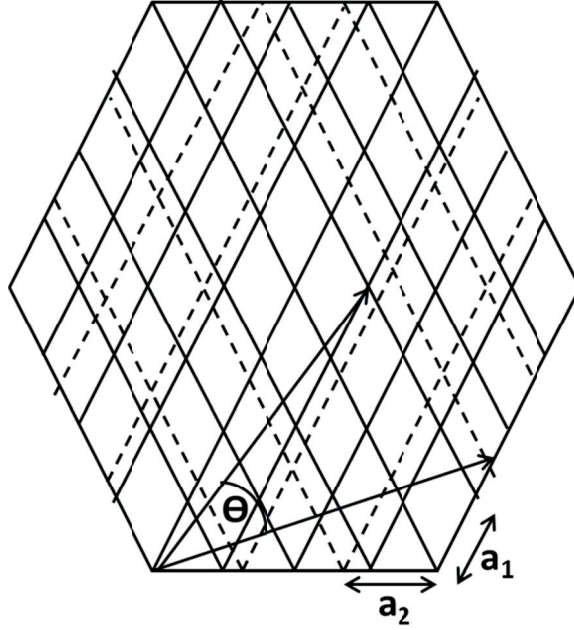


Figure 2.7. Schematic representation of a general grain boundary with different interplanar spacing in each grain for hexagonal systems.

2.3. Energy Minimization

The energy minimization method is one of the most basic and simple technique in computational modeling. It is used to calculate the equilibrium or relaxed state of a system by iteratively changing the positions of the atoms until the desired minimum energy state is reached. But this minimum energy state can be guaranteed only to be a local minimum, not necessarily a global minimum. Mathematically this technique corresponds to solving the equation $\dot{r} = -\nabla_r V$, starting from initial guess $r=r_0$. A Taylor series expansion is used to calculate the energy of a system at slight deviation $\delta\vec{x}$ from \vec{x} ,

$$E(\vec{x} + \delta\vec{x}) = E(\vec{x}) + \frac{\partial E(\vec{x})}{\partial \vec{x}} \delta\vec{x} + \frac{1}{2!} \frac{\partial^2 E(\vec{x})}{\partial \vec{x}^2} (\delta\vec{x}^2) + \dots \quad \text{Eq.2.25}$$

Usually the Taylor series is truncated after the third term to save the computational cost. The first derivative term is called the gradient norm $\vec{g}(\vec{x})$ and the second derivative term is called the Hessian matrix $H(\vec{x})$ as given in Eq.2.26 and Eq.2.27.

$$\frac{\partial E(\vec{x})}{\partial \vec{x}} = \vec{g}(\vec{x}) = \begin{pmatrix} \frac{\partial E(\vec{x})}{\partial x_1} \\ \frac{\partial E(\vec{x})}{\partial x_2} \\ \cdot \\ \cdot \\ \cdot \\ \frac{\partial E(\vec{x})}{\partial x_n} \end{pmatrix} \quad \text{Eq.2.26}$$

$$\frac{\partial^2 E(\vec{x})}{\partial \vec{x}^2} = H(\vec{x}) = \begin{pmatrix} \frac{\partial^2 E(\vec{x})}{\partial x_1 \partial x_1} & \cdot & \cdot & \cdot & \frac{\partial^2 E(\vec{x})}{\partial x_1 \partial x_n} \\ \cdot & \cdot & & & \cdot \\ \cdot & & \cdot & & \cdot \\ \cdot & & & \cdot & \cdot \\ \frac{\partial^2 E(\vec{x})}{\partial x_n \partial x_1} & \cdot & \cdot & \cdot & \frac{\partial^2 E(\vec{x})}{\partial x_n \partial x_n} \end{pmatrix} \quad \text{Eq.2.27}$$

The energy of a system containing n atoms is a function of $3n$ variables. It is not possible to calculate the energy of such a large system analytically. That is why numerical methods are used to calculate the energy of the system. There are several methods available to calculate the minimum energy state. Most commonly used amongst them are Newton Raphson, conjugate gradient method and steepest decent methods. All of these methods use the gradient norm and the hessian matrix. The general algorithms for finding the minimum energy configuration is,

1. Calculate the force for the current configuration of atoms
2. Find a search direction $d^{(n)}$ and a step size $\alpha^{(n)}$
3. Advance the configuration of the system $u^{(n+1)} = u^{(n)} + \alpha^{(n)} d^{(n)}$
4. Continue the loop (steps 1-3) unless force becomes less than a tolerable value.

The difference between different methods lies in the choice of search direction $d^{(n)}$.

2.3.1. Steepest descent method

It is one of the simplest and most robust methods amongst gradient methods for energy minimization [44]. In this method the search direction is opposite to the direction of the force. The iterative equation can be written as,

$$\vec{x}_{k+1} = \vec{x}_k - \lambda_k \nabla E(x_k) = \vec{x}_k - \lambda_k \vec{g}(\vec{x}_k) \quad \text{Eq.2.28}$$

Where, λ_k is the length of the iterative step. A line minimization method is used to determine λ_k . In this method the objective function Φ is minimized with respect to variable α keeping search direction constant for a single step,

$$\Phi(\alpha^{(k)}) = E(\vec{x}^{(k)} + \alpha^{(k)} \vec{d}^{(k)}) \quad \text{Eq.2.29}$$

$$\frac{d\Phi(\alpha^{(k)})}{d\lambda^{(k)}} = \nabla E(x^{(k+1)})^T \frac{dx^{(k+1)}}{d\lambda^{(k)}} = -\nabla E(x^{(k+1)})^T \vec{g}(x^{(k)}) \quad \text{Eq.2.30}$$

For the objective function Φ to be minimum, α should be such that gradient vector is orthogonal to $\nabla E(x^{(k+1)})^T$. The step is taken orthogonal to the gradient vector and length is such that it cuts the energy surface at next iteration point (Figure 2.8). Due to this orthogonal direction the evolution path is a zigzag. The steepest decent method is especially interesting because a trajectory in going from initial to final has a clear physical interpretation.

2.3.2. Conjugate gradient method

In the conjugate gradient method [44], the first portion of the search takes place opposite to the direction of the largest gradient, just as in the steepest descent method. However, to avoid some of the oscillating back and forth that often slows down the steepest descent method as it moves toward the minimum, the conjugate gradient method mixes in a little of the previous direction in the next search (Figure 2.8). This allows the method to move rapidly to the minimum. The atom coordinates in this method are moved as following,

$$\vec{x}_{k+1} = \vec{x}_k - \lambda \vec{h}_k \quad \text{Eq.2.31}$$

$$\vec{h}_k = \vec{g}_k + \alpha_{k-1} \vec{h}_{k-1} \quad \text{Eq.2.32}$$

$$\alpha_{k-1} = \frac{\vec{g}_k \cdot \vec{g}_k}{\vec{g}_{k-1} \cdot \vec{g}_{k-1}} \quad \text{Eq.2.33}$$

Step length λ is determined using the line minimization method as explained in the previous section. The main strength of the method is its faster convergence in

comparison to steepest descent method. In fact, for a harmonic function the maximum number of steps required to reach the minimum using this method is equal to the number of degrees of freedom or variables. Although each step in the conjugate gradient method is more expensive than the steepest descent method, the total number of steps required for convergence might be much lower. Figure 2.8 shows the comparison of the two methods for the same convergence problem.

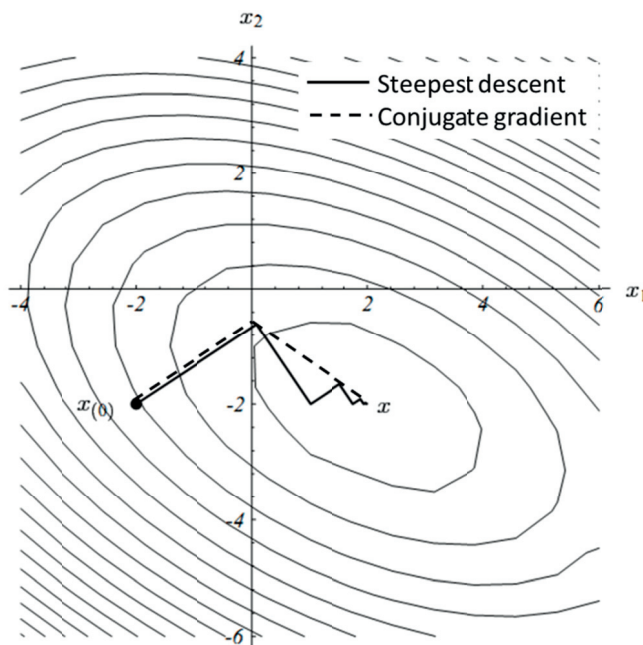


Figure 2.8. In steepest decent method, the search direction is normal to the force, while the conjugate gradient method mixes the previous search direction with the direction of the force to speed up the convergence [44].

2.3.3. Newton Raphson method

It is the most efficient method to converge iteratively to the minimum energy configuration of a large system. The scheme of iteration in this method is as follows,

$$\vec{x}_{k+1} = \vec{x}_k - \frac{\vec{g}(\vec{x}_k)}{H(\vec{x}_k)} \quad \text{Eq.2.34}$$

This method uses the curvature of the energy surface in addition to the gradient of the energy to identify search direction (Figure 2.9). It is more expensive than previous two methods since it requires calculation of hessian matrix at each step. The convergence of the Newton Raphson method increases as we approach the minima. However, the terms in the Hessian matrix are difficult to derive and are computationally costly for molecular force fields. Furthermore, the minimization can become unstable if the initial guess is too far from the minimum. Finally, calculating,

inverting, and storing an $N \times N$ matrix for a large system can become unwieldy. Even taking into account that the Hessian is symmetric and that each of the tensor components is also symmetric, the storage requirements scale as approximately $3N^2$ for N atoms. To remedy this situation, so called Quasi-Newton methods have been developed. These methods calculated the hessian matrix only at specific intervals or when the change in the energy is too large instead of calculating it at each interval. One of the commonly used ones currently is called Broyden-Fletcher-Goldfarb-Shanno (BFGS) algorithm [45].

$$H_{i+1} = H_i + \frac{\vec{x} \times \Delta \vec{g}}{\vec{x} \cdot \Delta \vec{g}} - \frac{(H_i \cdot \Delta \vec{g}) \times (H_i \cdot \Delta \vec{g})}{\Delta \vec{g} \cdot H_i \cdot \Delta \vec{g}} + (\Delta \vec{g} \cdot H_i \cdot \Delta \vec{g}) \cdot (\vec{v} \times \vec{v})$$

Eq.2.35

$$\vec{v} = \frac{\Delta \vec{x}}{\Delta \vec{x} \cdot \Delta \vec{g}} - \frac{H_i \cdot \Delta \vec{g}}{\Delta \vec{g} \cdot H_i \cdot \Delta \vec{g}}$$

Eq.2.36

Note: In practice, for an energy minimization problem, the combination of three methods is used. First few iterations with steepest descent and conjugate gradient method bring the initial guess closer to the minimum energy position and then Newton Raphson is used to increase the rate of convergence.

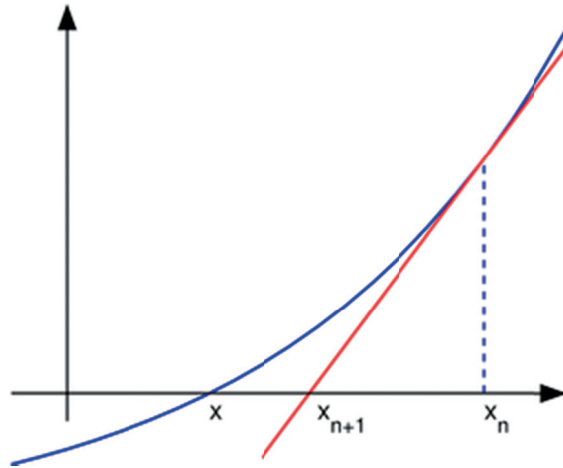


Figure 2.9. Newton Raphson method for energy minimization uses both the force as well as the curvature of the energy surface to find the search direction. It finds the root of the equation ($dE/dx=0$).

2.4. Molecular Dynamics

Molecular dynamics (MD) [46] simulations calculate the time dependent dynamics of a system, thereby dynamical properties such as, transport coefficients, time dependent responses to perturbations, rheological changes etc. It is a very simple method which calculates the position and velocity of the atoms in a system as a function of time using Newton's laws of motion,

$$\dot{\vec{r}}_i = \vec{p}_i / m_i \quad \text{Eq.2.37}$$

$$\dot{\vec{p}}_i = \vec{f}_i \quad \text{Eq.2.38}$$

where, p_i is the momentum, m_i is the mass of atom i , and f_i is the force acting on atom i . The numerical integration of coupled differential equation gives the velocity and position of atoms after each time step. The time step should be short enough to capture the right dynamics of the system. At the same time it can't be too short since it will increase the calculation cost.

There are several algorithms for the step by step integration, but they have to take mainly two points into account. First, it should be able to deal with both long as well as short time scales. Second, calculation of force is expensive; therefore it should be done as infrequently as possible. The most popular algorithm which is used for the numerical integration is velocity Verlet algorithm [47]. It can be written as,

$$\dot{\vec{p}}_i(t + 0.5\delta t) = \vec{p}_i(t) + 0.5\delta t \vec{f}_i(t) \quad \text{Eq.2.39}$$

$$\vec{r}_i(t + \delta t) = \vec{r}_i(t) + \delta t \vec{p}_i(t + 0.5\delta t) / m_i \quad \text{Eq.2.40}$$

$$\dot{\vec{p}}_i(t + \delta t) = \vec{p}_i(t + 0.5\delta t) + 0.5\delta t \vec{f}_i(t + \delta t) \quad \text{Eq.2.41}$$

where, $p_i(t)$, $r_i(t)$ are the momentum and position of atom i at time t , and $f_i(t)$ is the force acting on atom i at time t , and δt is the length of each time step. Important features of the velocity Verlet algorithm are: it is time reversible, symplectic, low order in time, requires just one expensive force calculation per step.

2.5. Nudged Elastic Band

The nudged elastic band (NEB) [48] is a method to find the saddle point and minimum energy path (MEP) between known initial and final states of a system. In this method, the path between initial and final state is represented through several intermediate images (or states) (Figure 2.11), which are connected with an elastic band (springs). The energy minimization of each image leads to the minimum energy

path (Figure 2.11) given that the minimization satisfies two conditions: First, the images should move along the connecting path during energy minimization; second, the distance between all the images remains constant. The difference between the saddle point energy and the initial state gives the activation energy for the transition (Figure 2.10).

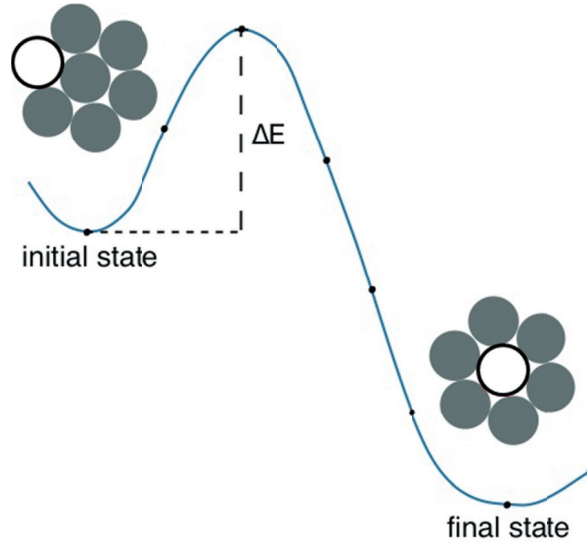


Figure 2.10. Activation energy (ΔE) for a reaction is calculated using nudged elastic band method as the difference of the energy between the saddle point state and the initial state.

Figure 2.11 shows schematically the forces acting on the elastic band during an NEB calculation. In this method, the total force acting on an image is given by

$$\vec{F}_i = -\vec{\nabla} V(\vec{R}_i)|_{\perp} + \vec{F}_i^s \cdot \hat{t}_{\parallel} \hat{t}_{\parallel} + f(\phi_i) \left(\vec{F}_i^s - \vec{F}_i^s \cdot \hat{t}_{\parallel} \hat{t}_{\parallel} \right) \quad \text{Eq.2.42}$$

Where $-\vec{\nabla} V(\vec{R}_i)|_{\perp}$ is the projection of the perpendicular component of the interatomic force $-\vec{\nabla} V(\vec{R}_i)$. Only the perpendicular projection is taken in order to keep a constant distance between the images. It can be written as,

$$\vec{\nabla} V(\vec{R}_i)|_{\perp} = \vec{\nabla} V(\vec{R}_i) - \vec{\nabla} V(\vec{R}_i) \cdot \hat{t}_{\parallel} \hat{t}_{\parallel} \quad \text{Eq.2.43}$$

\hat{t}_{\parallel} is the unit tangent to the connecting path. \vec{F}_i^s is the spring force acting on image i and it is given as,

$$\vec{F}_i^s \equiv k_{i+1} (\vec{R}_{i+1} - \vec{R}_i) - k_i (\vec{R}_i - \vec{R}_{i-1}) \quad \text{Eq.2.44}$$

where, k_i is the spring constant of the spring connecting image i and $(i-1)$. Therefore, second term in the Eq.2.42 is the parallel component of the spring force on image i . Subtracting the perpendicular component of the spring force ensures that the images are not pulled out of the minimum energy path and the projection of only perpendicular component of $\vec{\nabla}V$ ensures the constant distance between the images during energy minimization of the images. This method of manipulating the forces is referred to as ‘nudging’.

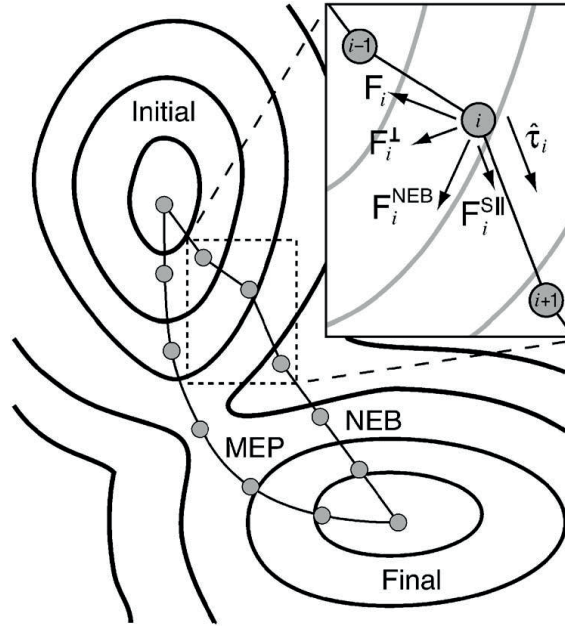


Figure 2.11. NEB is a method to find minimum energy path for the transition from a known initial state to a known final state. The diagrams shows the various forces acting on the elastic band during energy minimization of the elastic band. [49]

When the energy of the system changes very rapidly along the path, but the restoring force perpendicular to the path $-\vec{\nabla}V(\vec{R}_i)|_{\perp}$ is weak, the path can become kinky and the convergence of the minimization can slow down. Third term in the Eq.2.42 is introduced as a remedy to this problem. It is a smooth switching function that gradually turns the perpendicular component of the spring force where the path becomes kinky. The switching function $f(\phi_i)$ is given as,

$$f(\phi) = \frac{1}{2} (1 + \cos(\pi(\cos \phi))) \quad \text{Eq.2.45}$$

ϕ_i is the angle between the adjacent segments of the path at image i . Therefore, it can be written as,

$$\cos \phi_i = \frac{(\vec{R}_{i+1} - \vec{R}_i) \cdot (\vec{R}_i - \vec{R}_{i-1})}{|\vec{R}_{i+1} - \vec{R}_i| |\vec{R}_i - \vec{R}_{i-1}|} \quad \text{Eq.2.46}$$

2.6. Metadynamics

Metadynamics [50] is a method aimed at calculating the free energies and accelerating rare events, e.g. solid state diffusion, crystal structure prediction. One advantage of this method over NEB is that it does not require the a priori knowledge of the initial and final states of the system. It requires identification of control variables (CV's) which can describe the process of interest, e.g. the distance of the diffusing atom from its final position in case of an atomic diffusion problem. Potential energy, distance, angle, coordination number etc. can be used as the CV in Metadynamics. The dynamics in the space of CVs is enhanced by a history dependent potential constructed as a sum of Gaussians centered along the trajectory of the CVs. The dynamics starts at a local minimum and it is pushed towards the desired state by inserting a history dependent biasing potential (Gaussian centered at the current position of the CV) (Figure 2.12) after every interval of a fixed number of steps. The biasing potential helps the system to come out of the potential well through the lowest saddle point and explore the larger energy surface. The sum of these Gaussians added at regular intervals can be exploited to reconstruct the free energy of the process. The small repulsive Gaussian potential is added every τ_G MD steps. Therefore, external potential (Metadynamics biasing potential) acting on the system at time t is given by

$$V_G(S(x), t) = w \sum_{\substack{t' = \tau_G, 2\tau_G, \dots \\ t' < t}} \exp\left(-\frac{(S(x) - s(t'))^2}{2\delta s^2}\right) \quad \text{Eq.2.47}$$

where, $s(t) = S(x(t))$ is the value taken by the CV at time t . w is the height of the Gaussian, and δs is the width of the Gaussian. The basic assumption of the Metadynamics postulated heuristically is that, $\lim_{t \rightarrow \infty} V_G(s, t) \sim -F(s)$, which is used to construct the free energy surface ($F(s)$) of the system.

Accuracy and efficiency of this method depends on the optimum choice of parameters of the Gaussian potential, w , τ_G and δs . If the Gaussians are very deep and broad, the method will be more efficient but less accurate. On the other hand if

the Gaussians are very narrow and shallow, reconstructed free energy profile will be more accurate but it will take a longer time.

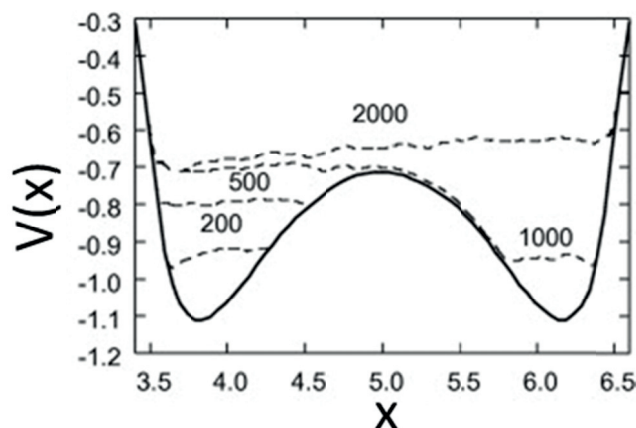


Figure 2.12. Time evolution of the metadynamics potential. Thick solid line is the the starting potential and it is steadily filled with Gaussians (dotted lines). The dynamic evolution is labeled by the number of dynamical iterations. [51]

2.7. Kinetic Monte Carlo

One of the major limitations of the standard molecular dynamic simulations is the approachable time scales. Accuracy of molecular dynamics simulation requires short enough time steps ($\sim 10^{-15}$ s) to resolve the atomic vibrations. Consequently, total simulation time in MD is often less than 1 micro second. However, many real processes of interest, e.g. diffusion, take place on much longer time scales. Kinetic Monte Carlo (KMC) attempts to solve the time scale problem by exploiting the fact that the dynamics of these types of long time scale events proceed through the diffusive steps separated by a migration barrier [52]. Rather than following the trajectory through every vibrational period, this method treats directly the state to state transitions. Therefore KMC is used to simulate the long time scale events which occur typically over a time period of seconds or even longer.

KMC can be applied to the infrequent – event systems, which means that the system spends enough time in an energy basin so that it forgets the history of how it reached into that state. The rate constants k_{ij} are defined for each possible escape route from the present state i to another adjacent energy basin j . Rate constant is k_{ij} characterizes the probability of the escape from the current state i to the state j per unit time. The rate constant is a function of the shapes of the potential basins i and j and the shape of the ridge top connecting state i and j .

Once all the rate constants are known, function R_n is defined as,

$$R_n = \sum_i^j k_{ij} \quad \text{Eq.2.48}$$

R_n is calculated for all the possible transition paths j from i . Then a random number p is drawn between 0 and 1. The transition state j is selected such that $R_{i-1} < pR_n < R_i$. Another random number t is drawn between 0 and 1 and the simulation time is advanced as,

$$\Delta t = \frac{-\ln p}{R_n} \quad \text{Eq.2.49}$$

Where n is the total number of transition paths possible from the initial state i .

The rate constant k_{ij} can be calculated using the harmonic transition state theory as following,

$$k_{ij} = \frac{kT}{h} \frac{\prod_{i=1}^{3N-6} \nu_i^0}{\prod_{i=1}^{3N-7} \nu_i^{TS}} \exp(-\Delta E_a / kT) \quad \text{Eq.2.50}$$

Where, T is the temperature, k is the Boltzmann's constant, h is the Planck's constant, E_a is the migration barrier of the diffusive jump from state i to j , ν_i^0 and ν_i^{TS} are the vibrational frequencies at the transition state and the ground state, respectively.

2.8. Summary of the methods used in the present work

The methods described in the previous sections have been used to simulate different problems in the current study. All the calculations in the present work have been performed using the force field method and atomic description of the system. Atomic description of the systems in combination with the force field method is a pragmatic approach to simulate more real systems with hundreds of atoms, when compared to the first principle electronic calculations which can deal with much smaller systems. However, there is equally strong limitation of not being able to describe the chemical bonds using the force field approach, which limits the types of the situations which can be simulated using this method. In the following chapters the strength of these methods has been demonstrated by showing the capability of these methods to address variety issues. A simple method like energy minimization gives useful insights into the issues of grain boundary segregation of cation dopants and anion impurities in alumina (chapters 3, 4 and 6). It is due to the more pragmatic

and simplistic approach that grain boundaries close to the real systems (near coincidence grain boundaries) with large area could be simulated in the present study to compare with experimental results of the grain boundary segregation in alumina (chapter 6). Nudged elastic band method and Metadynamics were used to calculate the migration barriers of oxygen diffusive jumps in alumina, which are rarely occurring events and difficult to simulate using standard molecular dynamics simulations (chapter 5). Kinetic Monte Carlo was used to link the experiments with the simulations by using the migration barriers to calculate the diffusion coefficients which are measured experimentally (chapter 5). In the end molecular dynamics method was used to simulate the adsorption behavior of polymer dispersants on alumina surfaces (chapter 7).

3. Dopant Segregation in Codoped α -Alumina

The following chapter gives the results of a study on the segregation of dopants to the surfaces and grain boundaries in the polycrystalline α -alumina, with the aim of contributing to the improvement of their transparency. Codoping implies the doping of alumina with combination of dopants, e.g. La-Y, Y-Mg, La-Mg. The chapter discusses in detail the segregation energies of several dopant combinations and its comparison with single doping cases, effect of codoping on interfacial atomic structures, changes in the coordination number at the grain boundaries, and the possibility of a coupling effect due to the codoping.

3.1. Introduction

Since the discovery of translucent polycrystalline alumina (LucAlOx) by Coble [53] in 1962, efforts have been made to achieve transparent polycrystalline alumina in many research groups for the last few decades [54,55,56,57]. In addition to its excellent mechanical properties and chemical stability at high temperatures, the possibility of large flat sheets and curved shapes makes it a potential material for a wide variety of transparent applications; e.g. watches, jewelry, wave guides, armors, high temperature windows [58] and metal-halide lamps [59]. It has been well established that fully dense (99.99%) ultrafine grained alumina is necessary to achieve high real in-line transmittances (RITs) due to its birefringence [55,57,60]. Therefore, it is necessary to achieve maximum densification with minimum grain growth in the final stages of sintering. Various rare earth elements (La, Mg, Y) have been employed in the literature as sintering aids/dopants for the sintering of transparent alumina [56,57,61]. These dopants segregate to the grain boundaries, thereby reducing the rate of densification as well as grain size/sintered density ratio [62,63]. Recently, codoping of alumina with rare earth elements (e.g. La-Y, Y-Mg, Mg-La) has been reported to further reduce the creep rates [64,65] as well as to

increase the real inline transmittance [56] in alumina, work carried out in our laboratory. However, different atomistic mechanisms [61,66] have been proposed in the literature for the role of dopants in the sintering and strengthening effects and the issue is still far from settled.

Codoping can affect the properties of alumina by changing its microstructural features and/or transportation mechanisms. Song and Coble [67] found that codoping with Mg in addition to Ca or Si gives an equiaxed grain structure in contrast to the platelike/abnormal grain structure when doped singly with Ca or Si. Song and Coble [68] also proposed a charge balance and strain balance condition for the appearance of platelike abnormal grains in codoped alumina. Swiatnicki et al. [69] reported that segregation of Mg to grain boundaries is suppressed when codoped with larger and higher charge cations like Ti, which was also supported by the ab-initio simulation study of Elsässer and Elsässer [70]. Depletion of Mg was attributed to the “site competition” effect between Mg and the dopants or impurities of higher valence at grain boundaries.

Lartigue et al. [65] claimed that the constitutive laws change in high temperature deformation of alumina by Mg-Y codoping, i.e. yttrium segregates strongly to the grain boundaries and strengthens Mg doped alumina, which is more pronounced under tension than under compression. Gavrilov et al. [71] studied the Si-Mg codoped system and found that the grain boundary concentration of both ions is reduced by a factor of 5 or more over single doping. Additionally, codoping increases the mutual bulk solid solubility of the dopants, an effect which has also been studied by Dillon et al. [72] who used atomistic modeling, and by Elsässer and Elsässer [70] who did an ab-initio study. The beneficial effect of MgO addition in controlling the microstructure of Si containing alumina was attributed to its ability to redistribute Si ions from the grain boundaries to the bulk.

There have been two competing theories to explain the beneficial effect of codoping over single doping in the literature. Lartigue et al. reported that segregation of Y to the grain boundaries impedes the accommodation of the dislocation at the grain boundaries, which enhances the creep resistance of Mg-Y codoped alumina. The detailed microstructural study was conducted to show that the proportion of coincidence site lattice (CSL) and/or coincidence axis direction (CAD) boundaries increases in codoped alumina [73]. But the claims of the formation of the special boundaries were contradicted by Cho and co-workers [74], who showed that the misorientation distribution doesn't change significantly in Y doped alumina in comparison to undoped alumina and the proportion of CSL boundaries was very low (1-5%) in Y- doped as well as undoped alumina.

Harmer and coworkers [64,75,76] conducted an extensive study to understand the beneficial effect of codoping on grain size in alumina and concluded it to be primarily

a solid solution effect, as after precipitation, no further improvement with increasing dopant concentration was observed. They reported enhanced creep resistance in Nd-Zr codoped alumina compared to singly doped alumina due to cosegregation of both the dopants. It was postulated that different sized cations can produce a better packing at the interface and thereby reduce the free volume for grain boundary transport. Therefore, disparity of cation size was thought to be the main reason for additional effects of codoping on enhancing creep resistance. This logic was further strengthened by the findings of their simulation studies [75]. They calculated the voronoi cell volumes of the voids at the two simple grain boundaries ($\Sigma 3$ and $\Sigma 13$) and compared it with the voids in the bulk alumina. It was shown that the monomodal size distribution of cation substitutional sites volume of the bulk is broken into a bimodal distribution on the low index $\Sigma 3$ grain boundary. On the other hand for a higher index grain boundary $\Sigma 13$, several potential substitutional sites with varying sizes, many larger than the corresponding bulk sites are created at the grain boundary. Therefore, dopants with different sizes can segregate easily to these sites and pack the interface efficiently at higher index grain boundaries. They also introduced the concept of complexion to explain the grain boundary structural changes due to the segregation of dopants [77]. Complexion is a separate phase, which can be made to transform into different complexions (phases) with vastly different properties by chemistry and heat treatment, which is not stable as a bulk phase. Depending on the dopant type and content, grain boundary complexion changes and consequently the grain boundary mobility is also affected. [78]

Elsässer and Elsässer [70] conducted several ab-initio studies of codoping at the rhombohedral twin grain boundary of alumina and reported that there is an energetic gain for cosegregation of aliovalent cations (bivalent/tetravalent) in comparison to single dopant segregation, while there is no or negative energetic gain for cosegregation of isovalent (trivalent) cations. The Mg-Si dopant pair slightly prefers to arrange on nearest neighbor sites parallel to the rhombohedral plane, suggesting a minor coupling effect. They also reported that codoping of alumina with trivalent ions in addition with bivalent/tetravalent ions can improve the covalent bonding in alumina since trivalent ions are accommodated chemically better than bivalent or tetravalent cations.

In the present study we will focus on Y, La and Mg codoping. Since the bulk solubility of both Y and La is very low (≤ 10 ppm) we assume that bulk interactions between the dopant have only minimal effect and we will therefore focus on surface and grain boundary structures. Ab-initio studies being computationally expensive, only small systems with a few 100 atoms can be calculated. Using classical atomistic modeling methods based on empirical potentials provides an opportunity to consider larger systems as well as larger a configurational space with lower computational cost. In previous studies [79,80] it has been shown that satisfactory agreement between

classical atomistic calculations and experimental as well as first principle results can be reached for alumina (less than 3% in atom positions for a $\Sigma 3$ grain boundary). The current simulation study aims to improve the understanding of the atomistic mechanisms behind doping and codoping using classical atomistic modeling methods. Energy minimization methods based on empirical potentials have been used to calculate relaxed surfaces and grain boundaries. The effect of doping and codoping has been studied on 9 surfaces and 8 grain boundaries for three codoping combinations: La-Y, La-Mg and Mg-Y. Segregation of dopants was observed to be energetically favorable in all the cases and a specific coordinative arrangement was observed in case of La-Y codoping. These results give interesting insights into interfacial energies and consequent grain growth for better control of microstructures towards transparent ceramics.

3.2. Approach

Energy minimization method was used to calculate the doped and undoped equilibrium interface energies and structures. Born model for solids, which has been explained earlier in chapter 2, was used to represent the energy surface of the alumina surfaces and grain boundaries. METADISE [81] was used for all the energy minimization calculations in the present work. The Born model describes interatomic forces in terms of pair potentials. A pair potential consists of an electrostatic potential and short range attractive as well as repulsive forces. In addition, the core-shell model by Dick and Overhauser [82] has been used to take into account the polarizability of oxygen ions. The potential parameters developed by Lewis and Catlow [83] were used in the present work and the initial alumina crystal structure has been taken from the work of Liu et al. [84]. Nonpolar surface cuts were generated at different depths along the same surface normal and the lowest energy cut was chosen to create the final relaxed surface atomic structure. To create the mirror twin grain boundaries, two surfaces are put back to back allowing a rigid shift in the grain boundary plane. The minimum energy relative position of the two half crystals is chosen to create the final grain boundary structure. For surfaces as well as grain boundaries, 2D Periodic boundaries are applied in the plane parallel to the interface. In the direction perpendicular to the interface, a two region model is applied where ions within ~ 9 Å from the interface are allowed to relax while the rest of the ions are kept fixed during energy minimization (For details see chapter 2). The bulk as well as the interface atomistic structures produced using the current method have been shown to be in good agreement with ab initio as well as experimental results.

In order to reduce the otherwise large number of possible codoping configurations, energy minimization was performed only on what were estimated to be the highest probability configurations. First, interface Al ions within a certain distance of the

interface were substituted one by one with the different dopants and the substitutional energy for each site was calculated for each dopant separately (Figure 3.1a). The probabilities for a specific site and a dopant were then calculated as follows: $[\exp(\Delta E_i)/\sum \exp(\Delta E_i)]$. ΔE_i is the energy of the site i (E_i) minus the energy of the farthest site from the interface. The probability of a specific multiple dopant configuration was then estimated as the product of the probabilities of each occupied site assuming the probability of each single site to be mutually independent (Figure 3.1b). For codoping, the probability of a particular codoping configuration is considered to be the product of the respective single dopant configurations as illustrated in Figure 3.1c. For each dopant concentration, energy minimization was then done for 150 configurations with the highest estimated probabilities.

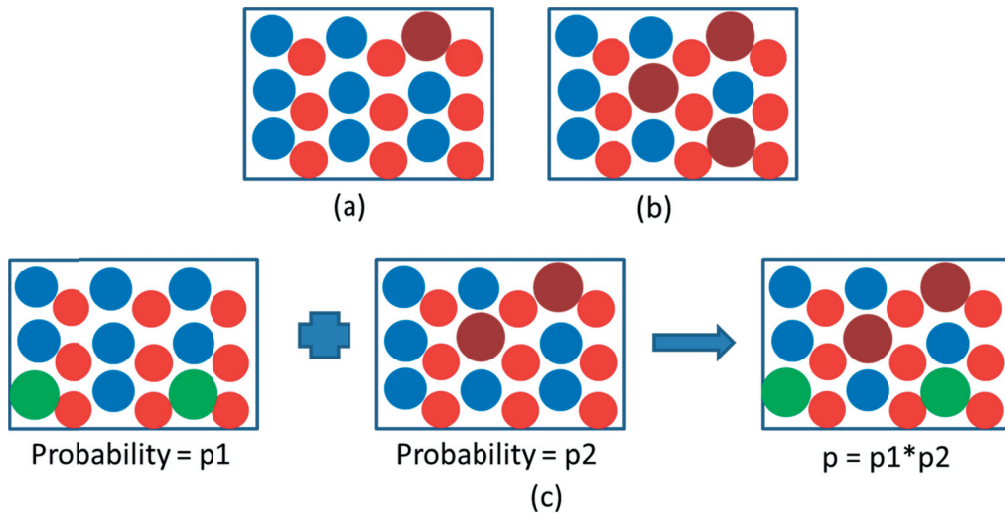


Figure 3.1. (a) single site substitution, (b) permutation of lowest energy sites for multiple dopant configurations, (c) codoping configuration as a combination of respective single dopant configurations

In the case of the divalent dopant Mg, one oxygen vacancy has to be created for every two dopant ions for charge neutrality. For a pair of Mg dopants, there are a large number of possible oxygen vacancy positions. In order to address this problem, the interface width was divided in slabs of widths of 2 Å. In the calculations it was found that there is no association of vacancies with bivalent dopants, which justifies the choice of a small slabs to reduce the computational cost. For a certain pair of divalent dopant ions in a slab, oxygen vacancies were created only in the same slab. Thereafter, the probabilities for Mg sites as well as vacancy sites were calculated in a similar fashion as for trivalent dopants. The lowest energy Mg sites and vacancy sites

were permuted in order to get the lowest energy configurations of multiple Mg doped alumina interfaces.

In order to check the accuracy of the configuration probability estimation, energy minimization was also performed on 1000 and 1500 randomly chosen configurations for trivalent and bivalent dopants respectively. A random number generator was used to choose the random cation sites on the interface. The Al atoms on the randomly chosen cation sites were substituted by the dopants and the energy of the configuration was calculated. The calculations were done for singly doped as well as codoped alumina surfaces and grain boundaries. The results show that the screening procedure adopted in the present work was able to capture the minimum energy configurations, while the energy of the random configurations was always higher as shown by a few representative examples in Figure 3.2.

The segregation energy of the codoping was calculated using the expression:

$$\Delta H_{seg}(N_Y + N_{La}) = \frac{(H(N_Y + N_{La}) - H(0) - N_Y \Delta H_{Y,bulk} - N_{La} \Delta H_{La,bulk})}{(N_Y + N_{La})} \quad \text{Eq.3.1}$$

$$\Delta H_{seg}(N_{Mg} + N_{La}) = \frac{1}{(N_{Mg} + N_{La})} \left(H(N_{Mg} + N_{La}) - H(0) - N_{La} \Delta H_{La,bulk} - N_{Mg} \Delta H_{Mg,bulk} - \frac{N_{Mg}}{2} \Delta H_{Ovac,bulk} \right) \quad \text{Eq.3.2}$$

$\Delta H_{seg}(N)$ is the enthalpy of segregation in a structure containing N dopant ions, $H(N)$ is the potential energy of the structure containing N dopant ions, and $\Delta H_{i,bulk}$ is the change in the enthalpy when inserting a dopant ion i in the bulk. $\Delta H_{Ovac,bulk}$ is the energy of creating an oxygen vacancy in the bulk alumina. For Y-La codoping, a total 9 surfaces and 8 grain boundaries were considered. All the grain boundaries were mirror twin grain boundaries of the same indices as the surfaces. (110) surface is parallel to a mirror plane of the crystal and therefore a (110) mirror twin grain boundary is equivalent to the bulk alumina. For Mg-La and Mg-Y codoping, 5 surfaces and the corresponding 4 mirror twin grain boundaries were studied. A brief summary of the grain boundaries and surfaces calculated in the present work is given in Table 3.1.

Additionally, since it was impossible to explore all possible combinations of dopant concentrations, we restricted ourselves to the case of equal dopant concentration for both the dopants.

3. Dopant segregation in codoped [alpha]-alumina

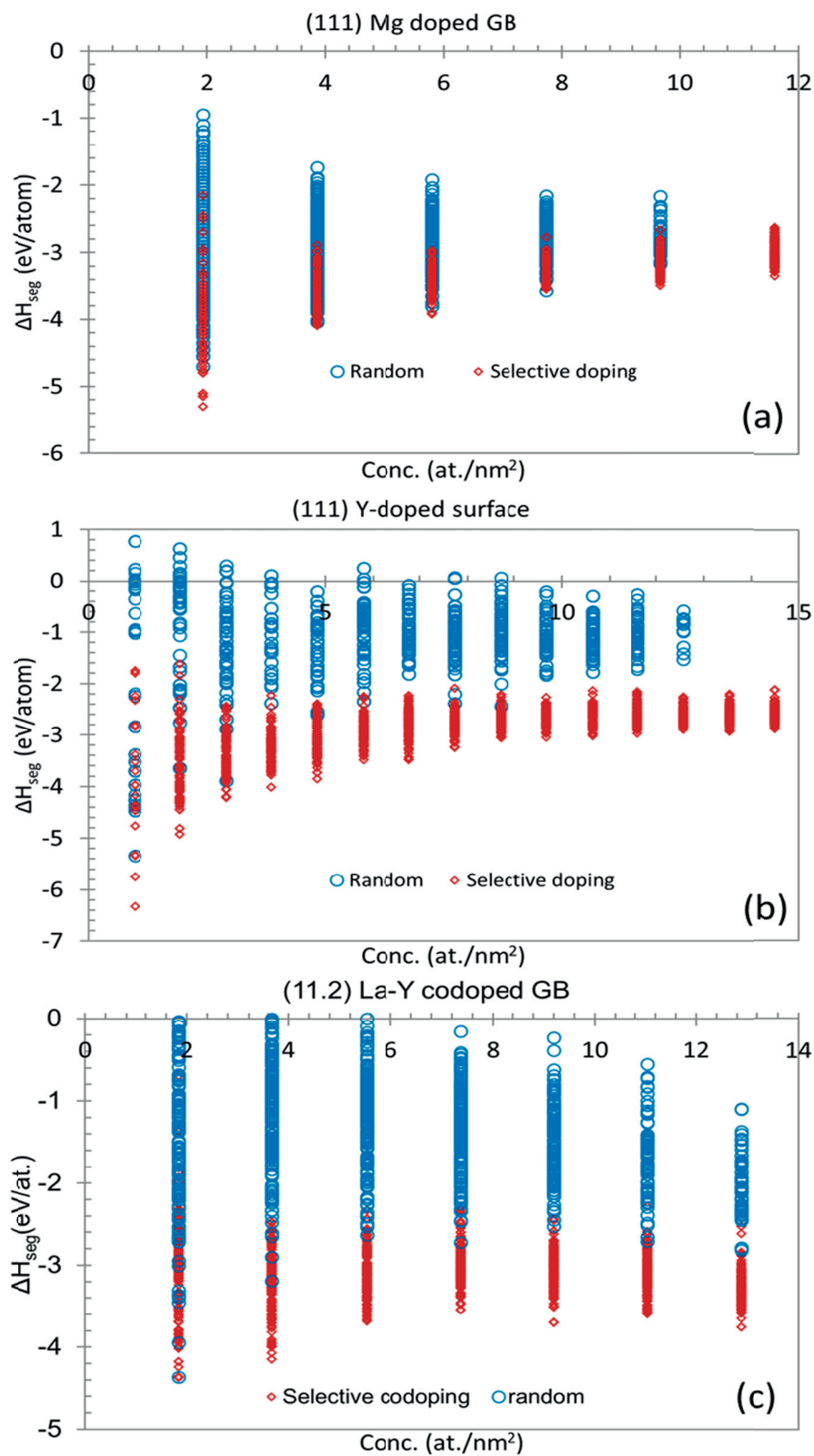


Figure 3.2. Comparison of probabilistic codoping with randomly chosen configurations, (a) Mg doped, (b) Y doped, and (c) La-Y doped

Table 3.1. Sigma values of the twin grain boundaries, surface area (A) of the cells used for the calculations and interfacial energies of grain boundaries (γ_{GB}) and surfaces (γ_{surf}) calculated in the present work. Sigma values is the ratio of the lattice points in the unit cell of coincident site lattice and the original lattice.

Miller indices	Σ	γ_{surf} (J/m ²)	γ_{GB} (J/m ²)	A (nm ²)
(00.1)	3	2.99	2.66	0.7713
(01.2)	7	2.62	0.27	0.7020
(10.0)	3	2.89	0.5	0.5866
(11.2)	7	3.44	2.85	1.0867
(10.1)	11	3.67	1.88	0.6175
(11.0)	-	3.02	-	1.0160
(11.3)	13	3.20	2.42	1.1691
(22.3)	43	3.18	2.95	2.1127
(11.1)	93	3.48	2.87	1.0341

In order to characterize the atomic arrangement at the interface a coordination number (CN) was determined by counting the number of atoms within a cut off radius. Cut off radii were taken [63,85] as Y-O: 2.9 Å, La-O: 3.1 Å, Mg-O: 2.7 Å, Y-Y: 4.54 Å, Y-La: 4.65 Å, La-La: 4.76 Å. Cut off radii were determined as the centre of the nearest neighbor and second neighbor distance where the coordination number remains constant for a certain range of cut off radius.

3.3. Theoretical Consideration

3.3.1. Mackrodt and Tasker formula derivation for codoping

Whereas the case of single doping has been studied quite extensively and an expression for the ratio between the interface (X^i) and bulk cationic ratio (X^b) as a function of the segregation energy (ΔH_{seg}) has been developed by Mackrodt and Tasker [86], the case of codoping has, to my knowledge, not been looked at thoroughly from a theoretical standpoint. However an expression for X^i/X^b very similar to the case of single doping can be derived analogically to the Mackrodt and Tasker derivation for single doping.

If we, in analogy to the derivation of the Mackrodt and Tasker formula for one dopant [86], consider a semi-infinte crystal containing two types of dopants ($D1$ and $D2$) and a single interface as the sole defect (whether the interface is a surface or a grain boundary is unimportant for the following discussion). Let us for sake of

simplicity only consider dopants with a valance of +3 (such as Y and La) which replace the Al ion in the α -alumina structure. In analogy to the single doped case the total free energy G of the system can then be defined as:

$$G = \left(N_{Al}^b g_{Al}^b + N_{D1}^b g_{D1}^b + N_{D2}^b g_{D2}^b + N_O^b g_O^b + N_{Al}^i g_{Al}^i \right. \\ \left. + N_{D1}^i g_{D1}^i + N_{D2}^i g_{D2}^i + N_O^i g_O^i - TS_{config}^b - TS_{config}^i \right) \quad \text{Eq.3.3}$$

The superscript b indicates the bulk and i the interface structure; subscripts Al , $D1$, $D2$ and O indicate the aluminum, the two dopants and the oxygen ion in the system. N indicates the number of ions, g the individual free energy per ion and S_{config} is the configurational entropy. On the oxygen sublattice the configurational entropy is zero as there is only one type of ion. On the aluminium sublattice, if we assume the dopant ions to be randomly and uniformly distributed on the aluminium sites, the configurational entropy for the bulk as well as the interface can be defined as follows:

$$S_{config}^{b/i} = k \ln \frac{(N_{Al}^{b/i} + N_{D2}^{b/i} + N_{D1}^{b/i})!}{(N_{Al}^{b/i} + N_{D2}^{b/i})! N_{D1}^{b/i}!} \cdot \frac{(N_{Al}^{b/i} + N_{D2}^{b/i})!}{N_{Al}^{b/i}! N_{D2}^{b/i}!} = k \ln \frac{(N_{Al}^{b/i} + N_{D2}^{b/i} + N_{D1}^{b/i})!}{N_{Al}^{b/i}! N_{D1}^{b/i}! N_{D2}^{b/i}!} \quad \text{Eq.3.4}$$

If we now define $N_s = N_{Al} + N_{D1} + N_{D2}$ as the total number of sites of the aluminium sublattice and use the Stirling approximation ($\ln(n!) = n \ln(n) - n$ for large n), the configurational entropy can be expressed as:

$$S_{config}^{b/i} = k \ln \left[\frac{N_s^{b/i} \ln N_s^{b/i} - (N_s^{b/i} - N_{D1}^{b/i} - N_{D2}^{b/i}) \ln (N_s^{b/i} - N_{D1}^{b/i} - N_{D2}^{b/i})}{N_{D1}^{b/i} \ln N_{D1}^{b/i} - N_{D2}^{b/i} \ln N_{D2}^{b/i}} \right] \quad \text{Eq.3.5}$$

We can now introduce this expression of the configurational energy- entropy? into the expression of G . At equilibrium we have $\partial G / \partial N_{D1}^i = 0$. Accordingly if we take the derivative of the total free energy and by supposing that the only two individual free energies that are dependent on N_{D1}^i are g_{D1}^i and g_{D2}^i we finally get:

$$X_{D1}^i = X_{D1}^b \cdot e^{-\frac{\Delta G_{seg}^{D1}(X_{D1}^i, X_{D2}^i) + X_{D1}^i \left(\frac{\partial \Delta G_{seg}^{D1}}{\partial X_{D1}^i} + X_{D2}^i \left(\frac{\partial \Delta G_{seg}^{D2}}{\partial X_{D1}^i} \right) \right)}{kT}} \quad \text{Eq.3.6}$$

Where $\Delta G_{seg}^{D1} = g_{D1}^i - g_{Al}^i - g_{D1}^b + g_{Al}^b$ and $\Delta G_{seg}^{D2} = g_{D2}^i - g_{Al}^i - g_{D2}^b + g_{Al}^b$ and $X_{D1} = N_{D1}/N_{Al}$ and $X_{D2} = N_{D2}/N_{Al}$. If we now assume the vibrational segregation entropy to be negligible based on calculations done by P. Masri et al. [87], the free energy of segregation ΔG_{seg} can be approximated by ΔH_{seg} and we end up with the final expression:

$$X_{D1}^i = X_{D1}^b \cdot e^{-\frac{\Delta H_{seg}^{D1}(X_{D1}^i, X_{D2}^i) + X_{D1}^i(X_{D1}^i + 1) \frac{\partial \Delta H_{seg}^{D1}}{\partial X_{D1}^i} + X_{D2}^i(X_{D1}^i + 1) \frac{\partial \Delta H_{seg}^{D2}}{\partial X_{D1}^i}}{kT}} \quad \text{Eq.3.7}$$

3.3.2. Codoping versus single doping segregation energies

As seen from the Eq.3.7 the biggest difference to the case of single doped segregation is that the expression for codoping is also dependent on the change of the segregation energy of the second dopant with respect to the dopant concentration of the first.

Since we restricted ourselves to equal interfacial dopant concentrations in this work we can set $X_{D,tot}^i = X_{D1}^i + X_{D2}^i$ and $X_{D1}^i = X_{D2}^i = 0.5 \cdot X_{D,tot}^i$. If additionally we consider the case where codoping is neither energetically favorable nor unfavorable and hence the segregation energy of a dopant is only dependent on the total dopant ionic ratio ($X_{D,tot}^i$) at the interface and not on the individual ratios of each dopant (X_{D1}^i and X_{D2}^i) we can simplify Eq.3.7 as below,

$$0.5 \cdot X_{D,tot}^i = X_{D1}^b \cdot e^{-\frac{\Delta H_{seg}^{D1}(X_{D,tot}^i) + 0.5 \cdot X_{D,tot}^i(0.5 \cdot X_{D,tot}^i + 1) \frac{\partial \Delta H_{seg}^{D1}}{\partial X_{D,tot}^i} + 0.5 \cdot X_{D,tot}^i(0.5 \cdot X_{D,tot}^i + 1) \frac{\partial \Delta H_{seg}^{D2}}{\partial X_{D,tot}^i}}{kT}} \quad \text{Eq.3.8}$$

For the sake of discussion let us suppose that the shape of the ΔH_{seg} vs. X^i curves for the different dopants are very similar and hence the derivative of both ΔH_{seg}^{D1} and ΔH_{seg}^{D2} with the total dopant concentration to be about equal. According to our results, this assumption is not too far off (see Figure 3.3, Figure 3.4).

$$\left(\begin{aligned} &0.5 \cdot X_{D,tot}^i (0.5 \cdot X_{D,tot}^i + 1) \frac{\partial \Delta H_{seg}^{D1}}{\partial X_{D,tot}^i} \\ &+ 0.5 \cdot X_{D,tot}^i (0.5 \cdot X_{D,tot}^i + 1) \frac{\partial \Delta H_{seg}^{D2}}{\partial X_{D,tot}^i} \end{aligned} \right) \approx X_{D,tot}^i (X_{D,tot}^i + 1) \frac{\partial \Delta H_{seg}^{D1}}{\partial X_{D,tot}^i} \quad \text{Eq.3.9}$$

With this assumption we can see, that the derived expression (Eq.3.8) is very similar to the case of single doping (Eq.3.10), (see Mackrodt and Tasker [86] for more details) except for the factor of 0.5 in front of the interfacial dopant concentration. This means that at the same bulk concentration of dopant one X_{D1}^b , we have a higher total interfacial dopant concentration $X_{D,tot}^i$. This again means that, if we assume there are no interactions between the dopants in the bulk because of their low concentration (≤ 10 ppm for La and Y) and hence the bulk solubility of both dopants being the same in the case of single doping and codoping, we have a higher total interfacial dopant concentration at the solubility limit in the case of codoping than in the case of single doping. The reason for this is the additional configurational entropy of having two instead of only one dopant as derived in the previous section.

$$X_{D,tot}^i = X_{D1}^b \cdot e^{-\frac{\Delta H_{seg}^{D1}(X_{D,tot}^i) + X_{D,tot}^i(X_{D,tot}^i + 1) \frac{\partial \Delta H_{seg}^{D1}}{\partial X_{D,tot}^i}}{kT}} \quad \text{Eq.3.10}$$

For the case discussed above (i.e. neither favorable nor unfavorable interactions between $D1$ and $D2$), we should observe a codoping segregation energy ΔH_{seg} , which is the average of the segregation energies of $D1$ and $D2$ (i.e. $\Delta H_{seg} = 0.5 \cdot \Delta H_{seg}^{D1} + 0.5 \cdot \Delta H_{seg}^{D2}$). In the following discussion we will hence consider any calculated ΔH_{seg} below $(0.5 \cdot \Delta H_{seg}^{D1} + 0.5 \cdot \Delta H_{seg}^{D2})$ to be indicative of favorable interactions between the dopants of different types. Any ΔH_{seg} above that value would indicate unfavorable interactions such as, e.g. site competition between $D1$ and $D2$.

3.4. Results and Discussion

3.4.1. Segregation Energies

3.4.1.1. La-Y Codoping

9 surfaces and 8 grain boundaries were calculated for Y-La codoping. For all dopant concentrations, single doped and codoped, the segregation energies are negative as listed in Table 3.2. Therefore, segregation to the surfaces and grain boundaries is energetically favorable for all systems studied. Segregation energy for La-Y codoping varies from -2.14 to -5.25 eV/atom for surfaces and from -1.57 to -4.27 eV/atom for different grain boundaries, which indicates stronger segregation on surfaces than GB's. It should be noted that the segregation energies calculated for Y in the present work are slightly more negative (0.5-1.0 eV/atom) in comparison to the energies calculated in previous work [79] due to the more efficient method of selecting low energy configurations, especially at higher dopant concentrations. However the general behavior, i.e. often observed important energy minima, does not change. It may lead to higher solubility of dopants at interfaces than was calculated earlier [80].

Figure 3.3 and Figure 3.4 show the representative segregation energy plots for La-Y codoped alumina surfaces and grain boundaries respectively. Codoping segregation energy for La-Y codoped surfaces increases continuously for low concentrations and reaches a constant value of -2.14 to -5.25 eV at a dopant concentration of about ~6-8 atoms/nm² (Figure 3.3). Analysis of the simulated atomistic structures shows that 6-8 atoms/nm² is the dopant concentration which is required for the complete coverage of the surface Al sites with dopants, after which Al surface sites are no longer available to be substituted by the dopants. As the interface Al sites are filled up, the sites that remain available become energetically less favorable and hence the asymptotic value of segregation energy is reached after this concentration.

In the case of Y-La codoped grain boundaries, segregation energy for codoping neither decreases nor increases for (00.1) GB. For other low Σ grain boundaries, ((01.2), (10.0), (10.1)), segregation energy decreases with concentration (Figure 3.4). A minima is observed for the (01.2) GB at 6- 8 atoms/nm² dopant concentration and a change in the slope is observed for the (10.0) GB around the same concentration. For the higher Σ GBs (i.e. (11.1), (11.2), (11.3), (22.3)), the segregation energy for codoping increases with dopant concentration and approaches a constant value from 6-8 atoms/nm² similar to the surfaces. This concentration is similar to the concentration corresponding to minimas observed in the case of low index grain boundaries (6-8 at./nm²). One possible explanation for the decreasing segregation energy with increasing concentration in the case of low index grain boundaries might be that pure interfaces are closely packed and therefore can't accommodate larger size cations. With increasing dopant concentration, interface atomic rearrangement takes place. This rearrangement leads to more open interface structures favoring segregation. After a critical concentration, atomic rearrangement no longer remains energetically favorable, the GB is saturated and the segregation energy remains constant. On the other hand, high index grain boundaries are more disordered and hence, have a more open interfacial atomic structure. As the dopant atoms gradually segregate to the grain boundary, they start filling up the voids and makes the accommodation of more dopants difficult, which reaches a saturation point after a certain concentration.

To compare segregation energies of codoped interfaces with single doping, a curve corresponding to $[\Delta H_{seg,min}(D1,C) + \Delta H_{seg,min}(D2,C)]/2$ is shown in the segregation energy plots, where $\Delta H_{seg,min}(D1,C)$ is the minimum segregation energy of singly doped interface at a concentration C of dopant $D1$ (Figure 3.3 and Figure 3.4). As discussed in the section 2.2, the codoped configurations, which have segregation energy below this curve, are energetically more favorable than single doping. Only (10.0) and (22.3) surfaces have slight energetic gain over single doping (Figure 3.4). For grain boundaries energetically favorable interactions have only been observed for the (01.2) grain boundary (Figure 3.4), possibly due to the specific ordering of the dopants on this specific grain boundary that will be discussed further in the section 3.4.5. All other Y-La codoped surfaces and grain boundaries have no clear energetic gain/loss over single doping as shown through some representative segregation energy plots in Figure 3.3 and Figure 3.4. In general, therefore there is no conclusive favorable/unfavorable interaction between La and Y dopant ions at codoped interfaces.

3. Dopant segregation in codoped [alpha]-alumina

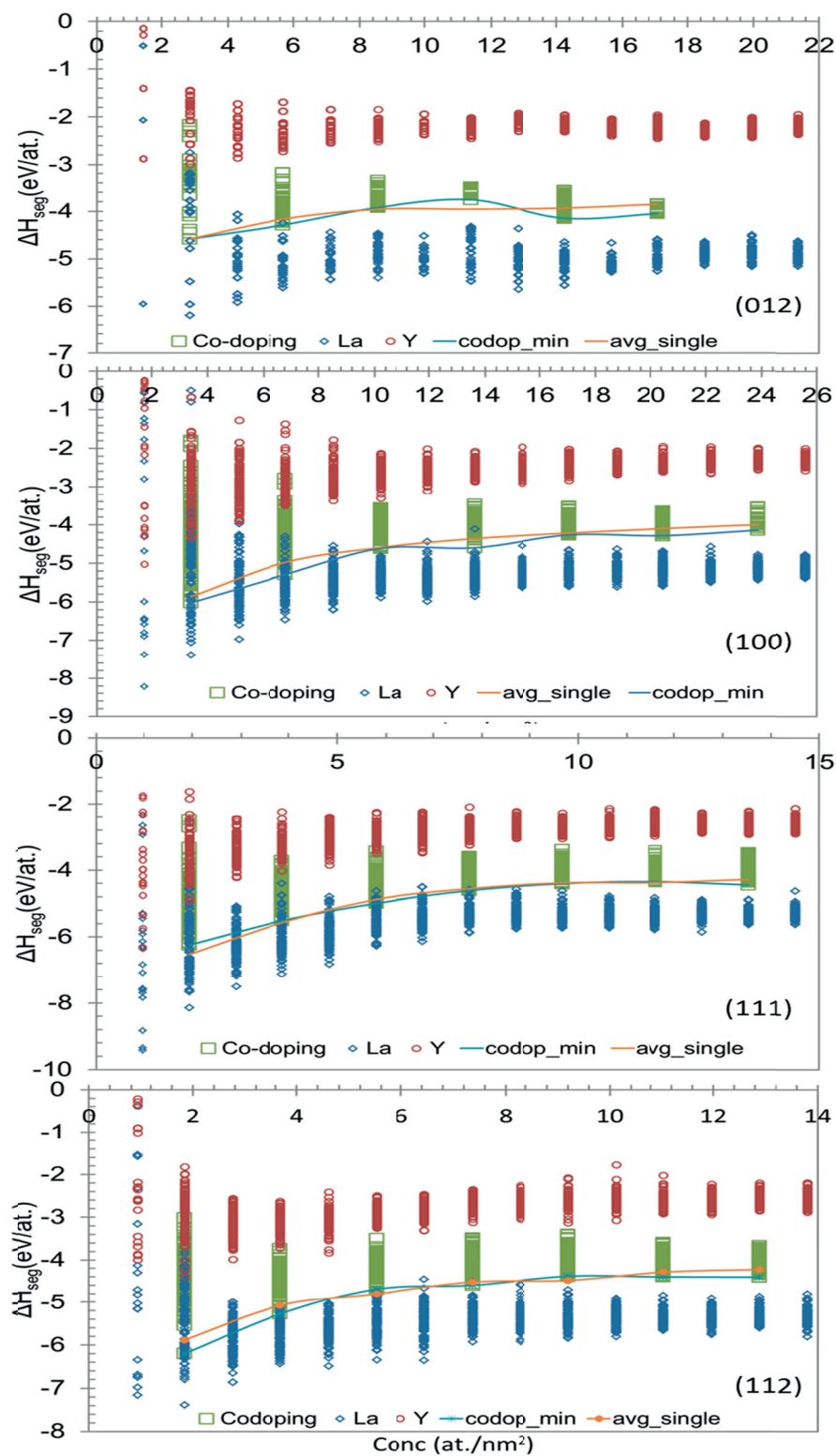


Figure 3.3. Representative segregation energy plots for La-Y codoped surfaces. The lines serve as visual guides only.

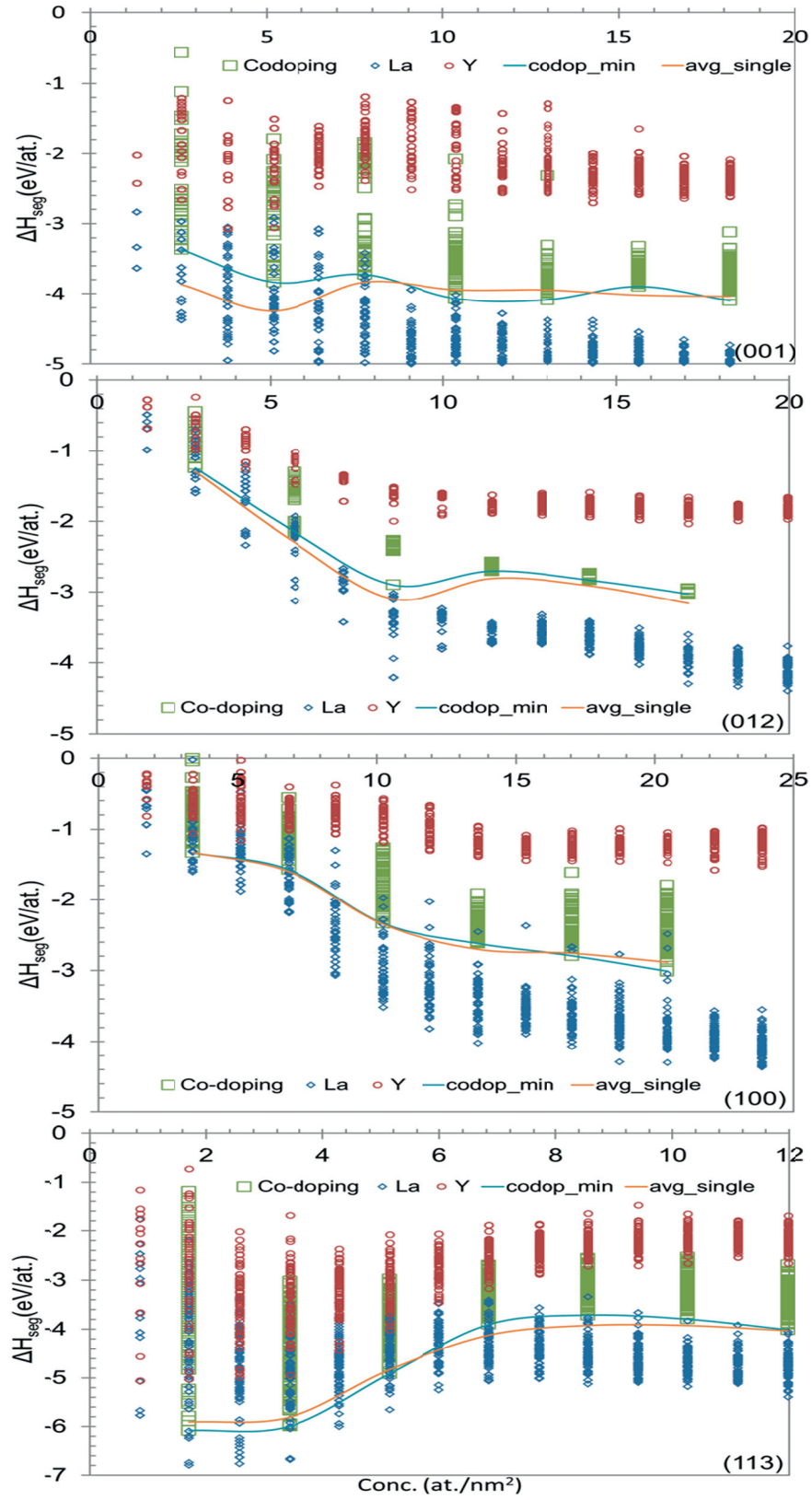


Figure 3.4. Representative segregation energy plots for La-Y codoped GB's. The lines serve as visual guides only.

Table 3.2. Asymptotic/local minimum Segregation energy values (ΔH_{seg}) and corresponding concentration (C) for La-Y Codoped surfaces and grain boundaries.

[§]Asymptotic ΔH_{seg} and C, *Value of ΔH_{seg} and C at a local minima; #neither asymptotic value nor minima is observed; ¥ change in the slope of the energy curve

	C_{surf} (at./nm ²)	$\Delta H_{seg,surf}$ (eV)	C_{gb} (at./nm ²)	$\Delta H_{seg,gb}$ (eV)
(00.1)	10.3720 [§]	-5.25 [§]	5.1860*	-3.84*
			10.372*	-4.07*
(01.2)	14.2453*	-4.15*	8.5472*	-2.9*
(10.0)	10.2291 [§]	-4.61 [§]	6.8194¥	-1.57¥
			10.2291¥	-2.34¥
(10.1)	9.7174 [§]	-2.14 [§]	6.4783*	-2.98*
			16.1957*	-3.44*
(11.0)	9.8429 [§]	-4.06 [§]	-	-
(11.1)	9.6703 [§]	-4.41 [§]	7.7362 [§]	-4.27 [§]
(11.2)	9.2022 [§]	-4.38 [§]	7.3618 [§]	-3.55 [§]
(11.3)	8.5535 [§]	-4.54 [§]	6.8428 [§]	-3.9 [§]
(22.3) [#]	6.6267 [§]	-4.23 [§]	6.6267 [§]	-3.16 [§]

Another important point to be noted is that the codoping segregation energies for different configurations with the same concentration have a much more continuous spectrum, no particularly lowest energy configurations are observed contrary to the single doping cases (Figure 3.3 and Figure 3.4). It will lead to an increase in the configurational entropy for segregation in case of codoping due to a higher number of comparable energy configurations.

3.4.1.2. Mg-La Codoping

Calculations were done for 5 surfaces and 4 grain boundaries for Mg-La and Mg-Y codoping. In case of codoping with Mg as one of the dopants, the concentrations which can be calculated are restricted due to the fact that one O vacancy has to be included for 2 Mg ions in the structure. Therefore concentrations are more discrete in comparison to Y-La case and hence it is difficult to comment on the pattern of the codoping segregation energy variation with dopant concentration in this case. Segregation energies for codoping are again negative for all the interfaces as shown in Table 3.3. Again, the Mg segregation energy calculated in the present work is 0.5-1.0 eV lower than reported in earlier work [80] due to the improved method to screen the lowest energy configurations. It may increase the solubility of the dopants

at the interfaces and hence the previously calculated [80] overall nominal solubility as well.

Figure 3.5 shows some representative segregation energy plots of Mg-La codoped surfaces and grain boundaries. Codoping segregation energy increases for all the Mg-La codoped grain boundaries except for (01.2), where it decreases with increasing dopant concentration (Figure 3.5 c). The segregation energy is always more negative for surfaces than GBs suggesting stronger segregation towards surfaces than GB's in this case as well.

Segregation is energetically more favorable for all the Mg-La codoped surfaces and grain boundaries except for (01.2) grain boundary in comparison to single doping, as codoping segregation energy plots lies below the average of the single doping segregation energy plots (Figure 3.5). It suggests that cosegregation of combination of dopants is preferred over the segregation of single dopants.

Table 3.3. Segregation energy values (ΔH_{seg}) and corresponding concentration (C_1 and C_2) for Mg-La Codoped surfaces and grain boundaries. C_1 and C_2 are the interface dopant concentrations when 4 and 8 dopant atoms are put on the interface respectively.

	C_1 (at./nm ²)	$\Delta H_{\text{seg,surf}}$ (eV)	$\Delta H_{\text{seg,GB}}$ (eV)	C_2 (at./nm ²)	$\Delta H_{\text{seg,surf}}$ (eV)	$\Delta H_{\text{seg,GB}}$ (eV)
(00.1)	5.186	-6.44	-4.65	10.372	-5.47	-4.14
(01.2)	5.6981	-4.33	-2.14	11.3962	-4.25	-2.69
(11.0)	7.8743	-4.49		11.8115	-4.25	
(11.1)	7.7362	-4.91	-4.52	11.6043	-4.49	-4.16
(11.3)	6.8428	-4.57	-4.63	10.2642	-4.69	-4.27

3.4.1.3. Mg-Y Codoping

Similar to other codoping combinations, the segregation energy for single as well as codoping is negative for all the interfaces. Again segregation towards surfaces for Y-Mg codoping is energetically more favorable than towards grain boundaries (Table 3.4). The segregation energy increases with increasing dopant concentration for all calculated surfaces and grain boundaries except for (01.2) GB, where it decreases with increasing concentration as shown in Figure 3.6 (c).

3. Dopant segregation in codoped [alpha]-alumina

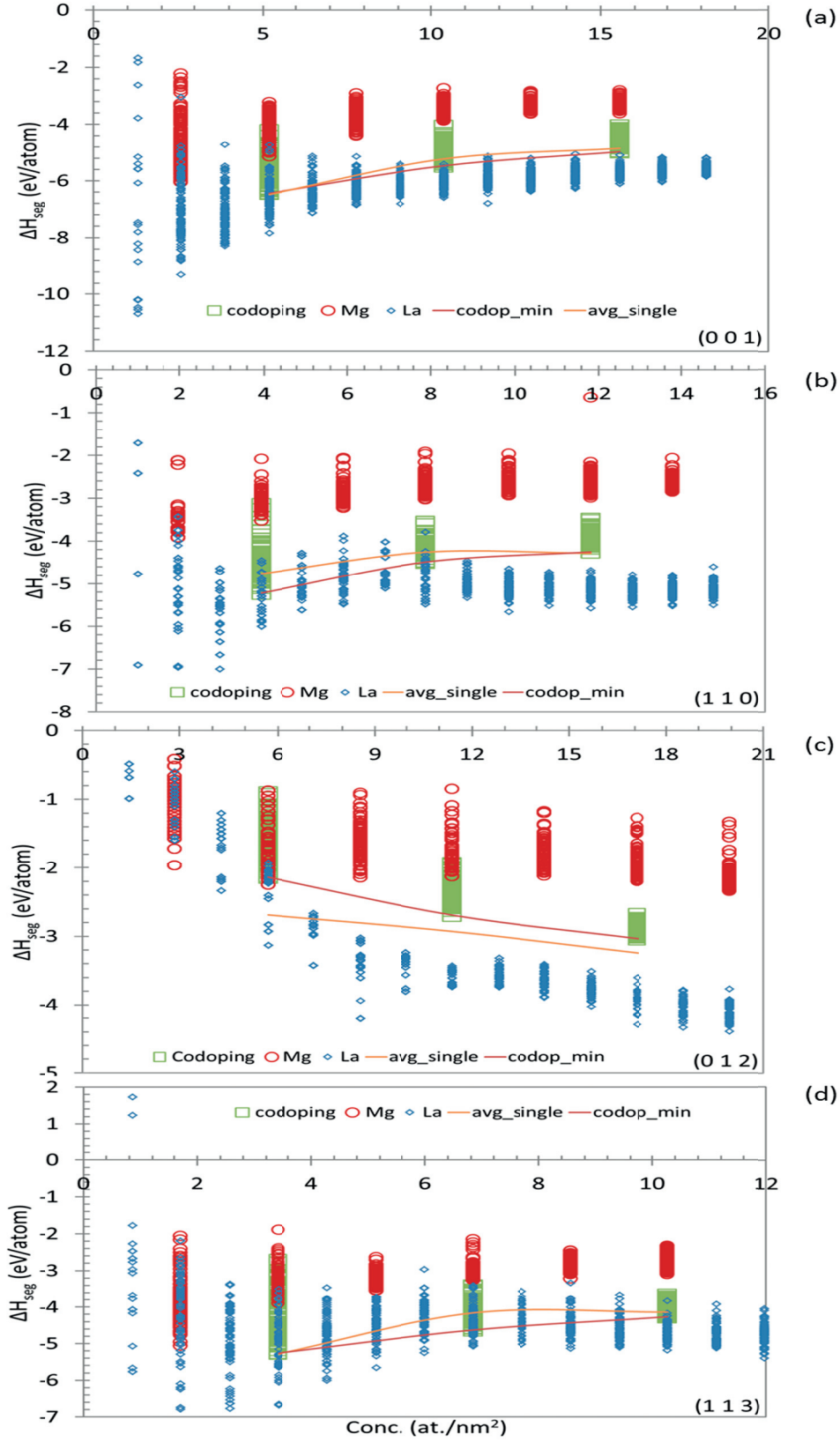


Figure 3.5. Representative segregation energy plots for Mg-La codoped a) (00.1) surface, b) (11.0) surface, c) (01.2) GB, d) (11.3) GB. Lines are just visual guides only.

Table 3.4. Segregation energy values (ΔH_{seg}) and corresponding concentration (C_1 and C_2) for Mg-Y Codoped surfaces and grain boundaries. C_1 and C_2 are the interface dopant concentrations when 4 and 8 dopant atoms are put on the interface respectively

	C_1 (at./nm ²)	$\Delta H_{\text{seg,surf}}$ (eV)	$\Delta H_{\text{seg,GB}}$ (eV)	C_2 (at./nm ²)	$\Delta H_{\text{seg,GB}}$ (eV)	$\Delta H_{\text{seg,GB}}$ (eV)
(00.1)	5.186	-5.04	-2.95	10.372	-4.14	-3.94
(01.2)	5.6981	-2.14	-2.84	11.3962	-2.69	-2.68
(11.0)	7.8743	-3.02				
(11.1)	7.7362	-3.4	-3.6	11.6043	-3.15	-3.18
(11.3)	6.8428	-3.06	-3.62	10.2642	-3.1	-3.2

Except (11.3) surface (Figure 3.6 b) and (01.2) grain boundary (Figure 3.6 c), segregation is energetically more favorable for calculated Mg-Y codoped surfaces and grain boundaries than single doping as shown in the Figure 3.6, and hence there is favorable interaction between Mg and Y dopants on the interfaces.

3.4.1.4. Cosegregation versus single dopant segregation energies

The segregation energies (Table 3.2, Table 3.3, Table 3.4) for the low energy grain boundaries (01.2) and (10.0) are less negative (La-Y: 1.57-2.9 eV; Mg-La: 2.69 eV; Mg-Y: 2.68 eV) than for the other grain boundaries (La-Y: 2.98-4.27 eV; Mg-La: 4.14-4.27 eV; Mg-Y: 3.18-3.94 eV). This might be supposed to lead to a homogenization of the sintered microstructure and a lower percentage of highly special low Σ twin boundaries. However even in undoped alumina the percentage of low energy Σ twin boundaries is very low [88] and a change in the homogeneity of the microstructure upon doping is not observed [56,88]. For surfaces the segregation energies of low and high energy surfaces are similar. The segregation energies for the (00.1) surface is significantly more negative than for the other surfaces in all the codoped cases (Table 3.2, Table 3.3, Table 3.4). Since the (00.1) surface is one of the lowest energy surfaces the highly negative segregation energies might be supposed to lead to a very low relative (00.1) surface energy and hence the domination of equilibrium morphology by the (00.1) surface (i.e. platelet like morphology).

3. Dopant segregation in codoped [alpha]-alumina

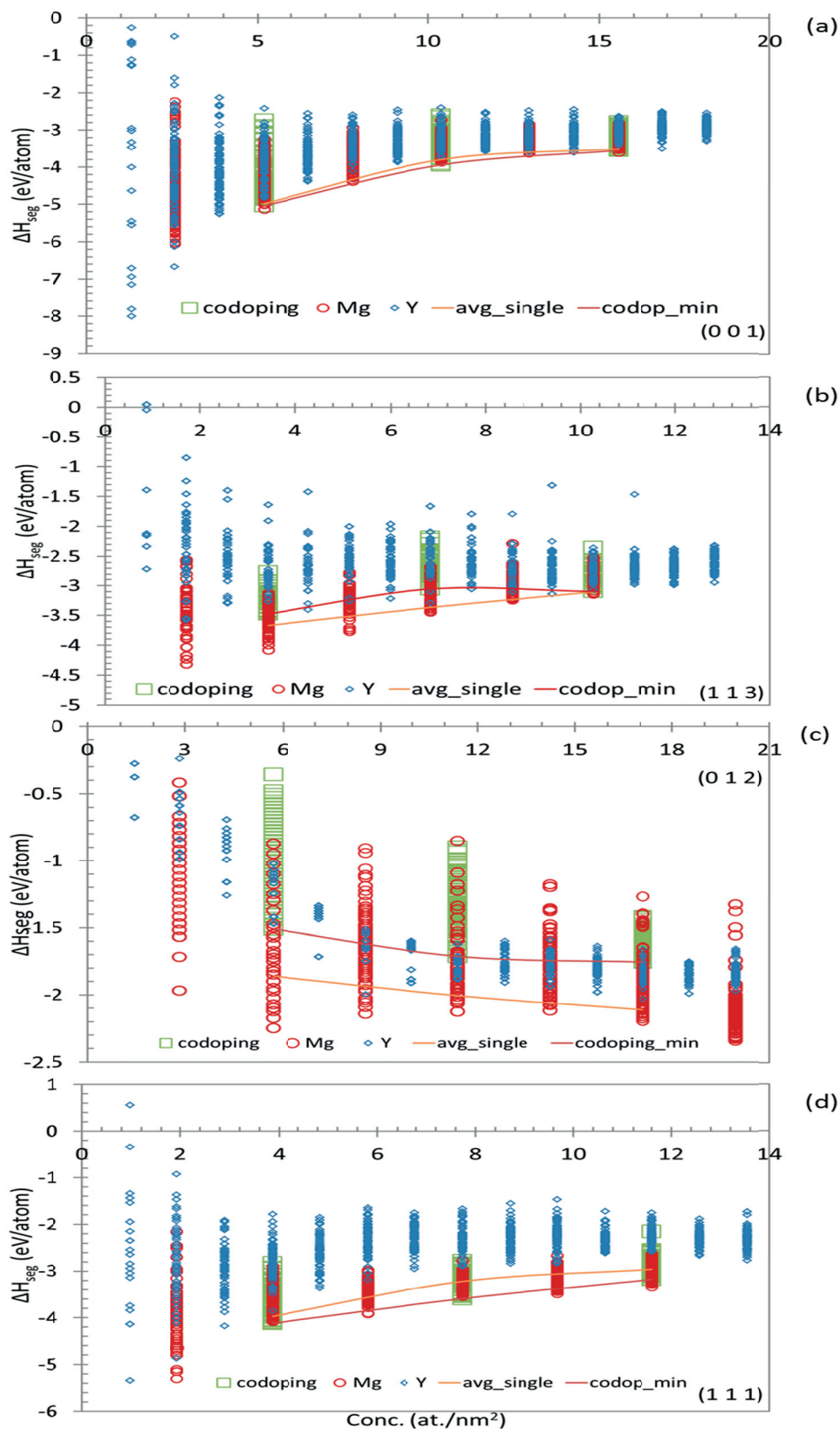


Figure 3.6. Representative segregation energy plots for Mg-Y codoped, (a) (00.1) surface, (b) (11.3) surface, (c) (01.2) GB, (d) (11.1) GB. Lines are just visual guides.

Segregation energy calculations show that while Mg-La and Mg-Y codoping combinations are energetically slightly more favorable in comparison to the single doping (Figure 3.5, Figure 3.6), La-Y codoping does not have any significant energetic gain over single doping (Figure 3.3, Figure 3.4). The current results are in agreement with the previous findings by Elsässer and Elsässer [70] DFT calculations, where they looked at the cosegregation of several dopant combinations in the single rhombohedral twin grain boundary in alumina. It was reported that while the cosegregation is favored over single dopant segregation in case of aliovalent (bivalent/trivalent) codoping, the cosegregation is slightly or not energetically favorable at all in case of identical isovalent dopants (Sc-Sc, Y-Y, La-La). The cosegregation of aliovalent dopants (Mg-Si) was reported to be energetically more favorable over single doping. Two factors are likely to contribute to the favorable Mg-Y and Mg-La cosegregation. The first factor is the creation of oxygen vacancies to compensate the charge of the Mg dopants on the Al sites. The presence of oxygen vacancies can be supposed to create more space for the accommodation of the significantly oversized Y and La ions. If the presence of oxygen vacancies is responsible for the energetic gain, sintering in vacuum should increase the amount of Y and/or La dopants at the interfaces similar to the addition of Mg because it increases the concentration of oxygen vacancies.

The second factor is the disparity in ionic sizes of the dopants (Mg^{2+} : 0.86 \AA , Y^{3+} : 1.04 \AA , La^{3+} : 1.17 \AA). Harmer et al. [75] showed in their atomistic simulation work that atomistic structures at the grain boundaries, especially high energy GB, breaks the unimodal void size distribution of the bulk alumina into multimodal distribution and hence creates several potential substitutional sites with varying sizes, many larger than the corresponding bulk sites. Therefore the dopants with different sizes should be able to fill up more voids with appropriate sizes. If this is the main reason for the energy gain, triple doping of Mg-La and Mg-Y doped alumina system with another dopant of medium size radius (e.g. Indium (0.94 \AA)) should also be energetically more favorable and help better packing the grain boundary atomic structure.

Comparison of the codoping segregation energies for different codopant combinations shows that the segregation energy is most negative for Mg-La dopant pairs (i.e. $\Delta H_{\text{seg}, \text{Mg-La}} \leq \Delta H_{\text{seg}, \text{Y-La}} < \Delta H_{\text{seg}, \text{Mg-Y}}$) for all the calculated surfaces and grain boundaries, as shown in Figure 3.7. The difference between Mg-La and Y-La segregation energy is not very marked, while the segregation energy for Mg-Y is significantly higher. This order is consistent with the order of segregation energies for single doped (i.e. $\Delta H_{\text{seg}, \text{La}} < \Delta H_{\text{seg}, \text{Mg}} \leq \Delta H_{\text{seg}, \text{Y}}$). The observed interaction energies as discussed in the previous sections do not alter the energetic order of the segregation energies. This is not surprising as in most cases the observed interaction energies between the different dopants were small.

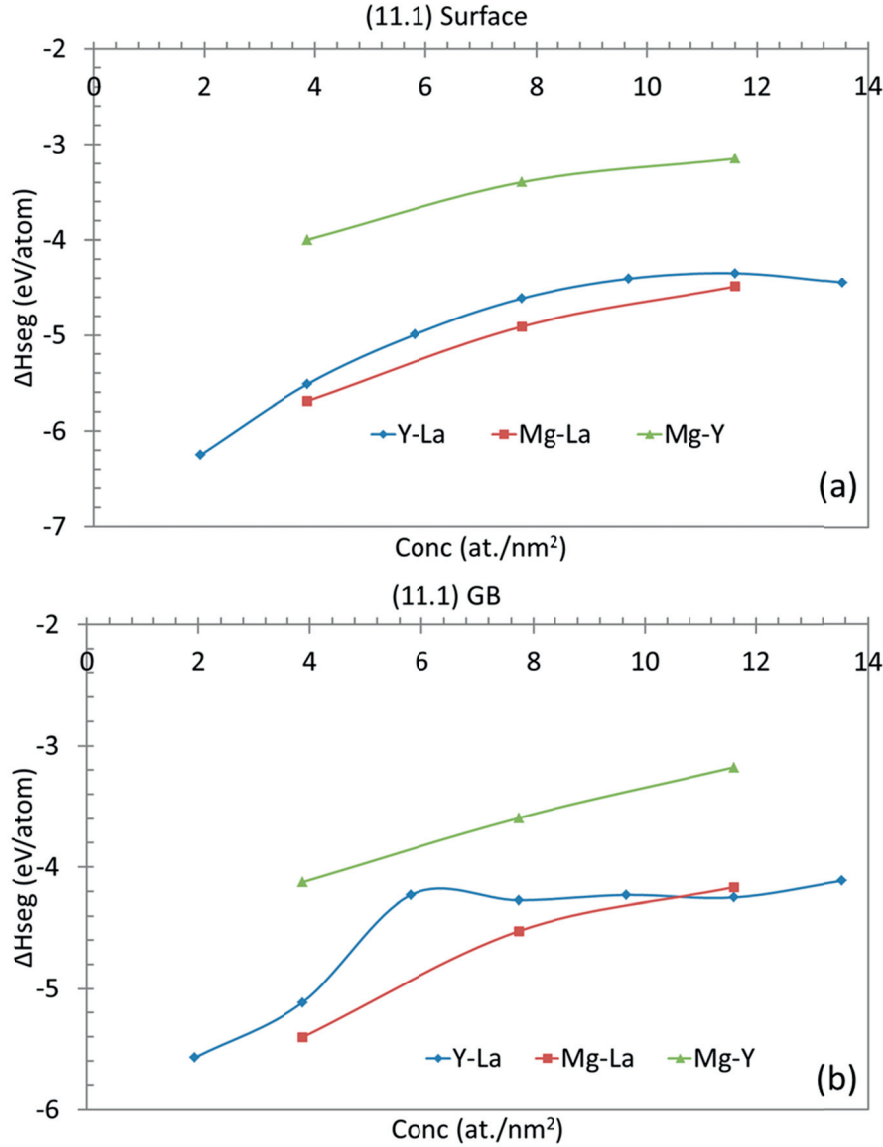


Figure 3.7. Codoping segregation energy comparison for three doping combinations for (a) (11.1) surface, and (b) (11.1) GB. The lines are visual guides only.

3.4.2. Interface specific segregation

Atomistic structures of the codoped surfaces and grain boundaries show that the dopants are confined to a very narrow region at the interfaces for all the dopant combinations and all the interfaces. West et al. [89] characterized the fine grained rare earth doped alumina ceramics using TEM based techniques (HRTEM, HAADF STEM and EDS) and reported the width of the segregation region to be less than 1 nm. Figure 3.8 and Figure 3.9 show the illustrative atomistic structures of Y-La codoped surfaces and grain boundaries at the characteristic interface dopant concentrations as mentioned in Table 3.2 in the previous section. Observation of the

atomistic structures suggests that segregation is sensitive to the surface and grain boundary structure. The segregation of the dopants affects the local grain boundary structure to some extent due to the relaxation of the oversized dopants, but the underlying structure of the grain boundary does not change significantly. The question of whether the dopant segregation is interface structure dependent or it is vice versa, was discussed in detail by Harmer et al. [78]. It was suggested by them that the boundary structure is determined by the dopant type and the concentration. However, the present study suggests that the final grain boundary structure in this concentration range of dopants is determined by the combination of both the factors: undoped local grain boundary structure as well as the dopant type and the concentration, in agreement with the earlier work in ref [66]. Variations across the different interfaces can be seen clearly in Figure 3.8 and Figure 3.9, for instance (01.2) and (11.3) surfaces as well as grain boundaries. While dopants form an ordered atomic layer at the (01.2) interfaces, they are randomly distributed at the (11.3) interfaces.

The dependence on the underlying interface structure can also be seen when looking at the packing efficiency. Dopants affect the packing efficiency of the surfaces and grain boundaries differently depending on the interface and the dopant combination. The same dopants may improve the atomic packing at some of the interfaces but create more spaces/voids on other interfaces. To confirm the effect of dopants on atomic arrangement of the interfaces, packing fractions were calculated for single doped and codoped grain boundaries. Packing fractions were determined by calculating the ratio of occupied volume of the grain boundary region (according to the ionic radii of the different ions) to the total volume of the considered grain boundary region. The average packing fraction was determined from all the calculated codoping configurations at different doping concentrations. The calculated packing fraction values (Table 3.5) show that the packing fractions vary quite significantly depending on the nature of the grain boundary as well as the doping combinations. Y doped grain boundaries are denser in comparison to La doped or La-Y codoped grain boundaries. Similarly, Mg doped grain boundaries have higher packing efficiency than La doped or Mg-La codoped grain boundaries. However in case of Mg-Y single/codoping, no conclusion can be drawn regarding effect of doping on grain boundary packing efficiency. It should be noted however that at least one of the doping combinations has the packing efficiency which is greater than the average of the single doping packing efficiencies regardless of the grain boundary. It leads to the conclusion that the triple doping would lead to enhanced grain boundary segregation in comparison to even codoping. Stuer et al. [56] also reported the best RIT and grain growth suppression results with triply (Mg-Y-La) doped alumina.

Table 3.5. Packing fractions of the single and codoped grain boundaries (Grain boundary width for packing fraction calculation was taken 10 Å⁰ for La-Y, La and Y doping, while 6 Å⁰ for Mg-Y, Mg-La and Mg doped grain boundaries).

	La	Y	Mg	La-Y	Mg-La	Mg-Y
(00.1)	0.59	0.64	0.65	0.63	0.63	0.69
(01.2)	0.59	0.62	0.58	0.62	0.56	0.58
(10.0)	0.53	0.61	-	0.57	-	-
(10.1)	0.53	0.61	-	0.57	-	-
(11.1)	0.55	0.58	0.57	0.56	0.58	0.59
(11.2)	0.57	0.60	-	0.58	-	-
(11.3)	0.58	0.62	0.64	0.60	0.59	0.63
(22.3)	0.61	0.61	-	0.61	-	-

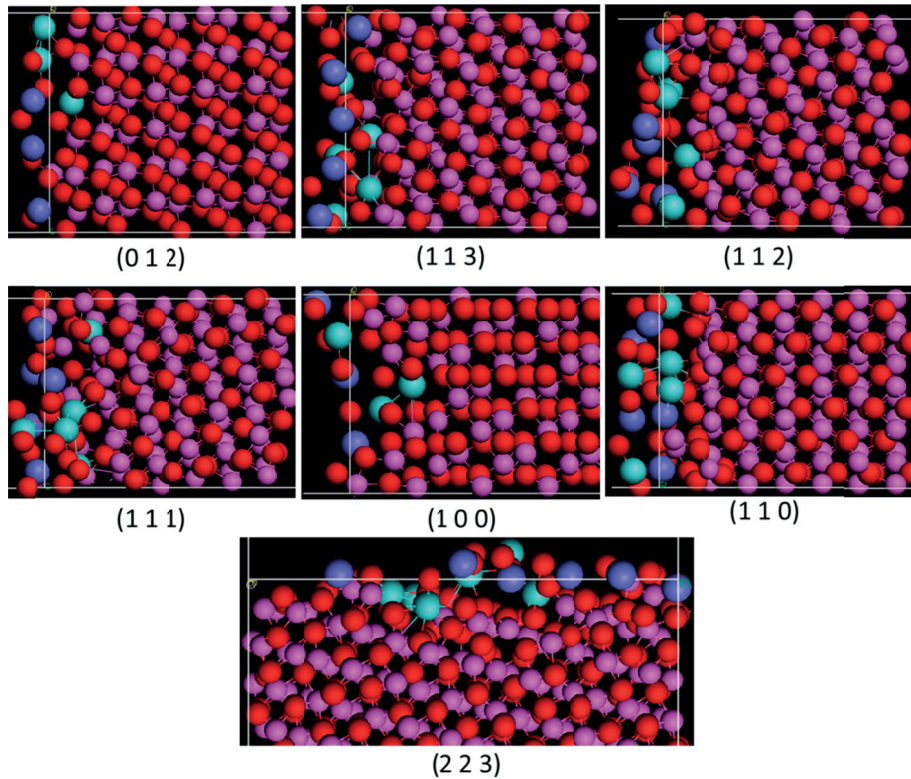


Figure 3.8. Interface structure dependent cosegregation and atomic arrangement of La-Y codoped α -alumina surfaces. All the atomistic structures are shown from the side view parallel to the grain boundary/surface plane with the white lines showing roughly the position of the grain boundary or surface plane. Oxygen ions are shown in red, aluminum ions in violet, Y in light blue and La in dark blue.

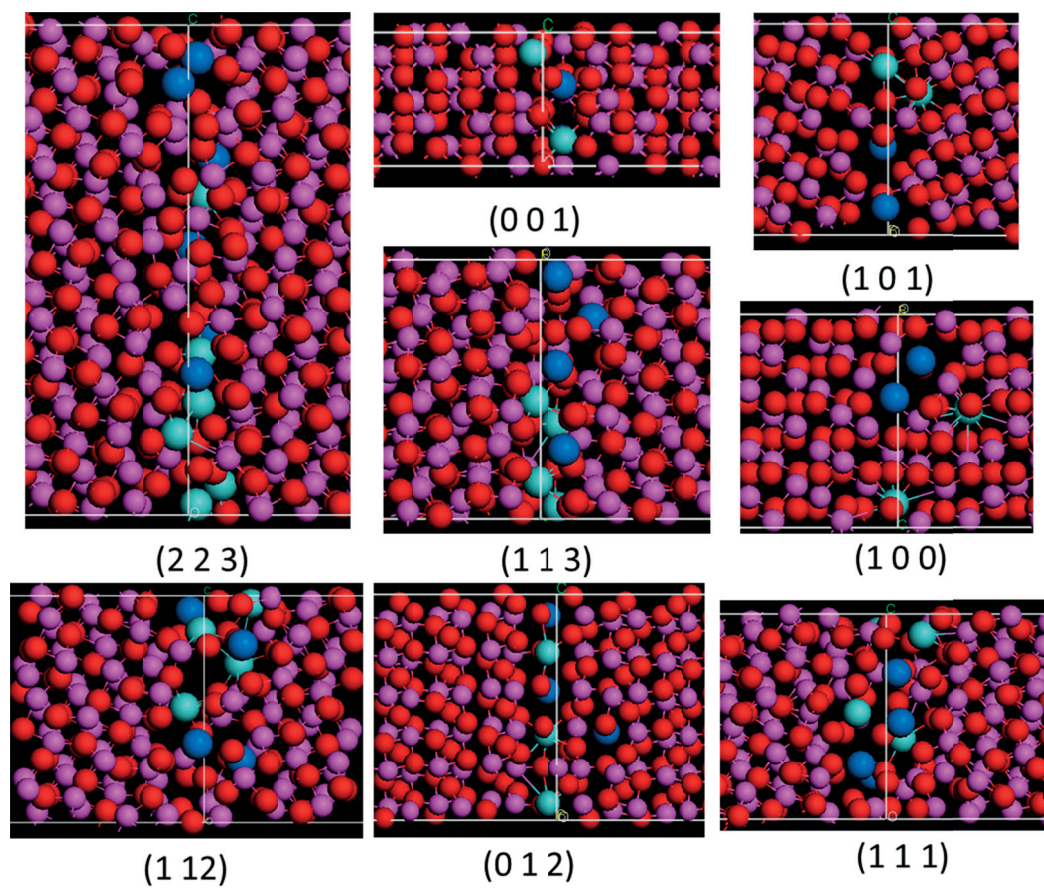


Figure 3.9. Interface structure dependent cosegregation and atomic arrangement of La-Y codoped α -alumina grain boundaries. All the atomistic structures are shown from the side view parallel to the grain boundary/surface plane with the white lines showing roughly the position of the grain boundary or surface plane. Oxygen ions are shown in red, aluminum ions in violet, Y in light blue and La in dark blue.

3.4.3. Complexion transition with dopant concentration

Concept of grain boundary complexion transition was introduced relatively recently by Harmer and coworkers [77] to explain the effect of dopants on grain boundary atomic structure. Complexions are phases which are not observed in the bulk phase but are stable at the grain boundaries under specific conditions. It has been proposed that based on the dopant type and concentration, the grain boundary complexion transitions take place and the mobility of the grain boundary is determined by the ordering of these complexions, which in turn will affect the sintering behavior of the ceramics. Figure 3.10 shows the development of the grain boundary complexion of a La-Y codoped (11.1) grain boundary with increasing dopant concentration, which is representative of other calculated grain boundaries. For low dopant concentrations (Figure 3.10 a,b), segregated dopants are adsorbed in

a monolayer. Shibata [91] et al. also observed well ordered two dimensional arrays of the Y-dopants at a high angle $\Sigma 13$ GB. For medium concentrations (Figure 3.10 c,d,e), segregated dopants form a bilayer. Above this concentration, the dopants are absorbed in a multilayer (Figure 3.10 f,g). Therefore, the increasing dopant concentration at the grain boundary leads to the higher order grain boundary complexions, which can be written as, $complexionI \Rightarrow complexionIII \Rightarrow complexionIV$, according to the terminology used in ref. [77]. It has been reported that when dopant segregation results into the formation of grain boundary complexion 1, it leads to the solute pinning effect and hence reduces the grain growth. For all other higher order complexions, grain boundary structure becomes more disordered and grain boundary mobility increases with increasing disorder [77,90]. Therefore, the dopant concentration has to be optimized in order to be effective in limiting the grain growth. Dopant concentrations higher than this will result into more disordered grain boundary complexions and hence will have an opposite effect on reducing the grain growth.

3.4.4. Oxygen vacancies at the grain boundaries

Doping of alumina with Mg is accompanied by the creation of oxygen vacancy defects in order to maintain the charge balance. One oxygen vacancy is created for every two Mg atoms. Figure 3.11 shows the probability plot of different oxygen vacancy sites on 4 different grain boundaries. The oxygen vacancy positions with lighter (or whiter) color and smaller size are the ones with higher probabilities. One of the most important features of these probability plots is that the highest probability vacancy sites are not necessarily in the center of the grain boundary region. For (11.1) and (01.2) GB's, the highest probably vacancy sites are located three atomic layers away from the center of the GB region. In case of (00.1) and (11.3) GB's, the high probability oxygen vacancy sites are more distributed across the GB region. There are few sites at the GB center which have the highest probability, but there are high probability sites away from the center also. Therefore, it can be concluded that there are high probability sites available away from the GB. Since the creation of the oxygen vacancy provides extra space to accommodate the larger size cations, the presence of higher probability oxygen vacancy sites will mean that the oversized dopants can be accommodated away from the GB also increasing the bulk solubility of the dopants. It provides an explanation to the earlier hypothesis based on the ab-initio study of Elasässer et al. [70] and the experimental observations of Song et al. [68], where they attributed the additional beneficial effect of codoping of alumina with Mg to its ability to redistribute the dopants in the bulk and increase the bulk solubility of dopants due to its charge compensation effect.

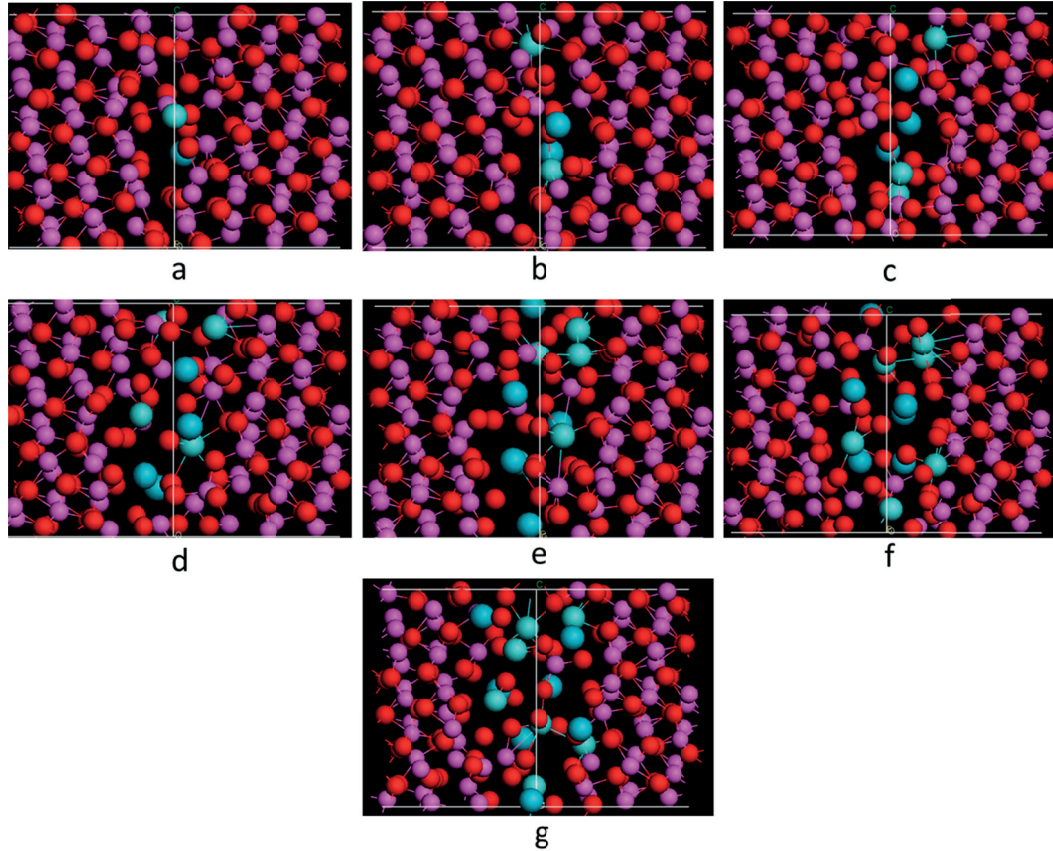


Figure 3.10. Complexion transition in La-Y codoped (11.1) grain boundary with the increasing dopant concentration. a) 1.93 at./nm², b) 3.86 at./nm², c) 5.79 at./nm², d) 7.72 at./nm², e) 9.65 at./nm², f) 11.58 at./nm², and g) 13.51 at./nm². La is dark blue and Y is light blue. All the grain boundaries are viewed parallel to the GB plane. Line at the grain boundary is only a rough estimate of the grain boundary position.

3.4.5. Atomistic structure characteristics: Codoping vs. single doping

There is no specific pattern formation by the dopants at the codoped grain boundaries, with the exception of the (01.2) grain boundary where a pattern is observed for all three codoping combinations. As shown in Figure 3.12 dopants occupy positions which form an atomic layer parallel to the grain boundary. Dopants first exhaust the interface Al sites available before going to the next sub-surface layers leaving on original alumina atomic layer intact in between. The absence of pattern formation for the majority of interfaces studied is in contrast to the formation of geometric patterns by Y in many of the single doped alumina surfaces and grain boundaries at minimum energy concentrations, observed in earlier simulation studies [79] as well as experimental studies using TEM [91]. This is also consistent with the fact that in general upon codoping no minimal energy

configuration is observed, the energies calculated for the different configurations for a specific dopant concentration seem to form a continuous energy spectrum, indicating a higher configurational entropy in the case of codoped than in the case of single doped interfaces.

In general codoping is observed to produce more ordered and rigid atomistic structures at the interfaces. This effect is most pronounced when La doped structures are compared to Mg-La and Y-La codoped structures, due to its higher size mismatch. E.g. as shown in Figure 3.13, in comparison to La-doped (11.1) grain boundary (Figure 3.13 b), Mg-La and Y-La codoped grain boundaries (Figure 3.13 d, f) have more ordered and rigid structure. The effect is also visible for Mg and Y dopants, but to a lesser extent.

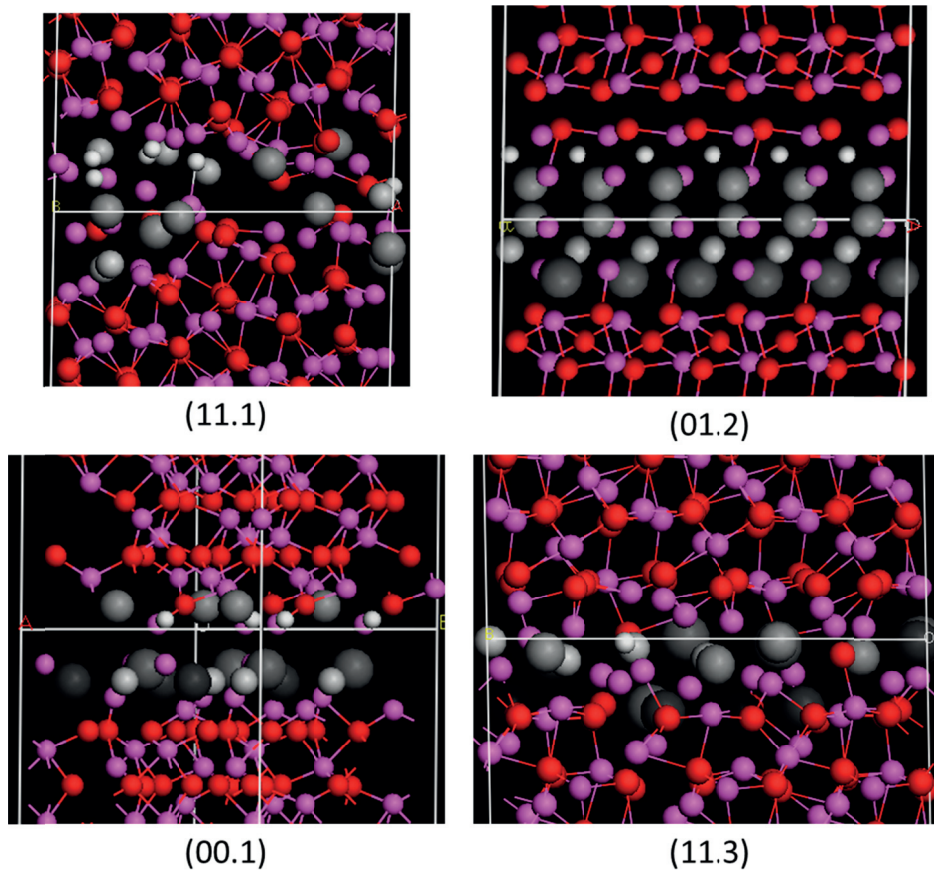


Figure 3.11. Energetic probabilities of oxygen vacancy formation at the grain boundaries. The sites with smaller and lighter color atoms have higher probability and darkest and largest one have the least possibility. All the grain boundaries are viewed parallel to the GB plane.

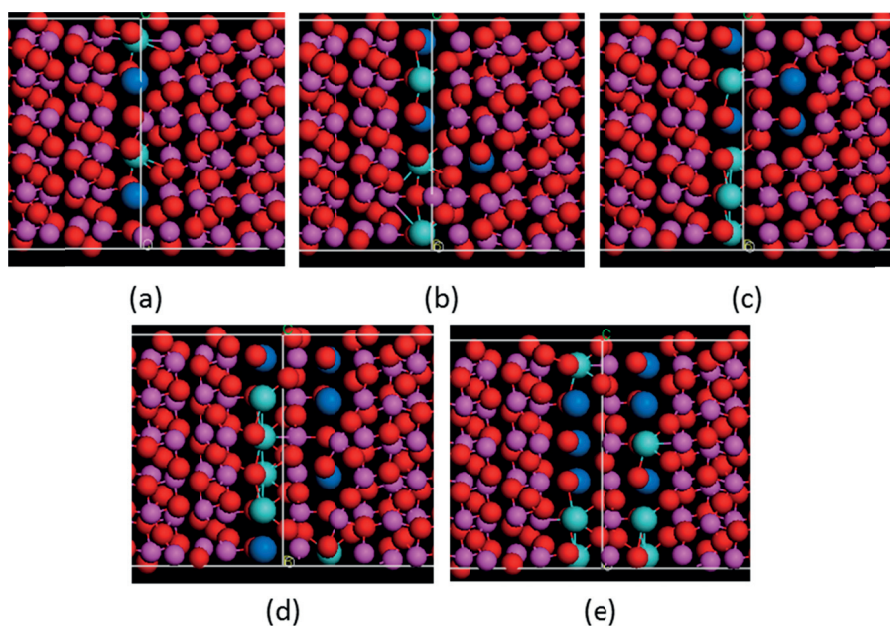


Figure 3.12. Formation of dopant atomic layer on Y-La codoped (01.2) grain boundary with increasing dopant concentration. Oxygen ions are shown in red, aluminum ions in violet, Y in light blue and La in dark blue.

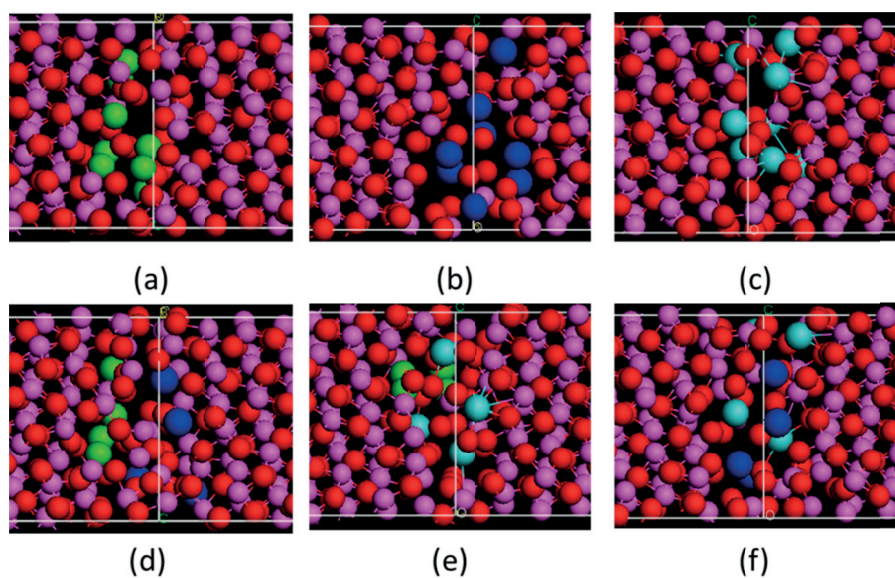


Figure 3.13. Comparison of single doped and codoped (11.1) grain boundaries (a) Mg doped, (b) La doped, (c) Y- doped, (d) Mg-La codoped, (e) Mg-Y codoped, and (f) La-Y codoped (Concentration=7.74 at./nm²). Oxygen ions are shown in red, aluminum ions in violet, Y in light blue, La in dark blue and Mg in green.

3.4.6. Coupling Effect

As mentioned in the previous section, there is no energetic gain for cosegregation over single dopant segregation in case of Y-La codoped surfaces and grain boundaries. However, an atomistically preferred arrangement of the dopants is observed in the case of Y-La codoping. As shown in Figure 3.14, dopants of different species arrange themselves around the oxygen at nearest neighbor positions. An oxygen ion seems to be more often coordinated by a Y and a La than by two La or two Y. To confirm the atomistic observations coordination numbers (CN) were determined for different surfaces and grain boundaries from the atomistic structures of the interfaces at characteristic concentrations for each interface as mentioned in Table 3.2. Coordination number for Y-La was found to be higher in comparison to Y-Y and La-La coordination numbers for all the surfaces and grain boundaries, except the (10.1) and (11.1) grain boundaries. CN's for both Y-Y (2.39) and La-La (3.55) are higher than Y-La (2.17) for (10.1) grain boundary. Similarly, for (11.1) grain boundary La-La CN (2.39) is higher than Y-La CN (2.09). For other grain boundaries, the coordination number for Y-La varies from 1.53 to 2.22, while for Y-Y and La-La it varies from 0.51-1.64 and 0.83-1.43 respectively. Similarly the coordination number of Y-La, Y-Y and La-La varies from 1.81-3.01, 1.39-2.2 and 0.98-1.94 respectively for codoped surfaces. Higher coordination number for Y-La in comparison to Y-Y and La-La for each individual interface shows the higher probability of Y and La at nearest neighbor position around oxygen. In an ab-initio study, Elsässer and Elsässer [70] also observed a similar specific atomic arrangement of dopants on rhombohedral twin boundary of alumina when codoped with bivalent/trivalent dopant ions. They reported that in case of codoping, dopant pairs prefer to arrange on nearest neighbor sites parallel to rhombohedral plane, showing a coupling effect. This is supported by the above results for other grain boundaries in the alumina system.

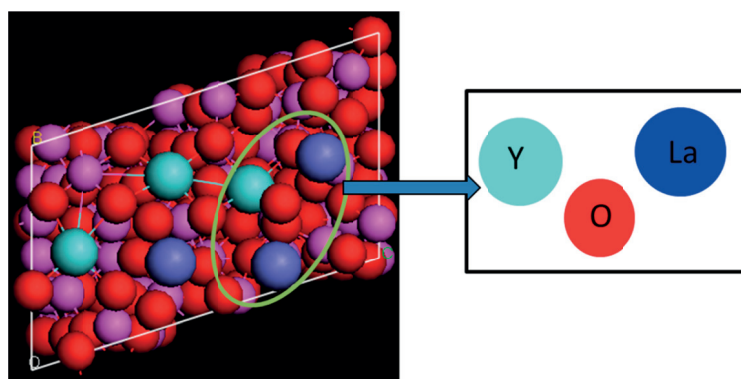


Figure 3.14. (11.1) Y-La codoped surface looked from the top perpendicular to the surface. Specific coordinative arrangement/coupling effect is seen, where oxygen atom is always surrounded by two different types of dopant ions.

Table 3.6. Dopant-Oxygen coordination number (CN) and nearest neighbor (NN) distance for different codoping combinations

Doping combination	La-O		Mg-O		Y-O	
	CN	NN (Å°)	CN	NN (Å°)	CN	NN (Å°)
La-Y surfaces	5.12-5.84	2.39-2.47	-	-	5.62-5.87	2.24-2.33
La-Y GB's	6.56-9.39	2.49-2.55	-	-	6.24-7.86	2.28-2.41
La-Mg surfaces	5.37-5.80	2.42-2.49	4.40-5.58	2.03-2.11	-	-
La-Mg GB's	7.49-7.80	2.49-2.53	5.12-5.97	2.11-2.14	-	-
Mg-Y surfaces	-	-	4.20-5.49	2.00-2.12	4.90-5.70	2.19-2.31
Mg-Y GB's	-	-	5.44-5.74	2.03-2.11	6.17-7.34	2.25-2.34
Single doped surfaces[79,80]	3.8-6.0	2.33-2.43	-	-	3.00-5.82	2.00-2.37
Single doped GB's [79,80]	5.5-6.5	2.36-2.45	5.00-5.50	2.09-2.12	6.51-7.49	2.30-2.40

3.4.7. Dopant Oxygen Coordination Number

The dopant-Oxygen coordination numbers (CN) have been calculated for all the codoping cases. The characteristic concentrations to calculate dopant-O coordination number for La-Y codoping were taken from Table 3.2. For Mg-Y and Mg-La codoping the concentration corresponding to 8 dopant ions was considered to calculate the dopant-O CN. In accordance with the different geometry (i.e. at the surface neighbors normally found in the bulk are missing whereas at grain boundaries only their relative positions will change), coordination numbers are higher for grain boundaries than for surfaces. The dopant-oxygen coordination numbers do not vary much from one codoping combination to another (Table 3.6).

No significant change in Y-O and Mg-O coordination environment between single doped and codoped structures is observed. The coordination numbers as well as the nearest neighbor distance are similar in single doped and codoped alumina for Mg and Y. However, the Y-O coordination number seems to be more homogeneous in codoped alumina than single doped alumina across different surfaces. For La-O on the other hand, the coordination numbers are significantly higher in codoped alumina in comparison to single doped alumina. The CN of La-O and Y-O is also significantly higher than the Mg-O coordination. Due to the better chemical accommodation of the trivalent dopants in comparison to bivalent dopants [70], it results into stronger dopant-oxygen coordination bonds at the grain boundaries. Stronger coordinate bonds between oxygen and trivalent dopants and further enhancement of bonding due to codoping (Mg-La) leads to rigid atomistic structures, which strengthen the grain boundary against creep as also reported by Buban et al. [63].

3.5. Conclusions and Outlook

Atomistic arrangements and segregation energies have been investigated using empirical potential based energy minimization technique for 9 different surfaces and 8 grain boundaries for La-Y codoping in alpha alumina. A lower number of surfaces and grain boundaries were investigated for the Mg-La and Mg-Y cases due to the higher computational cost caused by the need to introduce oxygen vacancies to compensate for the difference in valence of Mg with the host cation Al. Energy of segregation is negative for all the interfaces and for all the single doping and codoping combinations, which suggests that segregation of dopants is energetically favorable for all larger size dopant cations. Cosegregation does not have significant gain energetically over single doping in case of codoping of alumina with isovalent dopants (Y-La). However, Y-Y, La-La and Y-La coordination numbers in combination with atomistic structure of doped interfaces show a preferred atomic arrangement of the dopant atoms (coupling effect) at the Y-La codoped interfaces, whereby different type of dopants prefer to arrange themselves around oxygen on the nearest neighbor positions. This is an agreement with earlier ab-initio simulations done on only a single grain boundary [70]. Segregation energy is more negative for aliovalent codoping (Mg-La and Mg-Y) in comparison to single doping for most of the surfaces and grain boundaries, which may be attributed to two possible factors: grain boundary space created due to oxygen vacancies and disparity in the ionic sizes of the dopants. This observation leads to an interesting possibility of doping alumina with three different sized cations, e.g. Mg-La-In, to further enhance the additional effects of codoping in alumina. Comparison of packing efficiency of single doped and codoped grain boundaries also suggests that the doping of alumina with more than two different sized cations may be more efficient in enhanced packing of the grain

boundaries. Once again the findings of the current study are in good agreement with the conclusions of ref. [75], which were drawn from a study done on only two simple grain boundaries $\Sigma 3$ and $\Sigma 13$.

The final grain boundary structure in the studied concentration range of dopants is determined by the combination of two factors: the undoped local grain boundary structure as well as the dopant type and the concentration. Although dopants affect the local grain boundary structure, the underlying atomic arrangement of the grain boundaries does not change significantly due to the segregation in the probed dopant concentration range. Investigation of the grain boundary complexion transition with dopant concentration suggests that there has to be an optimum dopant concentration for favorable complexion transition to reduce the grain boundary mobility and hence reduce the grain growth.

In case of codoping with Mg, due to the presence of the more favorable oxygen vacancy defect formation sites away from the center of the grain boundary region, more space becomes available away from the grain boundary center to accommodate the larger size dopants. It helps redistributing the dopants farther from the grain boundaries and hence, increasing the nominal solubility of the dopants.

Dopant-oxygen coordination numbers were higher for trivalent dopants (Y and La) in comparison to Mg and for codoping (La-Mg) in comparison to single doping (La). Stronger covalent bonds between oxygen and trivalent dopants, and further enhancement of covalent bonds due to the codoping (Mg-La), lead to rigid atomistic structures, which strengthens the grain boundaries against creep.

The present study contributes in extending the understanding of doping in general, and especially codoping in the processing of alumina. It confirms the previous findings of specific coupling [70] and cation size disparity [75] which were done on very limited grain boundaries, for wider variety of grain boundaries. In addition it has been able to attribute the relative importance of bivalent and trivalent dopants to different reasons. While trivalent dopants can be chemically more suitable in alumina and may have coupling effects, codoping with bivalent dopants is energetically more favorable and helps increase the nominal solubility of dopants by creating favorable oxygen vacancies away from the center of the grain boundaries. Extending the complexion study of Harmer et al., it was shown that to obtain the favorable complexion of the grain boundaries by doping, the doping concentrations have to be optimized, which was observed ~ 4 atoms/nm² in the present study.

The triple doping with varying size dopants, e.g. Mg-In-La or Mg-In-Y would be an interesting proposition to look into in the future experimentally as well as by atomistic modeling. However screening the most favorable doping configuration will

be more difficult due to the increased number of possible configurations and hence, will need more computational resources. Another possibility for the modeling will be to try out the different compositions of the dopants. In the present study only equal proportions of the dopants were simulated. It would be interesting to see how the energetics and atomistic structure change with different concentrations of the dopants. Although variety of grain boundaries, low as well as high energy grain boundaries were simulated in the present work, the real sintered alumina microstructure has very little fraction of such twin grain boundaries. Therefore, it's very difficult to make a good comparison with the experiments, which is a serious limitation. More general grain boundaries need to be simulated in order to validate the modeling results with the experiments. The current thesis makes some effort in that direction, the results of which will be discussed in chapter 6.

4. Segregation of Anion Impurities

In the following chapter the results of the study on segregation of chlorine impurity on the alumina interfaces will be presented and discussed. First a brief introduction and literature survey of this relatively little studied phenomenon relevant to the processing of alumina will be provided. Then the simulation approach along with the derivation of the potential parameters will be discussed. Finally, the results will consist of segregation energies of the anion impurities, effect of anion impurities on the atomistic structure, coordination number etc.

4.1. Introduction

α -alumina powder has been used as a raw material for polishing abrasives, catalyst supports for high temperature reactions, cutting tools, and advanced ceramics. Powders of α -alumina are synthesized using several established methods, such as the Bayer process, calcination of gel based $\text{Al}(\text{OH})_3$ in air or in controlled atmosphere, high temperature decomposition of aluminum-containing salts, and chemical vapor decomposition. Out of these methods, vapor decomposition method is employed very commonly to produce nano size α -alumina powders. Synthesis of high purity alumina powders is crucial for the processing of advanced ceramic applications, e.g. transparent alumina [92,93]. Even a small amount of impurity could be detrimental for the performance of such advanced ceramics. There are several commercial α -alumina nano powders available in the markets, which claim to be 99.99% pure, e.g. Baikowski, Sumitomo. However, there are still very small amount of impurities present due to the contamination during the vapor phase synthesis. Baikowski and Sumitomo, two commercially available nano powders, both report a total cation impurity (Na, Si, Fe, Ca etc.) content of ~ 50 ppm in their powders. However, none of the producers report any anion impurity content. In the literature also, there has been rarely any analysis done for the contents of anion impurities in

alumina powders. Heuer et al. [94] reported 140 ppm anion impurity content in Lucalox alumina powders. Except that, to the best of my knowledge there have not been any attempts to quantitatively characterize the anion impurities in alumina. However depending upon the synthesis method, alumina can contain Cl^- ions or $(\text{SO}_4)^{2-}$ impurities, which is accepted by majority of the people working in the field.

There are numerous studies available in the literature which focus on the effects of cation dopants/impurities on the properties of alumina, e.g. sintering, grain growth, light transmission, creep resistance, details of which were discussed in chapter 3. However, the effects of anion impurities are very poorly understood, not only in the field of alumina, but also in the processing of other ceramic materials, like TiO_2 , MgO , spinel etc. The very limited numbers of studies which are available throw some light on the importance of anion impurities in the processing of the ceramics. Fan et al. [95] reported that $\text{C}_2\text{O}_4^{2-}$ impurities in porous alumina membranes accumulated during the electrochemical anodization process in oxalic acid solution can affect its refractive index and adsorption coefficient.

Leipold and Kapadia [96] studied the effect of anion impurities (S^{2-} , Cl^- , F^- , OH^-) on hot-pressing of MgO . It was reported that the final density of MgO is reduced due to the presence of all the anion impurities in the temperature range of 850-1150 °C. The vapor pressure and second phase precipitate formation at the interfaces were proposed to be the contributing factors behind the effects of anion impurities. However, no supporting evidence was reported for second phase precipitate formation.

Dittmann et al. [97] also investigated the effect of Cl^- impurities on the sintering behavior of titania nano particles. It was reported that although Cl^- impurities lowered the temperature of phase transition and densification, it resulted in a drastic grain growth during the final stage of sintering. Grain boundary embrittlement was also observed in the samples containing Cl^- impurities. It was proposed that the Cl^- anions get entrapped in the ceramic pore structure due to the early densification of titania nano powders. These pores cannot be closed due to the evaporation and condensation kinetics of grain growth in presence of Cl^- impurities.

In the light of earlier observations of effect of Cl on oxide materials sintering and densification, it can be an important topic to investigate in order to enhance our understanding of sintering of alumina polycrystals. In the present atomistic modeling work, the segregation energies of Cl^- ions on the alumina surfaces and grain boundaries were calculated. The coordination numbers of Cl^- ions on the interface were calculated in order to get an idea of the chemical environment of the ions on the interfaces. The analysis of the segregated interface atomic structures should give insights into the effect of Cl^- ions on the microstructure of Cl contaminated alumina. Being a very little explored area of study, this preliminary work should help

understanding the importance of anion impurities in the processing of advanced alumina ceramics.

4.2. Approach

The details of the segregation calculations have already been given in the previous chapter. Only the modifications in the previously explained method will be given here. The energies of the doped and undoped surfaces and grain boundaries were calculated using the Born model for solids. Born model describes the interatomic forces in terms of pair potentials. In this case, the pair potential parameters were taken from the work of Binks et al. Binks potential parameters were fitted to chlorides, oxides and fluorides of various metals (Li, Na, K, Al, Zn, Ag, Co etc.), including Al_2O_3 . However, the Buckingham potential parameters were not derived for Al-Cl interaction in that work. Therefore, Al-Cl Buckingham potential parameters were calculated in the present work by fitting it to the aluminum oxy chloride (AlOCl) lattice parameters, keeping all other parameters constant as given in the Binks potential set. The fitted lattice parameters as well as the experimental parameters are given in the Table 4.1.

Table 4.1. Results of the Al-Cl Buckingham potential parameter optimization. The experimental and the fitted lattice parameter along with the error are listed in the table.

	a	b	c	α	β	γ
Fitted	3.43	3.81	8.58	90.0	90.0	90.0
Experimental	3.62	3.61	7.67	90.0	90.0	90.0
Error (%)	-5.2	5.5	11.9	0	0	0

The screening method to avoid the large number of possible configuration and select only highest probable configurations was similar as described earlier in the case of cation segregation. Probability of each substitutional anion site was calculated first. The depth of the scanning region to calculate the probability sites varied 2-4 Å for surfaces and 4-8 Å for grain boundaries depending on the number of sites available in this region. To maintain the charge balance of the system one Al vacancy was created for every three Cl atoms. Cl substitutional defects (O_{Cl}) and the Al (V_{Al}) vacancies were assumed to be decoupled and therefore were treated independently instead of a cluster $[\text{V}_{\text{Al}}3\text{O}_{\text{Cl}}]$. In the expression for segregation energy also, the energies of the substitutional Cl and Al vacancies are subtracted separately (Eq.4.1). Similar to the case of Mg doping, the interfaces were divided into slabs of (0.5-1 Å) to reduce the number of possible Al vacancies for each Cl substitution. The

probability of each O_{Cl} site was calculated similar to the case of Mg doping. The lowest energy O_{Cl} and V_{Al} were permuted in order to get the lowest energy configurations of multiple Cl segregated alumina interfaces. The segregation energy of a configuration was calculated using the expression:

$$\Delta H_{seg}(N_{Cl}) = \frac{1}{N_{Cl}} \left(H(N_{Cl}) - H(0) - N_{Cl} \Delta H_{Cl,bulk} - \frac{N_{Cl}}{3} \Delta H_{V_{Al},bulk} \right) \quad \text{Eq.4.1}$$

Where, $\Delta H_{seg}(N)$ is the segregation energy in the structure containing N Cl atoms. $H(N)$ is the potential energy of the structure containing N Cl atoms. $\Delta H_{i,bulk}$ is the change in enthalpy when inserting ion i or V_{Al} in the bulk, which was calculated by the Mott Littleton method with 4 Å and 10 Å as the radius of region 1 and 2 respectively. In total 3 surfaces and 5 grain boundaries were calculated, which are listed in Table 4.2. 150 configurations were calculated for each anion concentration. The interface energy and area of the grain boundaries and surfaces calculated in the present work were given in the table 1 of chapter 3.

Cl-Al coordination numbers and the near neighbor distances in the segregated interfaces were calculated to characterize the change in the atomic arrangement due to the presence of Cl impurities. The average distance of first nearest neighbor and second neighbor was used as the cut off (4.25 Å) for these calculations.

4.3. Results and Discussion

4.3.1. Experimental evidence of Cl at GB's

A collaborative work was carried out at the Centre for Electron Microscopy (CIME) at EPFL by F. Nabiei [98] and coworkers to characterize the sintered transparent polycrystalline alumina samples prepared in our group using Sumitomo (AA04) powders. Scanning Transmission Electron Microscopy (STEM) Imaging and Energy Dispersive X-Ray (EDX) spectroscopy techniques were used to show that the significant amount of Cl anion impurities were present in the grain boundaries and especially at the triple points (Figure 4.1). The line scan analysis to determine the amount of impurities showed varying amount of Cl anions across the different grain boundaries ranging from 0.2 – 7.7 atoms/nm². However, Cl peaks were observed even 0.2 µm away from the center of the grain boundary in the line scanning results.

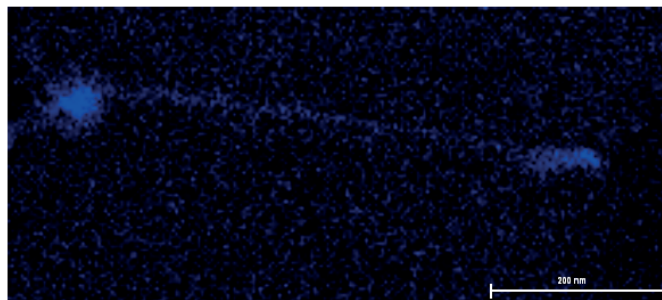


Figure 4.1. STEM-EDX spectroscopy results showing the presence of Cl impurities at a grain boundary and the triple points.

4.3.2. Segregation energies (ΔH_{seg})

Figure 4.2 and Figure 4.3 show the representative ΔH_{seg} versus anion concentration plots for the Cl segregated surfaces and grain boundaries respectively. ΔH_{seg} for all the surfaces and GB's was found to be negative at all the calculated concentrations in the present work, which suggests that the Cl anion segregation is energetically favorable. ΔH_{seg} is slightly more negative for surfaces than GB's, which shows the higher tendency of segregation of anions to the surfaces. It might be attributed to the fact that it is easier to accommodate oversized anions on the surfaces than GB's due to partially coordinated atoms at the interface.

ΔH_{seg} for Cl anions is 4-6 times more negative than the cation ΔH_{seg} , which is comprehensible given the much larger ionic size of Cl anions (1.7 Å) in comparison to La (1.17 Å) or Y (1.04 Å). Due to such a large size mismatch, the bulk solubility of Cl is expected to be very low in alumina and it is expected to strongly segregate to the interfaces. Such a strong segregation may result into a 'swamp out' effect, which is sometimes used to explain the reduced segregation of Mg in presence of Y [99]. It is essentially the inhibition of segregation of one cation dopants due to the preferential segregation of other dopant. In this case very strong segregation of Cl anions may inhibit the segregation of other cation dopants to the GB's.

ΔH_{seg} continuously becomes more positive with the increasing anion concentration, which is similar to the majority of the cation doped interfaces (chapter 3). However, one of the characteristics observed in the ΔH_{seg} versus concentration plots for Cl anions is the change in slope of the curve at a certain concentration. The slope of the curve is higher at lower concentration and it decreases after a certain point. Table 4.2 gives the value of the characteristic concentration and minimum segregation energy at this concentration. The characteristic concentration varies significantly across the different interfaces, but it remains constant for the same index surface and grain boundary. However, the exact characteristic concentration might be missed sometimes between the two calculated concentrations due to the large

interval between them, which is different for each interface because of their different surface area. Interfacial atomic structures corresponding to this concentration will be discussed in the next section.

Table 4.2. Chlorine segregation energies are listed for alumina surfaces and grain boundaries at the concentration where the slope changes in the segregation energy plot. Corresponding characteristic concentrations are also given for each interface.

Miller Index	Sigma (Σ)	Conc. (at./nm ²)	$\Delta H_{seg,surf}$ (eV)	$\Delta H_{seg,gb}$ (eV)
(00.1)	3	7.5	--	-12.3
(01.2)	7	8.2	-13.2	-12.2
(10.0)	3	9.8	-13.3	-10.9
(10.1)	11	9.3	--	-11.6
(11.1)	93	5.6	-15.2	-12.1

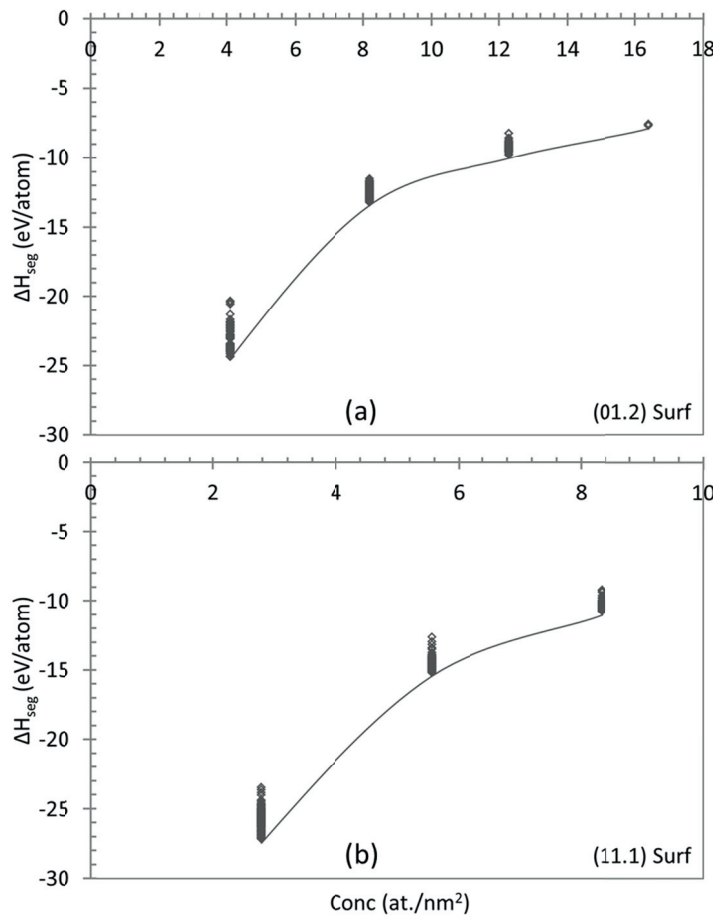


Figure 4.2. Representative segregation energy plots for Cl segregated (a) (01.2) surface, and (b) (11.1) surface. Lines are just visual guides.

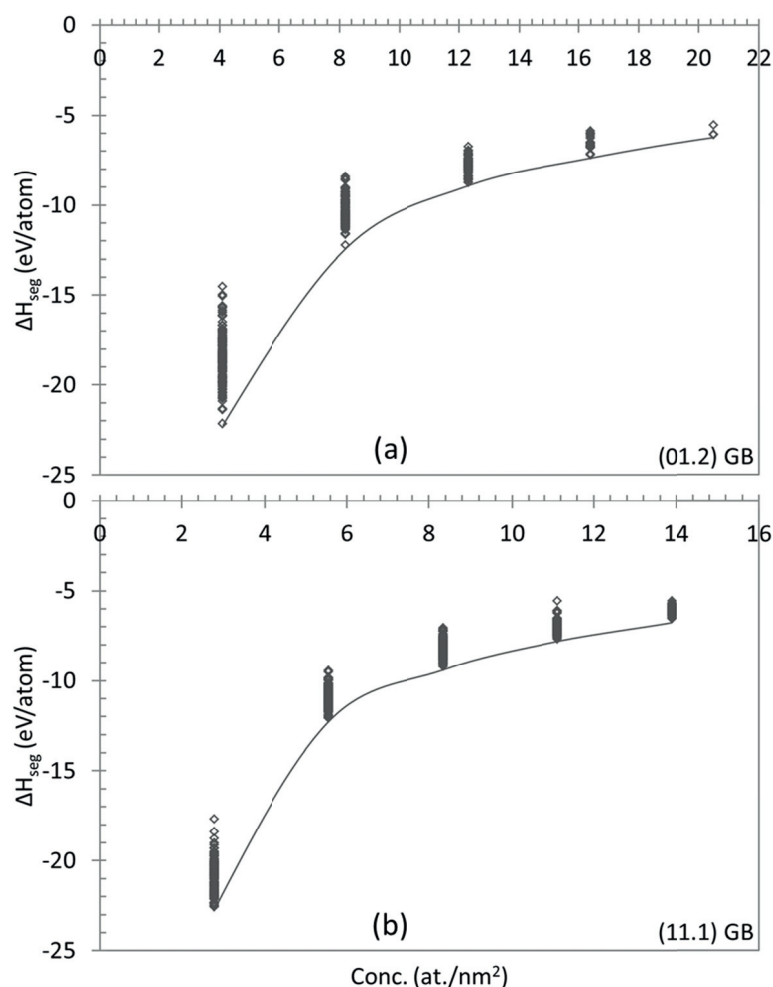


Figure 4.3. Representative segregation energy plots for Cl segregated (a) (01.2) GB, and (b) (11.1) GB. Lines are just visual guides.

4.3.3. Interface atomistic structures

Figure 4.4 shows the atomistic structure of the surfaces and the GB's at the characteristic concentrations as given in Table 4.2. It can be observed for all the interfaces that the formation of bilayer of the anions just begins at this concentration. Therefore, the characteristic concentration corresponds to the complexion transition of the interface from complexion I (single layer adsorption) to complexion II (bilayer adsorption) as described in the ref [100].

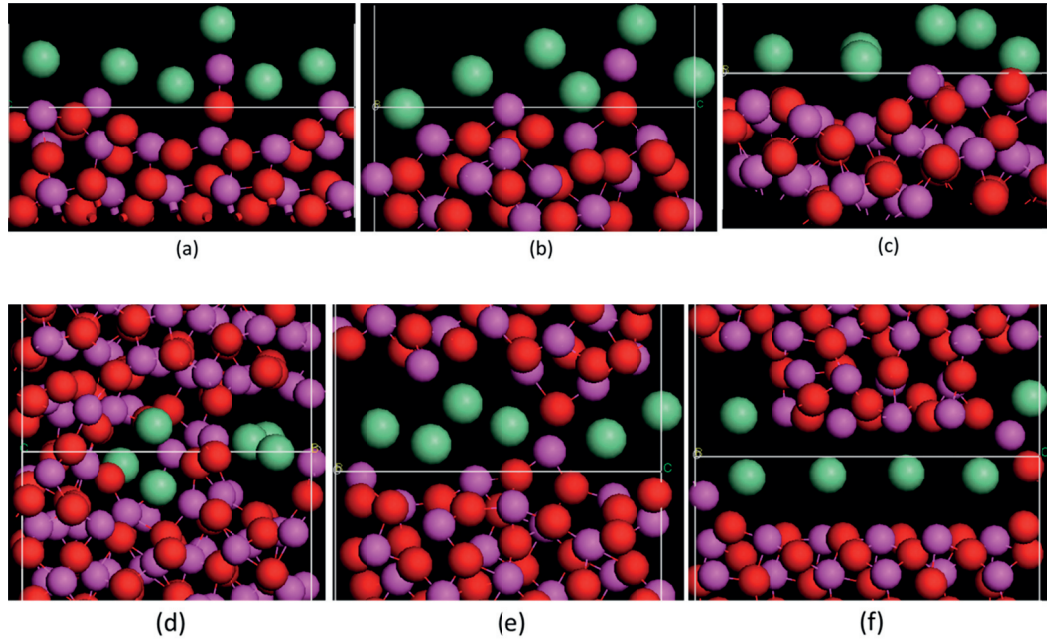


Figure 4.4. Atomistic structures of the interface at their respective characteristic concentrations as mentioned in the table 2, (a) (01.2), (b) (10.0), (c) (11.1) surfaces, and (d) (11.1), (e) (10.1), (f) (01.2) GB's. All the structures are seen parallel to the interface plane. Al atoms are in pink, Oxygen in red and Cl atoms are in green.

Figure 4.5 shows the evolution of the atomistic structure of a (11.1) GB with increasing dopant concentration. At the lowest dopant concentration (Figure 4.5 a), the Cl atoms are situated in a single layer at the grain boundary. As the concentration increases the Cl atoms start occupying a bilayer at the grain boundary. As the concentration increases further, multilayers and intergranular film of anion impurity atoms are formed at the grain boundary. According to the theory of complexation proposed by Harmer and coworkers [100], the higher order grain boundary complexions are observed as the concentration of Cl anions increases at the GB's.

Higher order complexions increase the grain boundary mobility and mass transport. Possibly anion impurities can cause the higher order complexions at lower concentrations than cation dopants due to their larger size. Combining this factor with the earlier discussed significantly higher segregation energies for anion segregation than cation dopants, may lead to the inference that anion segregation can increase the grain boundary mobility and transport and hence, cause the rapid grain growth at high temperatures nullifying the effect of cation dopants, which was observed by Dittmann et al. [97] during the sintering of Cl containing TiO_2 nano powders.

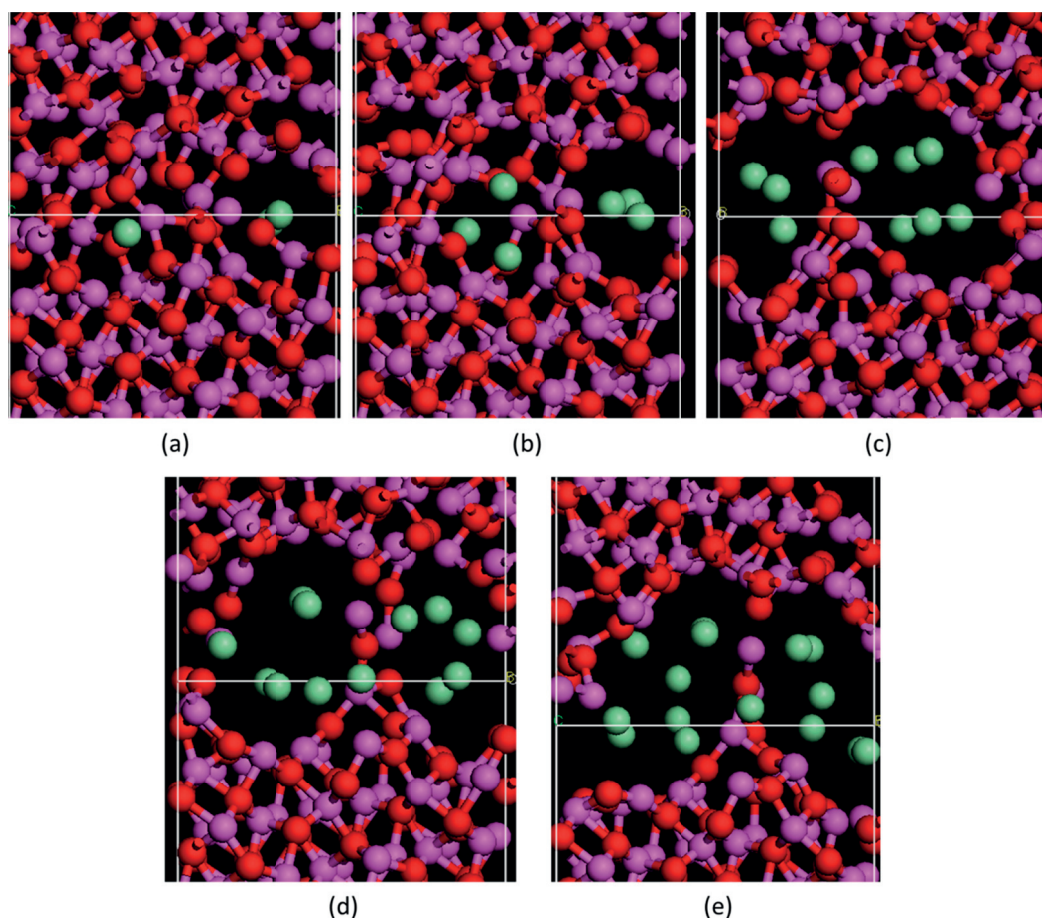


Figure 4.5. Evolution of the atomistic structure of a (11.1) GB with the increasing concentration of Cl ions, (a) 2.8 at./nm², (b) 5.6 at./nm², (c) 8.3 at./nm², (d) 11.11 at./nm², and (e) 13.90 at./nm². All the structures are seen parallel to the grain boundary plane. Al atoms are in pink, Oxygen in red and Cl atoms are in green.

4.3.4. Coordination numbers

The average Cl-Al coordination numbers (CN's) were calculated for different surfaces and GB's taking all the configurations at different concentrations into account, which are listed in Table 4.3. CN's for surfaces vary in the range of 4.3-4.9 (± 2), while for the GB's the CN's vary from 6.4 to 8.6 (± 4). The Cl-Al CN's for GB's are also very high in comparison to earlier observed CN 3 for grain boundary O-Al atoms by Milas et al. [101]. However, it should be noted carefully that the variance in the calculated coordinate numbers are relatively large. α -alumina has a hexagonal packed sub-lattice of oxygen with 2/3rd octahedral voids being occupied by Al atoms. In this arrangement of atoms CN of any O atom is less than or equal to 4 in the bulk alumina, while on a surface it should be 3 or less [102]. Higher coordination number of Cl than oxygen at the surface is an indication of stronger adhesion of Cl on the surface. In a recent study on Cl segregation in TiO₂, it was also suggested that

chlorine is chemically bonded at the TiO_2 surface, which makes it difficult to release it at lower temperatures and therefore it may get entrapped into closed porosity during the densification process. Therefore higher concentration of anion impurities should be expected at triple points and porosities. Comprehensive pore characterization study done by Stuer et al. [103] showed the existence of pores of approximately 50 nm diameter at the triple boundaries in the transparent polycrystalline alumina samples. However, the presence of these pores was attributed to the rapid spark plasma sintering, cationic dopants, and dislocations at high temperatures [103]. The results from the microstructural study carried out by F. Nabei [98] also support this observation, where STEM-EDX analysis showed the confirmed presence of Cl impurities at the triple points (section 4.3.1). Since the TEM analysis suggests the amount of Cl impurities to be approximately 250 ppm, perhaps some of the stable pores could be linked with Cl impurities and number of defects might be reduced with lower chlorine content.

Table 4.3. Cl-Al coordination numbers of different interfaces are given with corresponding nearest neighbor distances.

Miller Index	Surfaces		Grain Boundaries	
	NN (Å)	CN	NN (Å)	CN
(00.1)	-	-	3.45	8.4
(01.2)	3.36	4.3	3.38	8.3
(10.0)	3.36	4.9	3.34	8.0
(10.1)	-	-	3.38	6.4
(11.1)	3.39	4.6	3.45	8.6

4.4. Conclusions and Outlook

The topic of segregation of anion impurities in alumina has been investigated for the first time using an atomistic modeling approach. Simple technique of energy minimization was used to calculate the segregation energy of the Cl anions at 3 surfaces and 5 GB's. Buckingham parameters for Cl-Al interaction were fitted to AlOCl lattice parameters. Although the derived potential overestimates the c-axis length by ~10%, it should serve well for the preliminary qualitative study of the current topic. Strong segregation of the anion impurities to the surfaces and the GB's is expected due to 4-6 times higher segregation energies for anion in comparison to cation dopants.

Observation of the interface atomistic structures with increasing anion impurity concentration suggests that the characteristic concentration at which the slope of the segregation energy versus concentration plots changes corresponds to the

change of complexion of the GB structure from single layer adsorption to double layer adsorption of impurities at the GB. Higher order GB complexions are observed with increasing impurity concentration, which would enhance GB mobility and mass transport and hence can result into exaggerated grain growth at high temperatures.

The coordination numbers (CN) of Cl-Al at the surfaces and GB's are higher than the O-Al. Higher Cl-Al CN at the surface suggest stronger adhesion of Cl on the surface. It would make the release of anion impurities at lower temperatures more difficult and they may get entrapped into the closed porosities.

The present atomistic modeling study with the experimental work in collaboration with the CIME at EPFL has been able to demonstrate the importance of anion impurities present in alumina, which have been neglected so far in the processing of high purity alumina powders. The current results show the potential influence of anion impurities could be significant and needs to be taken into account especially for the processing of advanced ceramics where the margin for error is very small. Some of the propositions made in the present work based on the previous observations on other systems need to be confirmed with the experimental work focused on studying the effect of anions. H_2O_2 can be used to clean the Chlorine impurities from surfaces. Therefore, a comparative study on sintering and microstructural properties of as received and H_2O_2 treated alumina powder should be conducted to experimentally study the effect of Cl on alumina properties.

5. Effect of Mg on Solid State Oxygen Diffusion

In the following chapter, first we present the results of the atomistic modeling of oxygen vacancy diffusion in pure alumina. Activation barriers and oxygen diffusion coefficients for pure alumina have been calculated. In the second part, the effect of Mg impurity on the solid state oxygen vacancy diffusion in alumina is studied in order to understand the effect of nominal unavoidable impurities in commercial alumina powders. Specifically, the effect of Mg on the defect binding energies, activation barriers, vacancy stabilization and vacancy-vacancy interactions are discussed.

5.1. Introduction

Knowledge of diffusion in alumina is crucial to understand high temperature processes such as diffusional creep, sintering of ceramics, plastic deformation of single crystals and alumina scale formation in Al containing alloys. Experimentally the oxygen self-diffusion coefficient in alumina is determined via O^{18} tracer diffusion experiments at different temperatures. The activation energy (E_a) and pre-exponential constant (D_0) are obtained by fitting these results to an Arrhenius equation $D = D_0 \cdot \exp(-E_a/RT)$. The activation energy for oxygen diffusion in alumina was found to be 5-6 eV in several experimental studies [104]. Atomistic computational studies based on empirical potentials or first-principles however report the migration energy for oxygen vacancy diffusion in pure alumina to be 1-2 eV [105,106]. This failure to reconcile experimental and theoretical results for oxygen diffusion in alumina is popularly known as conundrum of oxygen diffusion in corundum, a phrase coined in [107].

The concentration of intrinsic point defects is negligibly small in alumina due to the very high formation energies (5-7 eV) [106,105 ,108] for Shottky and Frenkel defect pairs for both the Al and O. The formation energy for intrinsic oxygen Frenkel or

Schottky defects in alumina is predicted to be about 5 eV [108], which is too high for a significant intrinsic defect concentration. The defect population in alumina is therefore believed to result from charge compensation around aliovalent impurities or dopants. Heuer and Lagerlof [39] reported that oxygen vacancies are 2-2.5 times more mobile than oxygen interstitials, whereas aluminum interstitials appear to be ~100 times more mobile than oxygen vacancies. Therefore, O diffusion should occur via O vacancies, while Al diffusion should occur via Al interstitials in the undoped samples. Although diffusion experiments claim to use pure alumina, all samples contain varying levels of impurities (table 2 in [109]). Even the purest of alumina contains ppm levels of background impurities, like Ca^{2+} , Mg^{2+} , Si^{4+} or Ti^{4+} . Lagerlof and Grimes [108] have shown through static lattice calculations of defect energies coupled with mass action calculations that even such small amounts of impurities may control the defect chemistry in alumina. They further pointed out that an excess as small as 2 ppm of bivalent or tetravalent impurities can result in a change of the dominant type of defect (oxygen vacancy for Mg^{2+} , Al interstitials for Ti^{4+}) and important variations in the overall defect concentration. Hence no alumina sample can realistically be considered as undoped. In this perspective it may seem surprising that independent experimental studies on undoped alumina with varying amount of impurities result in fairly consistent results. Moreover even results for bulk diffusion of oxygen in alumina vary only modestly between doped and undoped alumina [36,110,111,112], suggesting a strong contribution from extrinsic impurities. Doremus [113] claimed that the variations observed in the experimental values of O diffusion data are within the experimental error and are caused by surface roughness, cracks and damages, but not from the impurities or dopants. Heuer [36] termed this insensitivity as buffering of oxygen diffusion in alumina.

Experimental and theoretical studies have attempted to understand the effect of dopants on the lattice [110,111,112] and grain boundary diffusion [114,115,116] of oxygen in alumina. Ti doping [111,112] is reported to decrease the bulk diffusion of oxygen while Mg either increases it [111] or leaves it unaffected [110,111]. In contradiction to what is expected from classical point defect chemistry [108], the magnitude of change in the diffusion coefficient is very small (50-100 times). The bulk solubility of typical dopants in alumina is rather small and segregation to grain boundaries is to be expected [117,118]. The effect of dopants should hence be stronger in the vicinity of grain boundaries even though in this case diffusion is also strongly altered by the modified crystal structure. Lu, Y, Zr and Sr [114,115,116] doping is reported to decrease grain boundary diffusion, while Mn and Pt doping increases it [114]. Nakagawa et al. [115] and Matsudaira et al [116] attributed the effect of dopants on grain boundary diffusion on the 'site blocking' or 'swamp out' mechanism. The 'Site blocking' mechanism suggests that the effective grain boundary area for diffusion is reduced due to the segregation of the larger size

dopants (like Y) which blocks the critical diffusive pathways and hence reduces the grain boundary diffusivity. On the other hand the 'swamp out' mechanism explains the reduced grain boundary diffusivity in presence of isovalent dopants due to the reduced segregation of aliovalent dopants (like Mg) to the grain boundaries, which will reduce the local population of defects at the grain boundaries. Yoshida et al. [114] used first principles molecular orbital calculation to show that dopants affect the net charge on neighboring oxygen ions. The dopants which induce higher negative valence charge on oxygen lower the diffusivity. Impurities were also reported to affect the concentration of available mobile defects due to the binding between impurities and defects [108,119]. Harding et al. [119] used kinetic Monte Carlo simulations to show an increase in the migration barrier of grain boundary diffusive jumps in presence of isovalent ions (La and Y) due to the 'site blocking' effect. The solid state oxygen diffusion can be affected by the dopants due to two reasons: binding energy between dopants and the defects can affect the availability of mobile defects for diffusion, and presence of dopants can also affect the activation barrier for defect migration. They also reported the defect binding energies of 0.96 eV and 1.15 eV for Y and La respectively. Similarly the activation energies of oxygen vacancy diffusion in presence of Y and La were reported to be 1.67 eV and 2.32 eV respectively at grain boundaries. Jacobs and Kotomin [106] showed using empirical potential based approach that the cation doped crystals favor cluster formation. The bivalent dopants used in the study, except Mg, were showed to facilitate solution of impurities with the interstitial cluster, whereby two substitutional bivalent ions were separated by an interstitial dopant ion on the vacant octahedral site in alumina. However, in the case of Mg, a cluster of two Mg with an O vacancy was observed to be slightly more preferred than interstitials cluster.

Although it is widely accepted that anion diffusion in alumina occurs by a vacancy mechanism, it is worth noting at this point an alternate mechanism proposed by Doremus et al. [113]. Noting that Al remains immobile under influence of applied electric field [120], Al and O have similar diffusion coefficients in some experiments [121,122], AlO is the vapor species when alumina vaporizes, Doremus suggested that the diffusing species in O and Al transport in alumina is the neutral AlO molecule. However, assumptions of similar diffusion coefficients of Al and O, viability of AlO above Al_2O_3 at elevated temperatures and easy availability of AlO neutral defects, are very much questionable [36].

In spite of previous studies on the effect of dopants on bulk oxygen diffusion in alumina it is still unclear to what extent impurities can account for the inconsistency between theoretical and experimental activation energies. The present work is the extension of the earlier work [109] done by U. Ashcauer in our group. Metadynamics [123] was used to calculate the migration barriers of the diffusive jumps in pure

alumina. Thereafter, combination of kinetic Monte Carlo [124] and Metadynamics was used to calculate the activation energy and diffusion coefficient of oxygen in pure alumina, which were found to be in close agreement with the experiments. However due to the wrong choice of the control variables, the migration barriers reported were largely overestimated and hence, the reported diffusion coefficient and activation energy were also incorrect. Nevertheless the previous work set up an apt methodology to address this kind of multi time scale and length scale problem. In spite of the erratic energies, the study gave useful insights into the issue. Three primary classes of jumps were found based on the three different diffusive jump lengths (2.42 Å, 2.54 Å, 2.67 Å). First class of jumps did not result into any macroscopic diffusion due to the closed path of the diffusive jumps, which was able to explain the buffering effect [36]. Second and third class of jumps formed the interconnecting diffusive pathways and had higher migration energies than the first class of jumps. Curved migration paths were observed for the interconnecting class of jumps.

In the present work the migration barriers were recalculated for the primary diffusive jumps in pure alumina using two different methods including Metadynamics with the corrections in the previous work. Corrected migration energies were used to calculate the diffusion coefficients and activation energy of oxygen atomic diffusion in alumina using kinetic Monte Carlo approach. Thereafter, to investigate the role of Mg on oxygen diffusion in alumina, binding energies and migration barriers of the diffusive jumps in the neighborhood of an Mg impurity were calculated based on empirical potentials. Effect of Mg on vacancy stabilization and vacancy-vacancy interaction was also analyzed. The diffusion coefficients and activation energy of oxygen atomic diffusion were calculated for impurity containing alumina also.

5.2. Approach

Our description of the energetics is again based on the Born model for solids including long-range electrostatic interactions and short-range attractive and repulsive forces described by empirical Buckingham pair-potentials. A core-shell model [125] was adopted to account for the polarizable nature of the oxygen ions. For more details of the force field, see the chapter 2 of the current thesis. The potential parameters developed by Lewis and Catlow [126] were used in the present work and the bulk structure of α -alumina was taken from Liu et al. [127]. This computational setup leads to an underestimation of the hexagonal c axis (12.43 Å) in comparison to the experimental value (12.99 Å). In order to evaluate the effect of the c-axis length on migration energies, we recomputed them using a different potential set, which better predicts the c-axis length (12.72 Å) albeit still smaller than experiment [128]. The effect of the change in the lattice dimension and a

comparison with preliminary DFT calculations (carried out at ETHZ by Dr. U. Aschauer, see annex A1) are further discussed in section 5.3.1. The General Utility Lattice Program (GULP) [129,130] was used for all defect and migration energy calculations.

5.2.1. Calculation of defect binding energies

Defect energies were calculated using two methods. First, the Mott-Littleton approach was used with 10 Å and 25 Å for the radii of region 1 and 2 respectively, which leads to well-converged energies even for the largest clusters (carried out by U. Aschauer at ETHZ). Distance dependent binding energies between oxygen vacancies (denoted as V_O from here on) and an Mg impurity (denoted as Mg_{Al} from here on) were calculated by substituting Mg onto an Al site and subsequently creating one V_O at a time on all O sites within a 6 Å radius of the Mg. After structural relaxation, the binding energy was computed by subtracting the defect energies of the V_O and Mg_{Al} computed separately.

Second, the energy minimization method was used to calculate the binding energy of V_O with Mg_{Al} . An Al atom in the center of the bulk structure was substituted by Mg and subsequently V_O 's were created in the 6 Å radius of Mg_{Al} one by one. The energy of the supercell containing an Mg_{Al} and a V_O was minimized. To calculate the binding energy of a particular configuration of Mg_{Al} and V_O cluster $[Mg_{Al}'V_O'']$, the energy of that configuration was subtracted from the energy of the $[Mg_{Al}'V_O'']$ cluster configuration, where Mg_{Al} and V_O are the farthest from each other.

5.2.2. Calculation of migration barriers

Nudged elastic band (NEB) [131] calculations were performed in a periodic 3×3×1 supercell of the hexagonal alumina unit cell. This size represents a good tradeoff between avoiding spurious interaction with periodic images and an affordable computational cost. The effect of vacancy concentration on the migration barrier of a class III jump was calculated by varying the supercell size while keeping only 1 vacancy in the supercell (Figure 5.1).

Two methods were tested to neutralize the 1e charge introduced by the combination of an Mg_{Al} and a V_O : Smearing of the excess charge over the Al sublattice or adding a neutralizing background charge. We found both options to give identical results for relative energies, such as binding energies and migration barriers; even though absolute values for formation energies show large variations compared to those evaluated using the Mott-Littleton scheme. Migration barriers for a total of 208 diffusive jumps within a radius of 6 Å of the Mg_{Al} were calculated. Initial and final states for the NEB calculations were constructed by removing oxygen ions from the initial and final position of the V_O migration pathway respectively. To determine the optimal number of intermediate images required for NEB

calculations, the calculations were done for few jumps with 10, 20 and 30 intermediate images to discretize the minimum energy pathway (MEP). It was observed that the MEP converges for 10 intermediate images (Figure 5.2). Therefore, after relaxation of the endpoint structures, NEB calculations were carried out using 10 intermediate images for the rest of the calculations. The migration barrier of a jump is extracted as the difference in energy between the initial point and the highest energy point (transition state) of the pathway.

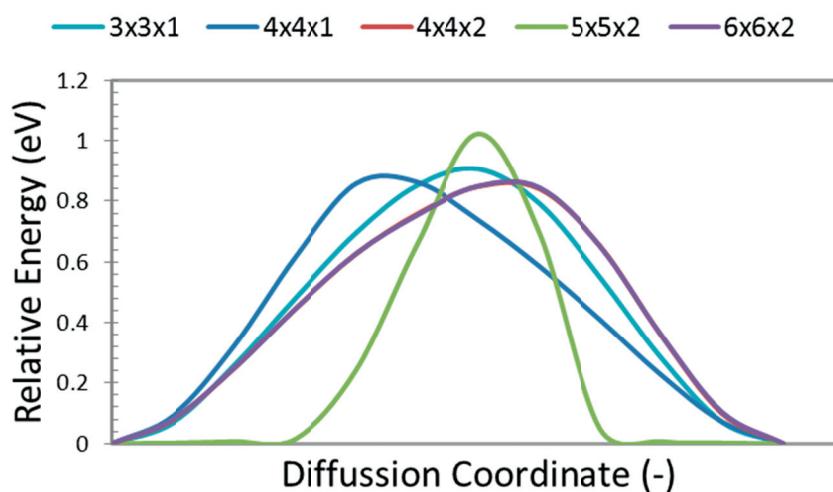


Figure 5.1. Migration barrier of a class III jump was calculated for 5 supercell sizes. The migration barrier is seen to be converging for a 3x3x1 supercell.

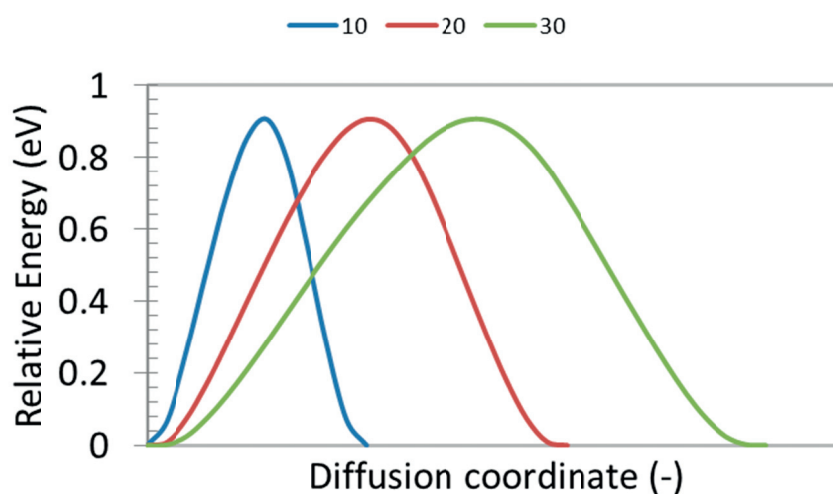


Figure 5.2. NEB calculations were done with 10, 20 and 30 intermediate images. Activation energy is shown to be converging with 10 intermediate images.

5.2.3. Calculation of diffusion coefficient

The Kinetic Monte Carlo (KMC) method was used to calculate the diffusion coefficient of oxygen in alumina. As described in section 2.7, rates of various diffusive jumps need to be calculated first to start with KMC calculations. Jump rates for the diffusive jumps were calculated using the Eyring theory [132] in association with harmonic transition state theory in the approximation of high temperature by the following equation [133],

$$\Gamma = \frac{\prod_{i=1}^{3N-6} \nu_i^0}{\prod_{i=1}^{3N-7} \nu_i^{TS}} \exp(-\Delta E_a / kT) \quad \text{Eq.5.1}$$

Where, T is temperature, k is Boltzmann's constant, h is Planck's constant, E_a is the migration barrier of the jump, ν_i^0 and ν_i^{TS} are the vibrational frequencies at the transition state and the ground state, respectively. ν_i^0 and ν_i^{TS} need to be calculated in order to calculate the pre-exponential constant and thereby, the jump rates. Use of NEB method to calculate the migration barriers allowed identifying transition state as the highest energy state in the minimum energy path, which was not possible while using Metadynamics method in ref. [109]. In the previous studies the pre-exponential constant was assumed to be the constant except the temperature for all the classes of the jumps [109]. Therefore NEB method allowed more accurate calculation of jump rates for the diffusive jumps. A 5×5×5 k-mesh was used to calculate the vibrational frequencies of the ground and the transition states' phonons using GULP. In this way the jump rates were calculated for all the 208 jumps separately in the 6 Å radius of Mg_{Al} . Effective migration barrier for the diffusive jumps starting in this region were calculated as the sum of defect binding energy and the migration barrier of the individual jump. The rates of the diffusive jumps occurring outside this region were assumed to be identical to the pure alumina. The activation energies and vibration frequencies were assumed to be constant at different temperatures to calculate the jump rates.

Once the jump rates were defined for all the jumps in a 3×3×1 supercell, the KMC simulations were carried out by randomly placing the vacancy on an oxygen site and allowing it to move through all possible primary jumps to nearest neighbor sites. KMC calculations were run for at least 900,000 steps and 100 runs were performed at each temperature in order to get a good average. The calculations were done at 4 temperatures; 1400, 1600, 1800 and 2000 K, which are situated in the sintering temperature range of alumina. The average means square displacement (MSD) over all the runs was calculated as following,

$$\text{MSD}(t) = \langle |\vec{r}(t) - \vec{r}(0)|^2 \rangle \quad \text{Eq.5.2}$$

where, $\vec{r}(t)$ is the position of the vacancy at time t . The diffusion coefficient was then calculated by using the Einstein's relation,

$$D = \lim_{t \rightarrow \infty} \frac{MSD}{6t} \quad \text{Eq.5.3}$$

Thus, the diffusion coefficient D can be calculated by the slope of the MSD vs t plot. To determine the macroscopic diffusion law, the diffusion coefficient is plotted against the inverse of temperature. The slope and y-intercept of the straight line gives the pre-exponential constant and the activation energy to define the diffusion law as $D = D_0 \cdot \exp(-E_a/RT)$.

Another modification in the current scheme of calculating the atomic diffusion coefficient instead of only vacancy diffusion coefficient was that all these calculations were done in a periodic system. The periodic boundary conditions were applied in order to track the movement of the atoms which is not possible in an aperiodic system. It allowed calculating the atomic diffusion coefficient which can be directly compared with the experimental results.

5.3. Results and Discussion

5.3.1. Migration barriers in pure alumina

Oxygen vacancy diffusion in alumina has been computed by different methods in the past [106,109,119,134,135]. Due to the high migration barriers, metadynamics [123] and NEB calculations based either on first principles or empirical potentials were the most efficient. A preliminary study was performed to check the consistency of these two methods. As shown in previous work, three different classes of primary jumps for oxygen vacancies exist in bulk alumina [109]. The migration barriers for these three primary jumps were recalculated using metadynamics and NEB based on empirical potentials. The distance between the moving vacancy and the center of mass of the rest of the ions was chosen as the control variable for the corrected metadynamics calculations. Metadynamics runs were performed with a time step of 0.0001 ps, a Nose-Hoover thermostat as well as Hoover barostat with relaxation time of 0.5 ps. In Figure 5.3 we show the migration barriers of the three classes of primary jumps computed using metadynamics and NEB. The metadynamics energy barriers slightly overestimate the NEB barriers, by an amount, which seems proportional to the barrier height. This is most likely due to the lack of directional resolution of the collective variable as discussed in [109].

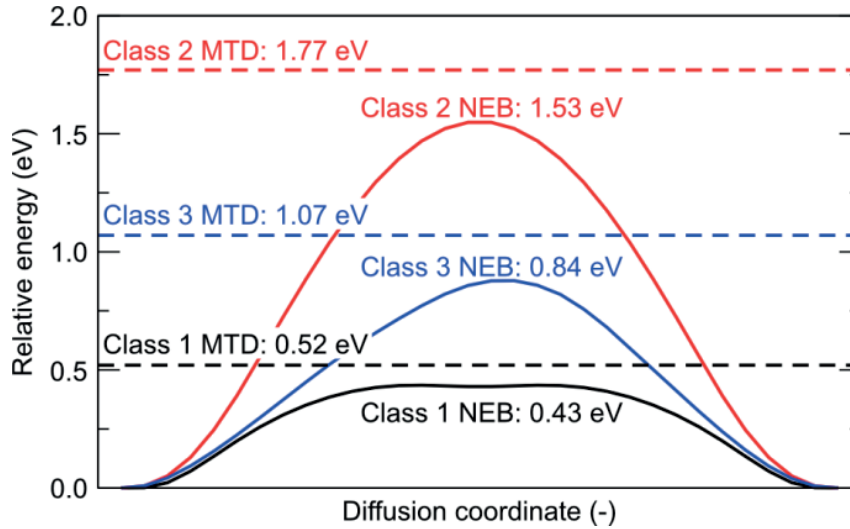


Figure 5.3. Migration barriers for the three classes of primary jumps, computed using the nudged elastic band (NEB, solid lines) and metadynamics (MTD, dashed lines) methods. For NEB the whole minimum energy pathway is given, while for MTD only the height of the saddle point is indicated.

The primary classes of diffusive jumps are similar to the ones found earlier [109], however with much lower migration energies. The first class of jumps with a jump distance of 2.42 Å has the lowest migration barrier but does not contribute to macroscopic diffusion because the V_O motion is restricted to a closed loop as previously discussed [106,109]. The second (2.52 Å) and third (2.67 Å) class of jumps form an interconnected network of jumps and can contribute to macroscopic diffusion. The second class of jumps will not contribute significantly to diffusion due to its lower jump rate (Table 5.1); therefore diffusion predominantly occurs by the third class of jumps. The migration barriers obtained by NEB and metadynamics are in a similar range for the three classes of primary jumps as shown in figure 1. As NEB yields more detailed information on the minimum energy pathway, only NEB was chosen for the remainder of this study.

As mentioned in the methods sections, the computational setup lead to underestimation of the hexagonal c-axis (12.43 Å) with respect to experiment (12.99 Å). In the section 5.3.4 we show data for the barriers computed using a second potential set [128], which gives a lattice parameter (12.72 Å) closer to experiment and also first principles density functional theory (DFT) (Annex 1, courtesy U. Aschauer) calculations, which nearly reproduce the experimental lattice. While absolute values for the diffusion dominating jumps can increase by ~0.5 eV for an expanded c-axis, we have verified that relative changes induced by the presence of Mg are unaffected. The results hence capture the relative effects resulting from the presence of Mg, while reliable absolute values for migration barriers, likely best

determined by first-principles DFT calculations, should be the focus of future research.

Table 5.1. Details of the three primary classes of diffusive jumps of oxygen in alumina

	Class I	Class II	Class III
Jump distance (Å)	2.42	2.54	2.67
Migration Barrier (eV)	0.43	1.53	0.84
Jump Frequency (THz)	4.8	6.8	21.2
Jump Rate at 1600 K (s^{-1})	7.07×10^{12}	3.18×10^9	1.29×10^{12}

5.3.2. Binding energy of oxygen vacancies

Figure 5.4 and Figure 5.5 show the binding energies calculated using Mott Littleton method and energy minimization, respectively. The binding energy of V_O with Mg_{Al} decreases asymptotically with increasing distance for both the methods. The highest binding energies of about 1.5 eV (Mott-Littleton) and 1 eV (energy minimization) are observed for V_O located in nearest neighbor sites to Mg_{Al} . These binding energies calculated using Mott Littleton are in good agreement with 1.36 eV reported by Lagerlof et al. [108], while the ones calculated using energy minimization are in good agreement with 0.9 eV reported by Harding et al. [119]. Although the energy minimization calculation show that the binding energy becomes zero at a distance of about 5-6 Å (Figure 5.5), the Mott Littleton calculation show that the interaction between the two defects is of a very long range. In fact binding energy is about 0.5 eV at 5 Å distance (Figure 5.4). However, Mott Littleton is more reliable method for such calculations because energy minimization method has a limitation of finite cell size effect and periodic image interaction affects the energy calculations. It is important to note that not only the distance between Mg_{Al} and the V_O , but also the local configuration of the cluster determines the binding energy, as can be seen from the scatter in the data in the both the plots.

This implies that V_O will be strongly attracted by Mg_{Al} over a long distance. This attraction could dramatically decrease the number of mobile defects as an additional activation energy of ~ 1.5 eV is required for the detachment of V_O in nearest neighbor positions of Mg_{Al} .

Lagerlof et al. [108] predicted the positively charged cluster consisting of one Mg_{Al} and one V_O to be dominant in samples with excess Mg^{2+} compared to Ti^{4+} impurities. Given that a cluster of one Mg_{Al} and one V_O has a net positive charge it is interesting to verify if additional vacancies can still bind to this cluster.

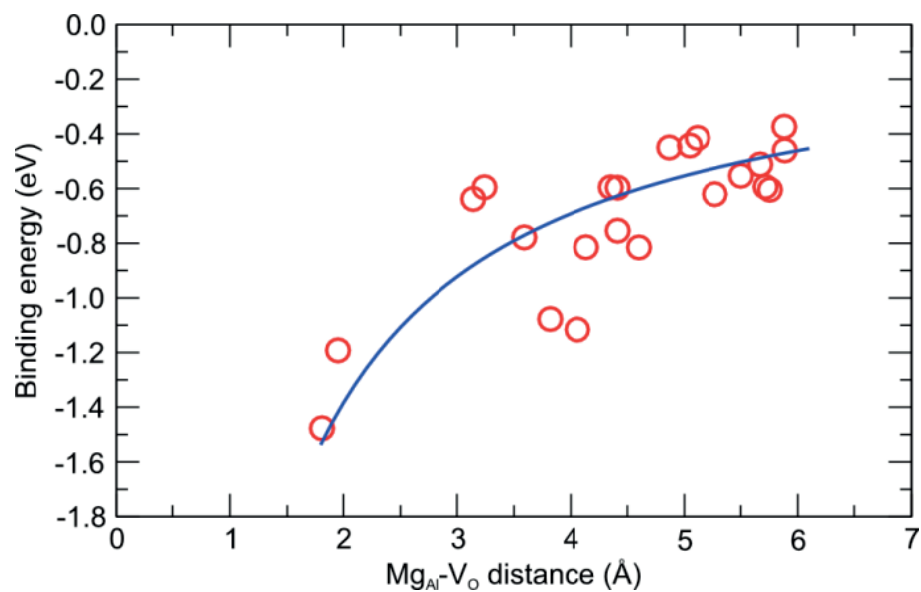


Figure 5.4. Binding energy of the V_O and Mg_{Al} as a function of their distance calculated by the Mott Littleton method. The blue line is a 1/d fit to the data.

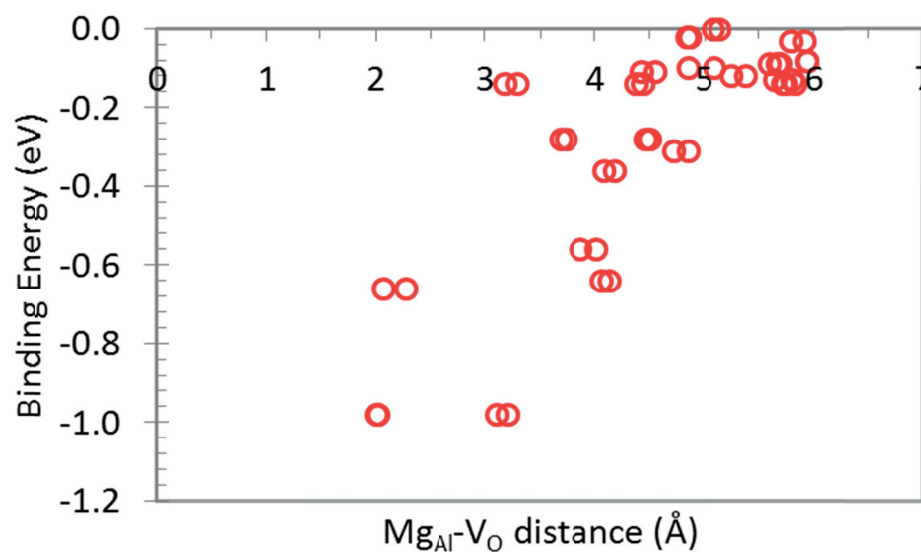


Figure 5.5. Binding energy of the V_O and Mg_{Al} as a function of their distance calculated by the energy minimization method.

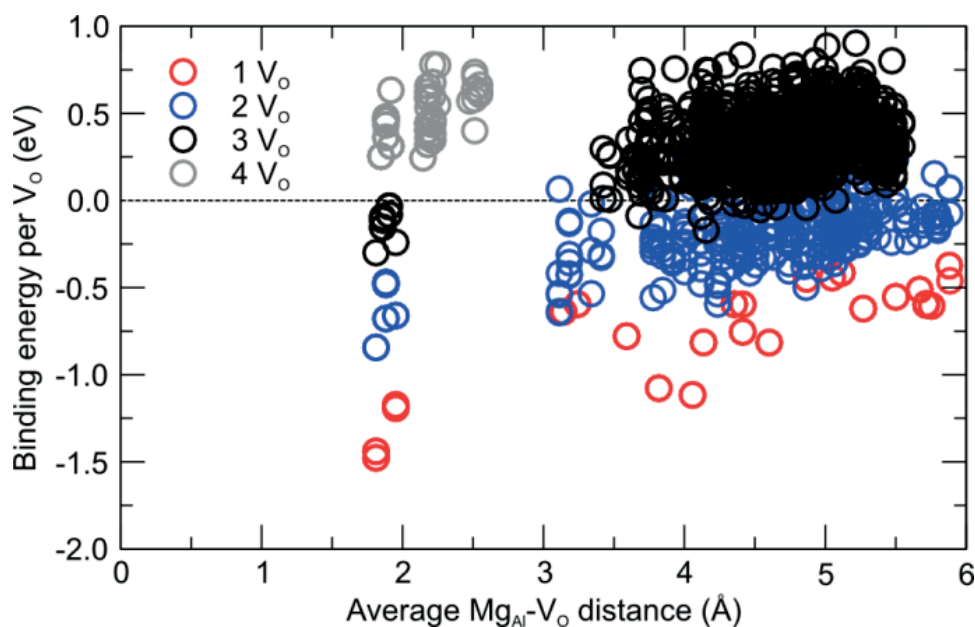


Figure 5.6. Binding energy per V_O for defect clusters of one Mg_{Al} and one to four V_O . Negative values indicate energetically favorable binding.

In Figure 5.6, the binding energy per V_O for clusters with an increasing number of V_O are presented. These calculations have been done using the Mott Littleton method. The red data points are the same as in the previous figure and are repeated here for clarity. We can see that independent of the cluster size, arrangements restricted to the nearest neighbor shell (around 1.9 Å distance) of Mg_{Al} are energetically the most favorable. There are however only six of these nearest neighbor sites, which restrict the maximum number of favorably bound V_O while still retaining a reasonable coordination of the Mg_{Al} . This is reflected in the rapid increase in the magnitude of the binding energy with increasing number of V_O and the fact that beyond three V_O the nearest neighbor cluster becomes energetically unstable. For clusters with larger numbers of V_O the accommodation in mixed nearest and next-nearest neighbor or clusters of even larger radius becomes more and more favorable. Our evaluation of clusters with a large number of V_O and large radii is restricted by the computational cost. It is therefore not impossible that an energetically favorable cluster with four V_O exists, however not with sites only in the nearest and next nearest neighbor shells.

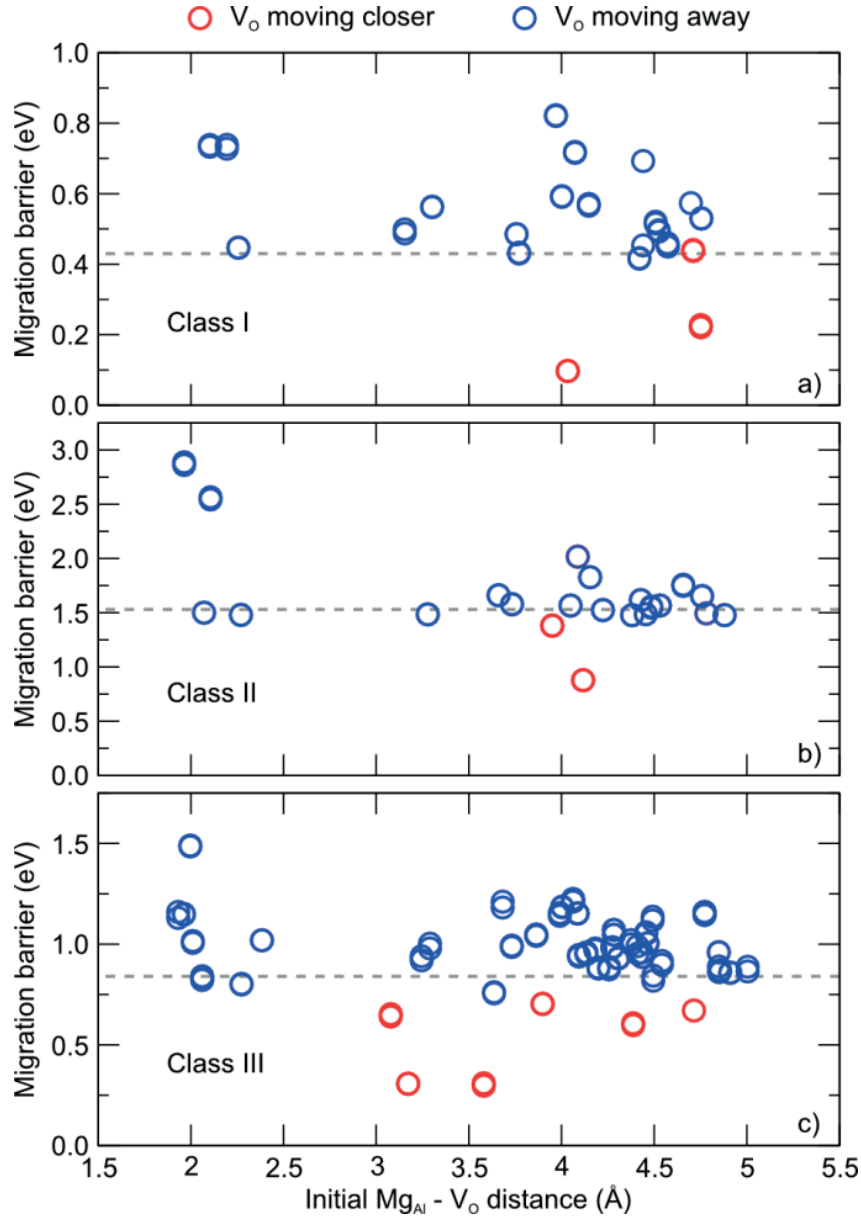


Figure 5.7. Migration barriers for the diffusive jumps of oxygen vacancies as a function of the initial distance of the oxygen vacancy from Mg for primary jumps of (a) class I (2.42 Å), (b) class II (2.54 Å) and (c) class III (2.65 Å). Dashed lines are the migration barriers in pure alumina for the respective class of jumps.

5.3.3. Effect of Mg on migration barriers

The effect of Mg_{Al} on the migration barrier of V_O jumps is characterized by three parameters: the initial distance between V_O and Mg_{Al} , whether the V_O moves 'closer to' or 'away from' Mg_{Al} and the migration trajectory.

Figure 5.7a), b) and c) show the migration barriers for the jumps of class I, II and III, respectively in the presence of Mg_{Al} . Compared to undoped alumina the migration barriers for all three classes of jumps increase or remain unchanged if the vacancies move away from Mg_{Al} . For all three classes of jumps the migration barrier increases by up to a factor 2 for jumps where V_{O} moves from the first nearest neighbor position of Mg_{Al} to a further position. On the other hand, the migration barrier is lower than in undoped alumina if the V_{O} approaches Mg_{Al} . The activation energy decreases by almost 4 times if V_{O} moves from a second nearest neighbor to a nearest neighbor position of Mg_{Al} , which is observed for jumps of class I and III.

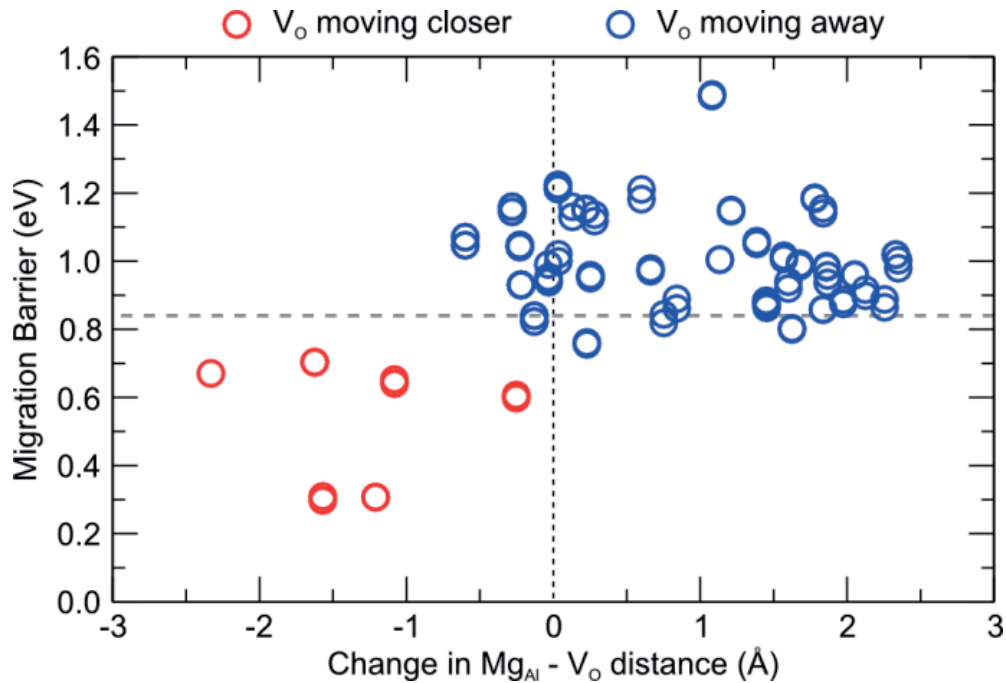


Figure 5.8. Migration barriers of class III diffusive jumps as a function of the difference in the initial and final distance of the V_{O} from Mg_{Al} . Negative values on the x-axis represent jumps where V_{O} approaches Mg_{Al} . The dashed line is the migration barrier in pure alumina.

In Figure 5.8, the data for jumps of the diffusion dominating class III as a function of the change in distance between V_{O} and Mg_{Al} is plotted. Negative values on the x-axis correspond to the jumps where V_{O} approaches Mg_{Al} and positive values to jumps increasing the distance between the two. Some points on the negative side of x-axis have higher migration barriers than in undoped alumina. An analysis of these diffusive jumps reveals them to have curved diffusion pathways. In these cases although the final vacancy position is closer to Mg_{Al} than the initial position, the curved migration path leads the V_{O} to move away from Mg_{Al} during the transition.

Analogously, the points on the positive side of the x-axis, which have lower migration barriers than in undoped alumina, exhibit curved migration paths and temporarily approach Mg_{Al} during the jump. Therefore not only the initial and final distance of V_{O} from Mg_{Al} , but also the migration path affects the migration barrier of a particular jump.

These results show that Mg_{Al} also has a rather strong effect on the diffusion kinetics in its proximity, increasing barriers for jumps leading away by up to ~ 0.4 eV, whereas jumps approaching Mg_{Al} are kinetically favored by lowering barriers by up to ~ 0.5 eV.

5.3.4. Effect of the c-axis length

5.3.4.1. Migration Barrier variations

As mentioned previously the potential model chosen in the present work [126] leads to an underestimation of the c lattice parameter (12.43 \AA) compared to experiment (12.99 \AA). In order to quantify the effect of this underestimation on the migration barriers, two additional sets of calculations have been performed: 1) using a potential set, which gives a c lattice parameter (12.72 \AA) closer to experiment [128] and 2) using first-principles density functional theory (DFT) calculations (annex A1, courtesy U. Aschauer), which are closest to the experimental lattice (12.93 \AA).

In Figure 5.10, we show the barriers for all three classes of jumps computed using the two additional methods and for reference we also repeat the Lewis (REF) barriers already reported previously. We can see that the Lewis potential generally results in barriers, which are ~ 0.5 eV lower than the ones obtained using the Binks potential. It is however difficult to judge how much of this difference is caused by the expansion of the lattice and how much is caused by the different potential parameters. Additional calculations reveal that the class 1 barrier doesn't change, class 2 jumps migration barriers are decreased, whereas for class 3 jump it is increased, when the lattice parameter is expanded. This leads to the conclusion that the systematic increase observed for all the classes of jumps in Figure 5.10 is largely due to the different potential parameters.

Looking at the DFT results in Figure 5.10 it can be seen that for jumps 1 and 3, an increase of the barrier by 0.25 and 0.5 eV respectively is predicted compared to the Binks potential. For class 2 the Binks potential barrier however almost coincides with the DFT results.

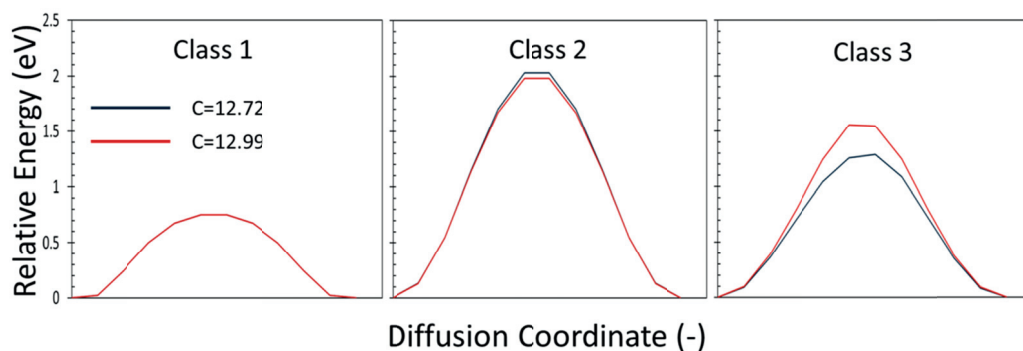


Figure 5.9. Migration barriers of three classes of jumps computed at two different c -axis lengths, keeping the potential parameters constant.

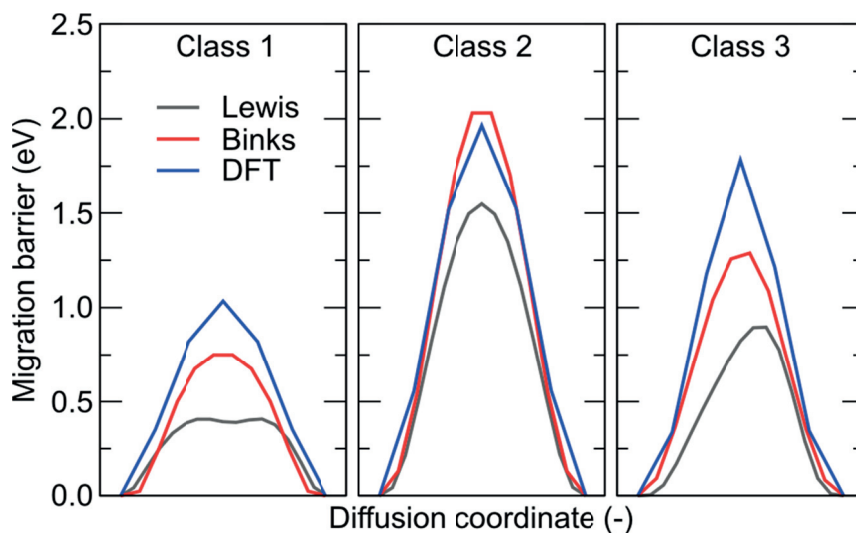


Figure 5.10. Migration barriers computed using the Lewis setup, compared to results obtained with the Binks potential and DFT calculations.

While we judge DFT calculations to be the most accurate for the determination of barriers, these results show that the computation of absolute values for barriers and hence a direct quantitative comparison with activation energies derived from experiment is affected by a very large uncertainty. This uncertainty stems from both changes in lattice geometry and changes in energetics from method to method. Therefore the conclusion is that absolute values reported in the present study are linked with a large error ($\sim 40\%$). However, in the next section it will be shown that the relative changes are well described and that the effects of Mg on diffusion, as predicted in the previous sections, are valid.

5.3.4.2. Relative Changes

In order to assess how the uncertainty on lattice parameters and energetics affect the relative effect of a Mg impurity, the change in the migration barriers when going from the pure alumina to the Mg doped system have been computed. These calculations were performed using both the Lewis [126] and the Binks [128] potential parameters at their respective lattice parameters. The results for the test set are shown in Figure 5.11. As we can see the change in the migration barrier is predicted to have very similar values for the two potential sets, the Binks potential generally predicting slightly more marked changes. The largest deviations seem to occur for the cases where changes are largest.

The good agreement between the two potential sets at different lattice parameters gives us the confidence that although, as shown above, absolute values are affected by large uncertainty, relative changes are predicted consistently. A comparison with DFT calculations would be computationally very costly and therefore has not been included in the current study but would be an avenue of future research worth following.

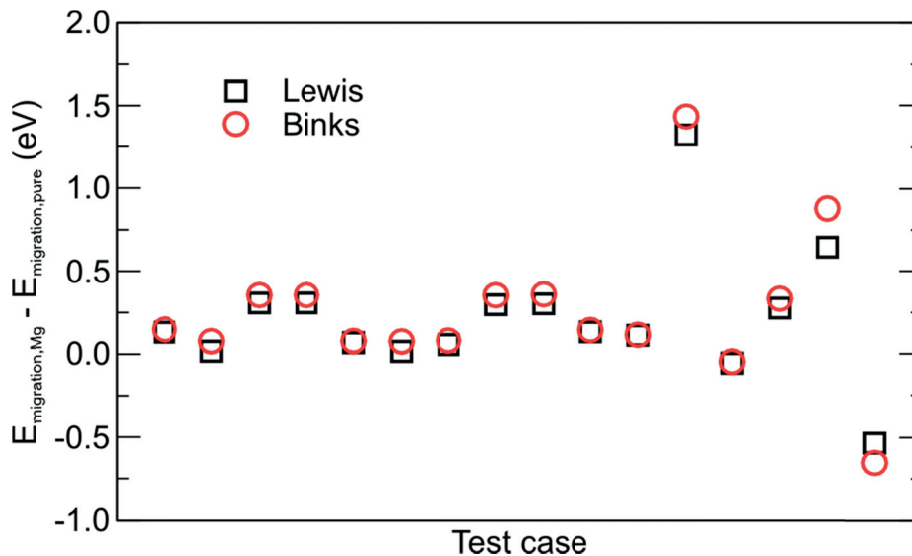


Figure 5.11. Change in migration barrier induced by the presence of Mg close to an oxygen vacancy. Results shown are for a small set of test cases.

5.3.5. Vacancy destabilization

Mg_{Al} was observed to render certain V_{O} positions unstable, the V_{O} moving to an adjacent site while relaxing the endpoint structure. This occurs only for V_{O} in second nearest neighbor positions to Mg_{Al} and the exchanges are restricted to sites linked by class I jumps. Structural relaxation due to the proximity of Mg_{Al} can hence implicitly carry out a class I jump.

These relaxations can lead to alterations of the diffusive pathways in close proximity of the Mg_{Al} . For some of the jumps, the minimum energy pathways exhibited two barriers separated by a metastable state (Figure 5.12). Upon closer inspection this metastable state is revealed to be the original initial state, the V_O having relaxed to a lower energy state by spontaneously performing a class I jump under the influence of Mg_{Al} . For the V_O to go from the new initial state to the final state, it will pass by the metastable (the original initial) state. In doing so V_O will first reverse the class I jump, which has a higher energy than in pure alumina as the V_O is attracted by the Mg_{Al} (see Figure 5.7). This is followed by the actual diffusive jump, the barrier of which can be larger or smaller than in pure alumina depending if the jump approaches or leads away from Mg_{Al} (see Figure 5.8). A schematic view of the relaxation and the two-step diffusive jump is shown in the inset in Figure 5.12. Pietrucci et al. [136] reported a similar destabilization of V_O due to the presence of yttrium in yttrium-stabilized zirconia (YSZ).

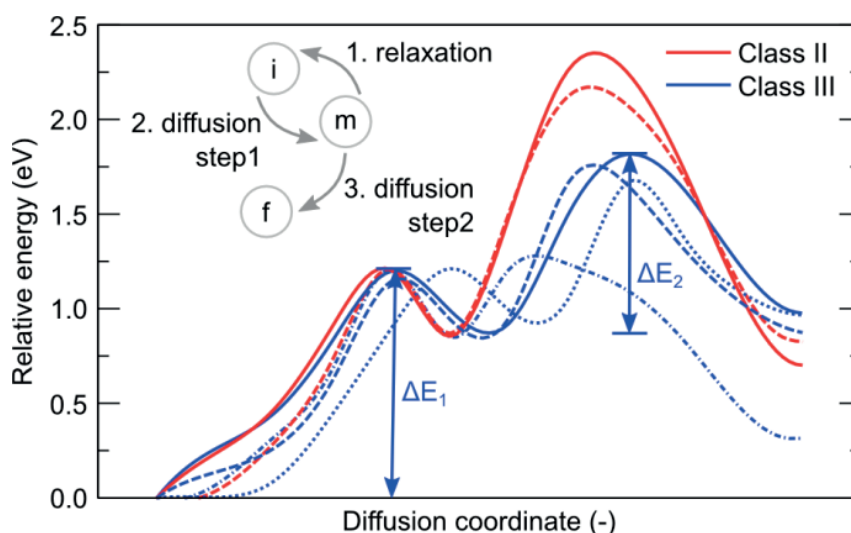


Figure 5.12. Minimum energy pathways for jumps starting from vacancy positions, which became unstable due to the presence of Mg_{Al} . The inset shows a schematic view of the relaxation process leading from the metastable (m) position to the new initial (i) position. Going from the new initial (i) position to the final (f) position now requires two diffusive jumps going via the intermediate metastable (m) state. This two-step nature is reflected by the two barriers observed in the minimum energy pathways (MEPs). The lines are cubic splines interpolated between NEB images. Red and blue solid curves are the MEPs of the highest barrier class II and class III jumps, respectively from this initial position.

It is interesting to note that a jump of class III, which previously had a barrier of ~ 0.9 eV will have a combined barrier ($\Delta E = \Delta E_1 + \Delta E_2$) of up to ~ 2.2 eV due to this vacancy destabilization and relaxation process as shown by the blue solid curve in Figure 5.12. This dramatic increase will kinetically hinder V_O 's to migrate away from Mg_{Al} .

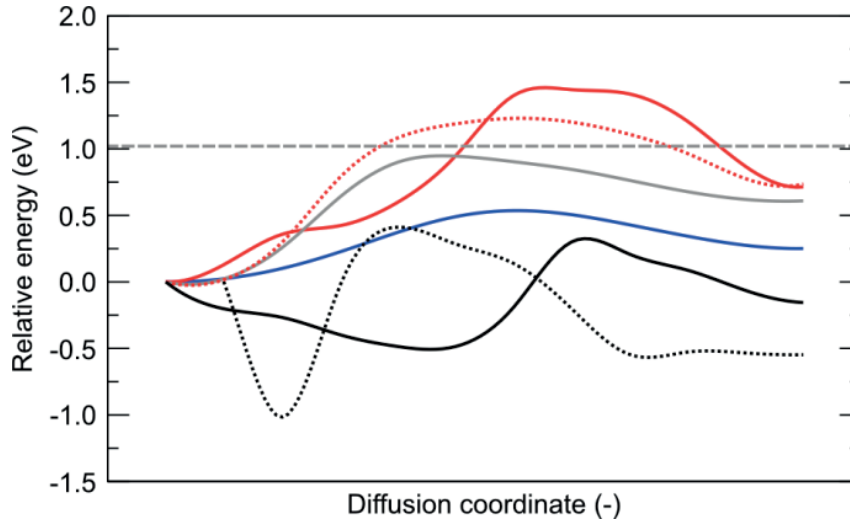


Figure 5.13. Minimum energy pathways showing the effect of V_O - V_O interaction by addition of a second V_O at different nearest neighbor sites. The dashed horizontal line is the migration barrier of the jump without a second V_O . Pathways with a destabilized initial position are shown in black, those with an increase in barrier in red, the one with an unaffected barrier in grey and the one with a lower barrier in blue. The lines are cubic splines interpolated between NEB images.

5.3.6. Vacancy-vacancy interaction effects

The aforementioned likelihood of V_O cluster formation around Mg_{Al} makes it necessary to consider the effect of V_O - V_O interaction on migration barriers. In order to gain some preliminary insights on this interaction, a particular V_O jump was carried out in presence of one additional V_O at different nearest neighbor sites. The migration barrier for this particular jump in presence of Mg but without a second vacancy was ~ 1 eV. In Figure 5.13 we can see different effects of the second V_O on the minimum energy pathway: 1) the presence of a second V_O at two different positions (black lines) destabilizes the initial V_O position, leading to metastable states and 2) depending on the position, the second V_O can either increase (red lines), leave unaffected (grey line) or decrease (blue line) the energy barrier. These observations are similar to what Pietrucci et al. [137] observed for V_O - V_O interaction in YSZ. They reported these interactions destabilize a large number of V_O cluster configurations and to strongly affect migration barriers depending on the relative position of the

other vacancies. These V_O - V_O interaction effects are governed by long-range electrostatic and medium-range elastic interactions due to the relaxation patterns around vacancies. As shown by Pietrucci [137], the correct treatment of these elastic interactions in YSZ requires fairly large simulation cells. In our Mott-Littleton calculations we found however that at a distance of 10 Å from the V_O , atomic displacements were smaller than 0.005 Å, showing that elastic effects in alumina might be of shorter range than in YSZ. This gives us the confidence that results obtained in our chosen supercell should be reliable.

5.3.7. Diffusion Coefficients

Figure 5.14 (a) shows the mean square displacements (MSD) of the oxygen atoms as a function of time at 4 different temperatures, which were calculated using the kinetic Monte Carlo simulations. Application of periodic boundary conditions allowed tracking the movement of the oxygen atoms, which was not possible in the previously used aperiodic scheme of the kinetic Monte Carlo calculations [109]. It allows comparing the modeling results directly with the experimental diffusion results. Diffusion coefficient at a particular temperature was calculated by the slope of the linear fit to the MSD versus time plot using the Einstein's equation as explained earlier in section 2.3. Thereafter, atomic diffusion coefficients (D) were plotted as a function of inverse of the temperature (T) as shown in Figure 5.14 (b). The exponential fit to the D vs $1/T$ plot gives the diffusion equation for the oxygen atomic diffusion. The diffusion equation for solid state oxygen diffusion can be written as $D = 6 \times 10^{-10} \exp\left(-0.92eV/RT\right)$.

The current scheme of the kinetic Monte Carlo calculations takes into account the effect of Mg on the defect binding energy as well as the activation energy by considering an impurity containing defective cell. However, the activation energy for the macroscopic oxygen diffusion does not change significantly due to the presence of the Mg impurity. The negligible effect of Mg impurity might be attributed to the assumptions which were made to simplify the kinetic Monte Carlo simulations. Due to the computational limitations, the area only within a radius of 6 Å of the Mg was assumed to be affected due to the presence of impurity and rest of the jumps were assumed to be identical to the pure alumina. But as seen in defect binding energy calculations (section 5.3.2), the effect of Mg might be of a longer range. Secondly, in the current study vacancy-vacancy interactions, which may be very much present due to the possibility of cluster formation around Mg, were neglected. The blocking of diffusive paths due to the destabilization of the certain vacancy configurations was also not taken into account. These limitations should be another interesting avenue for future simulations.

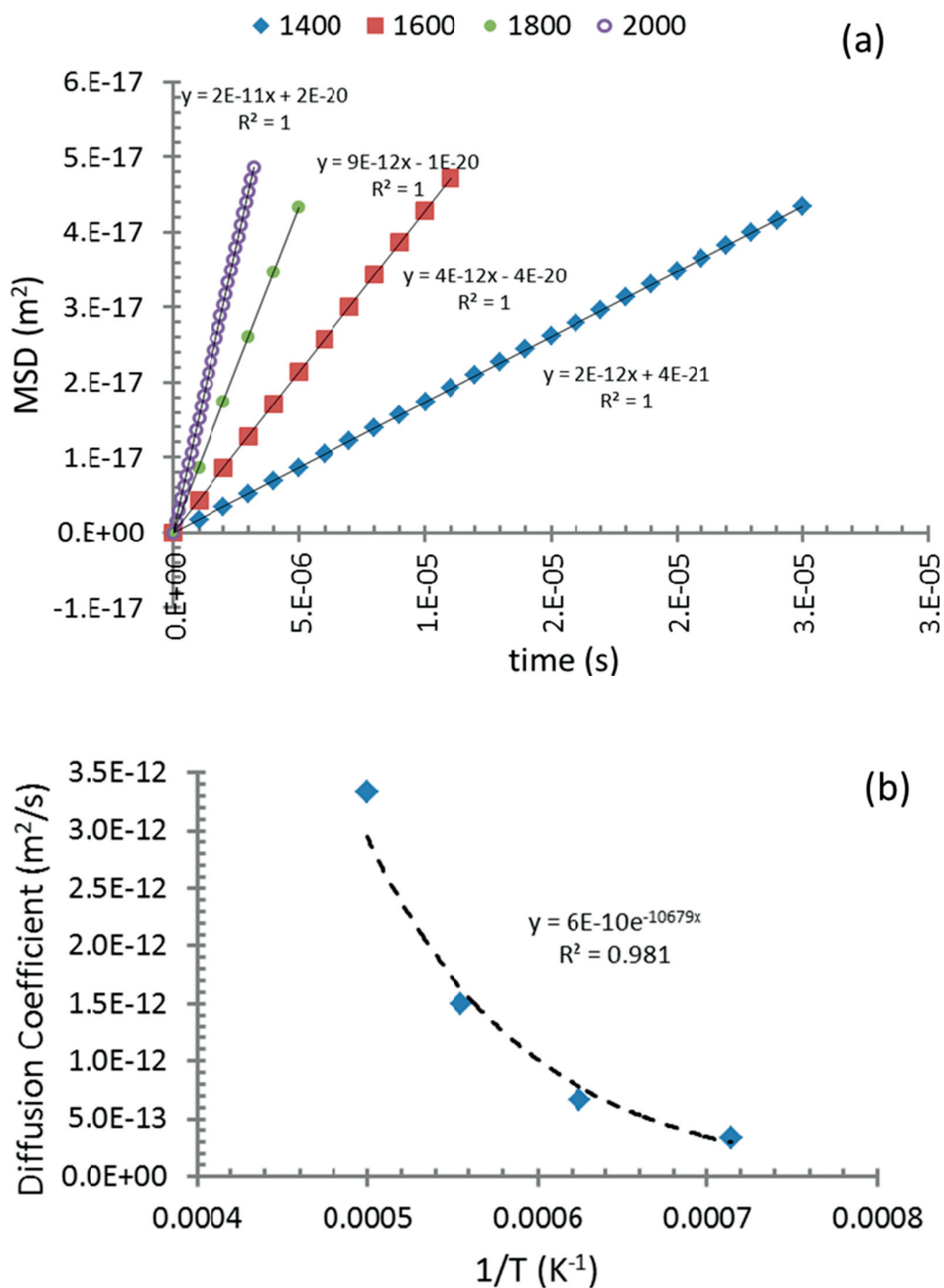


Figure 5.14. a) Mean square displacement versus time plots for oxygen atomic migration at different temperatures calculated using kinetic Monte Carlo simulations, b) Diffusion coefficients plots versus inverse of temperature to calculate macroscopic atomic diffusion law.

5.4. Conclusions and Outlook

The migration barriers leading to macroscopic diffusion in pure alumina were found to be in the range of 0.8 – 1.5 eV, which is much lower than the experimental values (5-6 eV). Grimes and Lagerlöf [108] did an extensive investigation on the defect chemistry of alumina in presence of Mg and Ti impurity. However, the effect of impurities on the defect energies and diffusion process has not been studied in detail so far in the literature. The present study for the first time attempts to study the effect of unavoidable cation impurities in alumina on the solid state oxygen diffusion by calculating jump barriers of as many as 208 jumps in the 6 Å radius region around Mg, and defect binding energies in the same region.

Substitutional magnesium (Mg_{Al}) defects lead to an energetically favorable binding of up to three oxygen vacancies (V_{O}). The first V_{O} can bind with an energy of ~1.5 eV whereas the binding energy is reduced by more than half for each subsequent V_{O} . V_{O} are most favorably accommodated in nearest neighbor positions to Mg_{Al} but the electrostatic interaction is of very long range and leads to energetically favorable clusters with larger radii (up to 6 Å radius were considered here). This implies that Mg_{Al} impurities and dopants will capture an important number of V_{O} in their vicinity, thus reducing the available number of mobile defects.

Mg_{Al} also affects the migration barriers of V_{O} in alumina. Jumps towards Mg_{Al} become kinetically more favorable by a factor 4, whereas those away have their barrier increased by a factor 2. This will also kinetically favor a large concentration of V_{O} in the vicinity of Mg_{Al} .

Given that the effect of an increased barrier and the binding energy are additive to the migration energy of V_{O} , Mg_{Al} may account for a 2-3 eV increase in the total activation energy of diffusion of oxygen vacancies. Another effect caused by Mg_{Al} is the destabilization of certain vacancies, which converts single diffusive jumps into two subsequent jumps with an overall increase in barrier of almost 1 eV. This will further hinder diffusion, as was reported for yttrium stabilized zirconia [136].

This leads to the picture that Mg dopants and impurities in alumina will lead to a reduction of the number of mobile V_{O} 's as well as an increase in their migration energies. On the other hand Grimes and Lagerlöf [108] showed that Mg excess dramatically increases the number of V_{O} 's. The diffusion coefficient is hence possibly determined by an antagonistic effect between the increased total number of defects and their reduced mobility. It is possible that in conjunction with the homogenization of interfacial energies, [117] the slower diffusion kinetics possibly explain the microstructure homogenizing effect, which Mg dopants have on alumina by a gentler sintering.

In conclusion dopants or impurities have a significant influence on the V_o diffusion process in alumina. The methods used here to estimate the energy barriers probably lack the accuracy on absolute values needed to give us quantitative comparison with experiment. General trends however are coherent within quite different computational setups. Our results indicate that the effect of the impurity population found in experimental systems could contribute to the high experimental values for diffusion activation energies, when compared to those calculated in pure alumina systems. But it must be recognized that real systems are complex consisting of variety of impurities. It will be a daunting task to take into account the effects of various impurities present in an alumina system using the current atomistic scale methods. Therefore, future work needs to take into account this added complexity on a larger scale to better approach experimental systems and provide a direct quantitative comparison.

6. Linking Modeling with Experiments

In an effort to link experimental results with the modeling, calculations of yttrium dopant segregation on a near coincidence grain boundary (more realistic than a twin grain boundary) will be presented in the following chapter. First the results of the microstructural characterization of a transparent alumina sample carried out by our collaborators will be presented. The modeling calculations will be discussed, which were done on a experimentally well characterized grain boundary, including segregation energies, atomistic structures, grain boundary densities and coordination number.

6.1. Introduction

Since a detailed literature survey of the segregation of cation dopants (Y, La, Mg) on twin grain boundaries was provided in chapter 2 of the current thesis, only the literature relevant to highlight the importance of the present work is given here. Majority of the computational segregation studies [138,139,140,141] have been done on the highly symmetrical twin grain boundaries of varying complexities to minimize the computational cost, which is required to simulate non symmetrical, large general grain boundaries. However, the fraction of special twin grain boundaries found in the sintered alumina samples is reported to be very small. Transmission electron microscopy studies of undoped alumina samples showed that grain boundary misorientation was randomly distributed and the fraction of near coincidence grain boundary was very low [142]. It was reported by the same group that the microstructure of alumina does not change significantly due to the yttrium doping [143], however Mg doping increases the number of near coincidence grain boundaries [144]. Cho et al. [145] later confirmed these findings by statistical determination of GB misorientation using electron back scattered Kikuchi diffraction

(EBKD). Proportion of coincidence site lattice boundaries was reported to be very low (1-5%).

Although it has been shown in experiments conducted on metal system that the lowest degree of segregation occurs on the grain boundaries with higher atomic densities [146], there are not enough conclusive evidences to conclude the same in case of alumina ceramics. In addition, the variation in grain boundary volume versus concentration across different experimental studies can make them difficult to compare with one another. Yttrium was found to be below the detection limit in a singular boundary $\Sigma 3$ and boundaries close to the $\Sigma 7$ orientation relationship. The very low yttrium content was also found in a faceted GB and a general GB [147]. On the other hand Bouchet et al. [143] found that yttrium segregates to all the grain boundaries in Mg-Y codoped as well as Y-doped alumina with few exceptions. Yttrium was not detected on a general GB, but its level was high in a low angle GB and in a boundary close to coincidence orientation relationship. It was suggested that there is no direct relationship between three dimensional coincidence relationship and GB segregation and the nature of solute and solvent atoms also needs to be taken into account in addition to the boundary characteristics [148].

In this light of the experimental observation of mostly general grain boundaries in doped and undoped alumina, and the missing direct link between experiments and the atomistic modeling, efforts are required to simulate the real grain boundaries. It will also help understanding how far are the observation made on simple twin GBs in the simulation are extendable to the general grain boundaries in the real alumina samples. In the present the segregation calculations were done for a Y-doped alumina near coincidence GB, which was also observed experimentally in a transparent alumina sample. Segregation energies and interface structure analysis results will be discussed in the following sections.

6.2. Approach

Transparent polycrystalline α -alumina samples were prepared in our group (by M. Stuer) from polyhedral near spherical powders with median particle size D_{v50} of 510 nm and specific surface area of 4.2 m²/g. Samples were doped during the colloidal processing step with 225 ppm quantity of both La and Y. Microstructural analysis of this sample was carried out at the Centre for Electron Microscopy (CIME) at EPFL by F. Nabiei [149]. FEI Tecnai Osiris Microscope was used at 200 kV with a Field Emission Gun (FEG) for scanning transmission electron microscopy for imaging and analytical data acquisition. Energy dispersive X-ray spectroscopy analysis was done using Super-X SDD EDX detectors to collect the data of the sample composition along with the imaging. Large angle convergent beam electron diffraction (LACBED) analysis was used to characterize the GB planes and orientations of the selected GBs

in the sample. The amount of dopants present in the GB was determined using the line scan analysis of the GBs.

A microstructurally well characterized general GB was selected for the atomistic modeling of the dopant segregation at a general GB. Near coincidence site lattice (NCSL) method was used to simulate the chosen general GB as mentioned in the chapter 2. Certain approximations were made in order to simulate the general GB using NCSL approach, which will be discussed in the section 6.3.1. Segregation energies of the single individual cation sites were calculated first by substituting dopant ions on the cation sites one by one. The screening method described in the chapter 2 was used to simulate the doped interfaces with varying dopant concentrations. Segregation energy of Y-dopant to the GB was calculated using the following expression,

$$\Delta H_{seg}(N_Y) = \frac{(H(N_Y) - H(0) - N_Y \Delta H_{Y,bulk})}{N_Y} \quad \text{Eq.6.1}$$

$\Delta H_{seg}(N)$ is the enthalpy of segregation in a structure containing N Y-dopant ions, $H(N)$ is the potential energy of the structure containing N dopant ions, and $\Delta H_{Y,bulk}$ is the change in the enthalpy when inserting a dopant ion in the bulk. Segregation energies were calculated at 7 concentrations, and 20 different configurations were calculated for each dopant concentration. Y-O coordination number was calculated with a cut off distance of 2.9 Å [138].

6.3. Results and Discussion

6.3.1. Microstructural characterization of grain boundaries

Figure 6.1 shows the high magnification EDX analysis results (carried out at CIME, EPFL by F. Nabiei) confirming the presence of Y and La cation dopants and Cl impurities at a GB and triple points. Y and La were reported to be segregating together on all the GBs. On an average amount of segregated Y (2.8 atoms/nm²) was more than La (2.3 atoms/nm²) on 7 randomly chosen GBs, which were quantitatively characterized using EDX line scan analysis. The dopants were found to be confined in the narrow region at the center of the grain boundary (Figure 6.2). The concentration of the dopants at the grain boundary was estimated to be 370 ppm, which is 82% of the nominal concentration of the dopants, i.e. majority of the dopant atoms segregate to the GBs. Although not an extensive study was done to characterize the type of different GBs present in the codoped alumina sample, all the investigated GBs were found to be high angle general GBs. Table 6.1 gives the details of three GBs identified including the dopant concentrations and the grain boundary planes of the adjacent grains.

GB B2 (Table 6.1) was chosen in the present work for the atomistic modeling of Y-dopant segregation. The GB planes were simplified by lowering the indices of the planes in order to optimize the computational cost. (4,2,-19) plane was approximated to (00.1) and (1,-9,-26) plane was approximated to (0,1,3). The angle between the approximated planes (18°) is maintained close to the angle between the original planes (27°).

Table 6.1. Concentrations of the Y and La dopants at three grain boundaries determined using EDX line scan analysis. It also gives the parallel planes of the adjacent grains and the misorientation angle of the GBs.

	Y/nm ²	La/nm ²	Angle (°)	GB ^{el} planes
B1	3.17	2.21	87°	(-7,-2,4) (1,5,5)
B2	3.19	2.77	27°	(4,2,-19) (1,-9,-26)
B3	2.28	3.21	168°	(2,-1,36) (-2,3,-14)

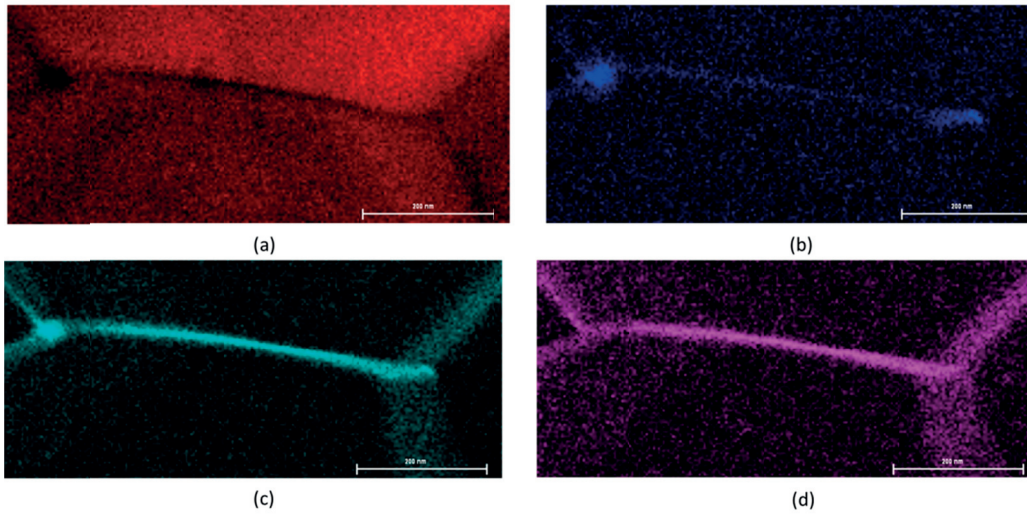


Figure 6.1. STEM-EDX spectroscopy results showing the presence of dopants and impurities at a grain boundary, (a) Aluminum, (b) Chlorine, (c) Lanthanum, and (d) Yttrium.

6.3.2. Segregation Energies (ΔH_{seg})

Before starting the discussion on the GB segregation energies, it should be noted that due to the large area of the GB (5 nm^2), the number of atoms in the region 1 (relaxable region) of block 1 and 2 is very high (see chapter 2, section 2.2). Therefore the thickness of the region 1 in block 1 and 2 had to be reduced in order to be able to do the Newton Raphson minimization of the energy function, which will affect the

accuracy of the GB segregation energies. Therefore the calculated absolute energy values need to be considered with caution.

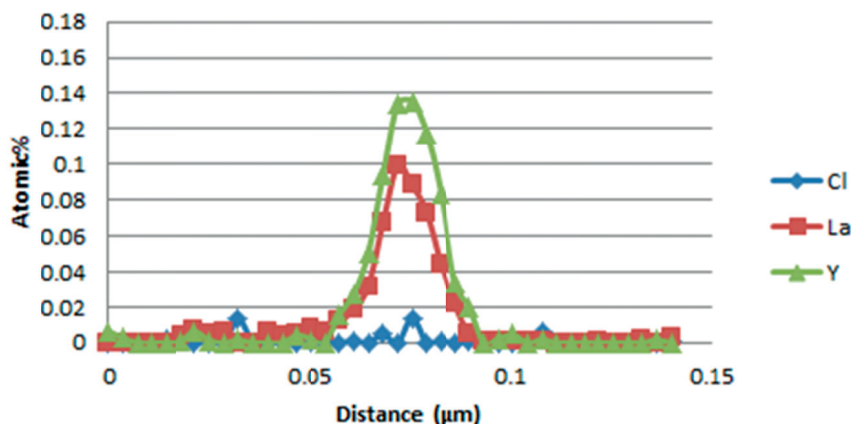


Figure 6.2. Line scan quantitative EDX analysis of a GB showing the presence of La and Y in the narrow region of the GB.

Figure 6.3 shows the ΔH_{seg} of the single cation sites as a function of their distance from the GB. The ΔH_{seg} for single cation sites in 2 Å region on both sides of the GB varies from -3.3 to 15.7 eV/atom. Not all the cation sites situated in this region are energetically favorable for segregation of Y dopants. In fact, only a small fraction (~25%) of the sites is energetically favorable for segregation. This is in contrast to the depth profile observed in the case of Y-segregation on twin GBs, where almost all the cation sites are energetically favorable for segregation and ΔH_{seg} varies in ~-5 to 0 eV/atom range. It implies that the cation dopants will not occupy all the cation sites at the grain boundary at higher concentrations, rather they will occupy specific energetically favorable site. Shibata et al. [150] also characterized a high angle $\Sigma 13$ GB using Z-contrast STEM. It was shown that the Y-atoms preferentially occupy specific atomic sites on the interface plane, which is in agreement with our current calculations on a near coincidence GB (referred as NCGB hereafter). Another point to note is that in the simulated NCGB one of the planes is parallel to the basal plane which is a high atomic density plane. Therefore larger size Y-atoms will have less space to be accommodated at the GB. Gülgün et al. [147] also reported one general GB with a basal boundary plane in one grain, which displayed lower yttrium content than other GBs.

Figure 6.4 shows the ΔH_{seg} as a function of Y-dopant concentration at the NCGB. ΔH_{seg} is negative for almost all the configuration at different concentrations including at the concentration of the Y-dopant (3.2 atoms/nm²) calculated using the EDX-analysis. Due to the large surface area of the GB (5 nm²), higher concentrations could not be calculated for the GB. Therefore, it does not give any idea of a pattern of the

ΔH_{seg} plot with the concentration. ΔH_{seg} varies in the range of -3 to 3 eV. There are a higher number of configurations of the highest energy sites possible at the higher concentration; therefore the ΔH_{seg} is negative for all the configurations at higher concentrations.

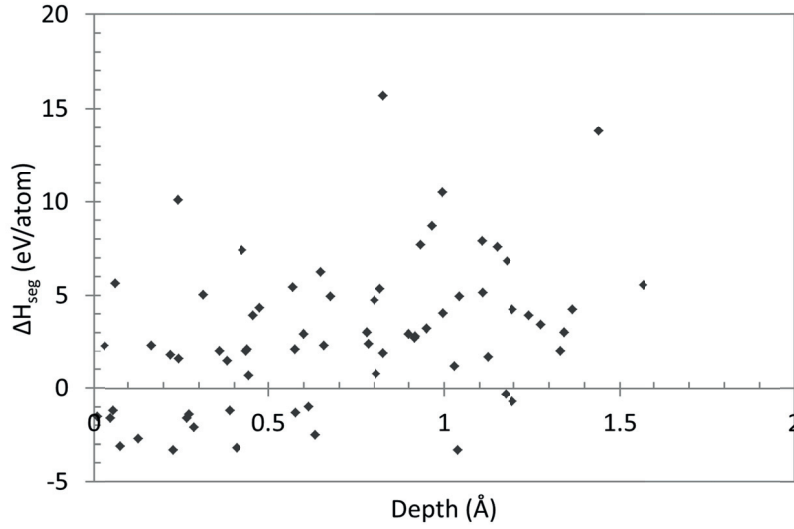


Figure 6.3. Segregation energy for single yttrium dopant sites situated at different depths from the near coincidence GB with (00.1) and (01.3) as GB parallel planes.

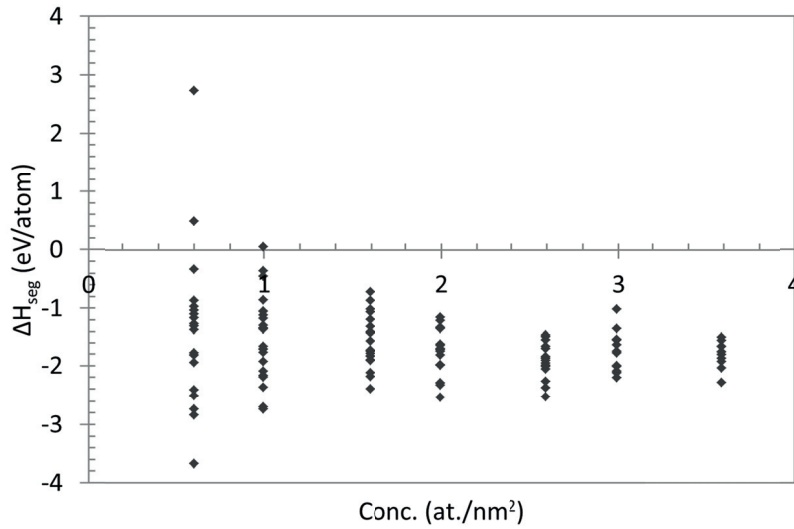


Figure 6.4. Segregation energy versus dopant concentration plot for the near coincidence GB with (00.1) and (01.3) as GB parallel planes.

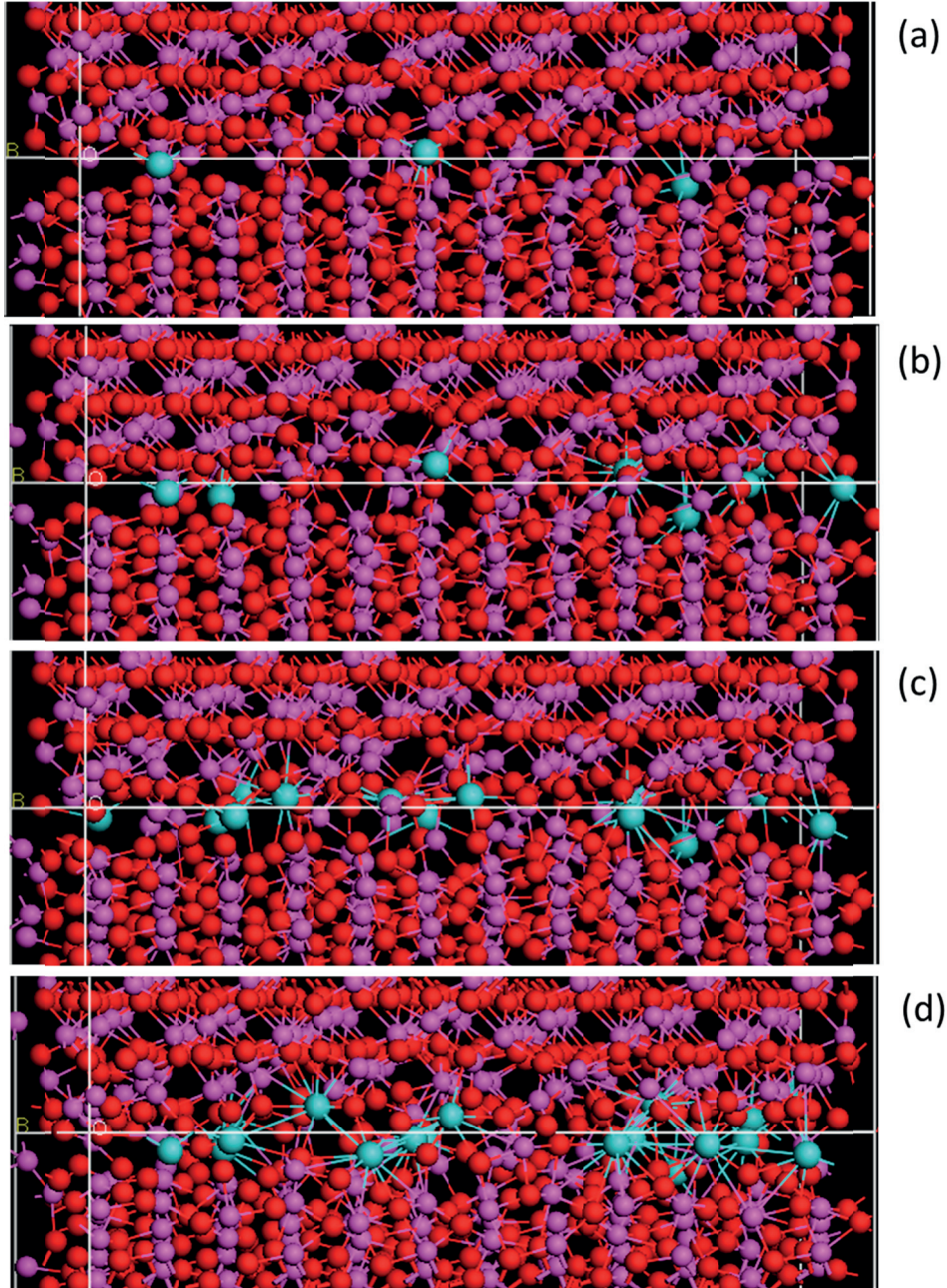
6.3.3. Atomistic Structures

Figure 6.5 shows the atomistic structures of the Y-doped NCGB at varying Y-dopant concentrations. It can be observed that dopants occupy the positions in a bilayer fashion at the GB for all the calculated concentrations. In contrast to the twin GBs where the dopants arrange themselves in the single layer (complexion 1 [151]) at lower concentrations, the occupancy starts in a bilayer fashion (complexion 3 [151]) in case of a NCGB. It will supposedly increase the GB mobility and transport of NCGBs in comparison to the twin GBs with complexion 1 as proposed by Harmer and coworkers [151]. But the segregation is confined to the double layer at the GB; it does not go beyond that for the concentration range calculated here. Although Shibata et al. [150] reported a two dimensional array of selectively occupied Y-dopant atoms using STEM analysis, high resolution images of general GBs in a polycrystalline alumina by Wang et al. [152] showed that the GBs are not disordered beyond one or two atomic planes in materials with low impurity content. These experimental observations are in good agreement with the atomistic modeling results of the cation segregation at twin GBs (chapter 3) as well as at a NCGB being discussed here. However it suggests that the dopant segregation does not produce the solute pinning effect on general GBs at any dopant concentration and hence should not suppress the grain growth according to the proposition in ref [151], which is not the case experimentally. However, it should be noted that some of the lower energy configurations might have been missed due to the limited number of configurations calculated for each dopant concentration in the current study.

Y-O coordination number (CN) was calculated for the segregated interfaces at different Y-dopant concentration using the cut off distance as 2.9 Å. Y-O CN was calculated to be 6.4 ± 0.9 . The nearest neighbor distance was found to be 2.32 ± 0.05 Å. The CN and nearest neighbor distances are very similar to the ones calculated earlier for twin GBs [138,140,141]. CN is higher in comparison to the experimentally calculated CN=4.2 at 3 Y/nm² [152]. However the lower CNs observed experimentally were attributed to the fact that the calculated CNs on a whole α -alumina sample might be the result of mixture of Y-O distances with a comparatively large variance. The packing density of the NCGB was calculated to be 0.24 which is much lower than the packing densities of the twin GBs (0.5-0.7) calculated earlier (chapter 3), which shows the more amount of space available for the larger size dopants at the NCGB. But it still does not result into higher segregation energies. Therefore, lower segregation energies of the Y on NCGB indicate that the segregation of cation dopants does not depend only on the size mismatch of the dopant ions, but depends also on the atomic structure of the interface.

Table 6.2. Summary of the ΔH_{seg} at experimentally observed concentration and coordination number (CN) and near neighbor distance (NN).

Conc. (at./nm ²)	ΔH_{seg} (eV/at.)	CN	NN (Å)
2.99	-2.20	6.4±0.9	2.32±0.05

**Figure 6.5.** Atomistic structures of a Y segregated near coincidence GB at different Y-dopant concentrations, (a) 0.60 at./nm², (b) 1.60 at./nm², (c) 2.59 at./nm², and (d) 3.59 at./nm². All the atomistic structures are seen parallel to the GB plane. Yttrium atoms are in blue, oxygen red and aluminum atoms are in pink.

6.4. Conclusions and Outlook

STEM-EDX analysis of the La-Y codoped α -alumina samples confirmed the presence of La and Y-dopants on all the GBs. Almost 80% of the cation dopant atoms were confined in the GBs. All the investigated GBs were found to be general GBs with average 2.8 atoms/nm^2 Y-dopant concentration and 2.3 atoms/nm^2 La concentration.

One of the general GB observed in the microstructure was simulated using the near coincidence site GB approach with (00.1) and (01.3) as the GB parallel planes in the adjacent grains. It was found that only $\sim 25\%$ of the cation sites in the 2 \AA region of the GB are energetically favorable for the Y dopant-segregation, which is in good agreement with the earlier experimental observations of Shibata et al. [150], where they observed Y-dopants occupying only specific cation sites at a $\Sigma 13$ GB. This will reduce the configuration entropy of the segregation on general GBs. The segregation energy of multiple dopant configurations was found to be negative for all the calculated concentrations except few at the lower concentrations. Hence, although the segregation of Y dopants is energetically favorable, dopants occupy certain specific cation sites at the GB.

Atomic structure analysis showed that the dopants are arranged in a bilayer fashion as opposed to single layer in case of special twin GBs (chapter 3), which is supposed to enhance the mobility as well as the transport of a NCGB in comparison to twin GBs. However, more number of configurations needs to be calculated for each dopant concentration in order to confirm this result. Lower segregation energies in spite of the low atomic density of the GB suggest that the segregation is not only dependent on the size mismatch, but also on the GB structure.

Due to the large GB area, size of the regions where atoms can relax was kept small for the energy minimization in order to keep the simulations within manageable computational resources, which would affect the accuracy of the absolute values of the energy. Molecular dynamics simulations or BFGS energy minimization of the doped GBs should be done in order to get more accurate estimate of the segregation energy values.

The present study of segregation on a general GB also shows that one needs to be careful in extrapolating the findings of the atomistic modeling of the simple twin GBs to the general GBs which are abundant in polycrystalline alumina samples. In some way, the current study provides a point which can be used to more accurately extend the findings of the simple twin GBs calculations to the more general GBs.

7. Preliminary Work: Surface Adsorption of Dispersants

7.1. Introduction

Defect free green body processing is essential for achieving high density ceramics with minimum grain growth. Preparing a uniform stable suspension of ultrafine ceramic powders is very difficult due to the tendency of agglomeration of high specific surface area fine ceramic powders. Polymer dispersants are often used to stabilize the alumina suspensions by steric as well as electrostatic repulsive forces. A recent atomic force microscopy (AFM) study [153] of alumina suspensions dispersed with carboxylic acids showed that more than 90% of the inter particle repulsive forces are contributed by the steric repulsion. Conformational entropy of the polymer adsorption plays an important role in the effectiveness of the steric forces. The conformational arrangement of PAA on the alumina surface determines the steric force and can be affected by the polymer structure and concentration [154,155,156]. At low concentration it is adsorbed in tail type formation. At slightly higher concentration conformation changes to train type configuration and finally on further increase in the concentration it changes to loop and tail configuration which corresponds to maximum decrease in the viscosity of the suspension. However, these propositions have been made based on the observed colloidal suspension stability behavior, but there is no experimental evidence to confirm the proposed hypothesis. Although AFM have been used effectively to determine the adsorption layer thickness [153], but still it is still not trivial to experimentally observe the conformations of the adsorbed polymers in the suspension.

Franks et al. [157] studied the charging behavior at the alumina water interface. They found that there are differently coordinated aluminum surface hydroxyls and therefore, their pK_a values also differ. Concentration of singly and doubly coordinated surface hydroxyl groups varies on different alumina surfaces. While basal planes have majority of doubly coordinated hydroxyls, singly coordinated

hydroxyls are found in greater proportion on prismatic, high index planes and the edge of steps on the basal plane. Surface dependent charging behavior of alumina can result in a surface dependent adsorption behavior of organic dispersants on alumina, which is to some degree governed by the electrostatic interaction between the two. Dringen et al. also reported that the binding of the Glutathione disulfide on the alumina surfaces is primarily driven by the electrostatic interaction via the carboxyl groups [158].

Das et al. [159] reported that the adsorption of PAA in the alkaline pH range is mainly due to the charge patch neutralization mechanism and hydrogen bonding between carboxyl groups and surface OH_2^+ . The interaction of polyelectrolyte and alumina surface has been mostly reported to be electrostatic in nature. But Hidber et al. [160] and Gocmez [161] reported the formation of a complex on the surface in their experimental and molecular dynamics (MD) simulation studies respectively. However, the MD simulations carried out so far on alumina surfaces [158] were done on a frozen surface, or surface in vacuum without water [161].

The goal of the present work was to use MD to study the adsorption behavior of commonly used dispersants such as acetic acid, glycolic acid, citric acid and polyacrylic acid (PAA) on alumina surfaces. Another objective of the current work was to investigate the adsorption behavior of dispersants on different crystallographic surfaces of alumina. As expected from the work of Franks et al. [157] surface specific adsorption behavior of dispersants on alumina surfaces will help explore the possibility of particle orientation in colloidal suspensions and thereby grain orientation during sintering..

7.2. Approach and Implementation Issues

Molecular dynamics simulations were done using empirical force field approach. De Leeuw and Parker [162] potentials were used for the interaction in the hydroxylated alumina surface. DREIDING [163] organic force field was used for intra-polymer interactions. TIP3P potential [164] and, the De Leeuw and Parker potential [165] with hydrogen bonding correction term [166] were tried for the water in the present work. Lennard-Jones potential parameters (ϵ and σ) for alumina surface were derived using the similar approach as by Dringen et al. [158]. Energy of a simulation cell containing surface and the polymer molecule was calculated using DFT (carried out by U. Aschauer at ETHZ) for varying distances between the polymer molecule and the surface. The L-J parameters for surface species (Al, O, hydroxyl O) were fitted to the energy of the supercell containing various conformational structures of polymer at varying distances from surface. Cross potential between alumina surface and polymer molecule were defined using the combination rule for L-J parameters.

To describe the interaction between water and the surface, two different approaches were used depending on the water potential in order to maintain the compatibility of the force field. With TIP3P potential for water, cross potentials were described by L-J parameters derived earlier for the surface and TIP3P L-J parameters for water. While with the De Leeuw and Parker potential, surface-water interactions were taken from their work on iron-oxyhydroxide with scaled Al-Ow Buckingham potential parameters. Detailed force field parameters are given in annex 2.

For the simulation (00.1) surface slabs were generated and hydroxylated using METADISE. PAA molecules with 10 monomer units were added manually on top of the surface. The simulation cell containing PAA and surface was equilibrated at 10K. Thereafter, the empty space in the simulation cell was filled up with water leaving a vacuum of 20 Å on top of the simulation cell. All the atoms in the alumina slab were allowed to relax during the MD run, which was not done in the previous MD simulation study [158]. MD simulation was conducted at 300 K with NVT Hoover isotherm with a relaxation time of 0.5 ps and time step of 0.2 fs. The simulation cell was equilibrated at 300K for 50K steps before starting the MD run.

MD simulations were done for surfaces in vacuum as well as surface in water. MD simulations run does not show any abnormal behavior with surface in vacuum. Figure 7.1 shows the different conformational arrangements of the PAA molecule on alumina (00.1) surface. As it can be seen there are no major distortions in the surface atomic structures and the polymer-alumina cross potentials seems to work well for the system. These calculations were run for only 400K steps (0.08 ns).

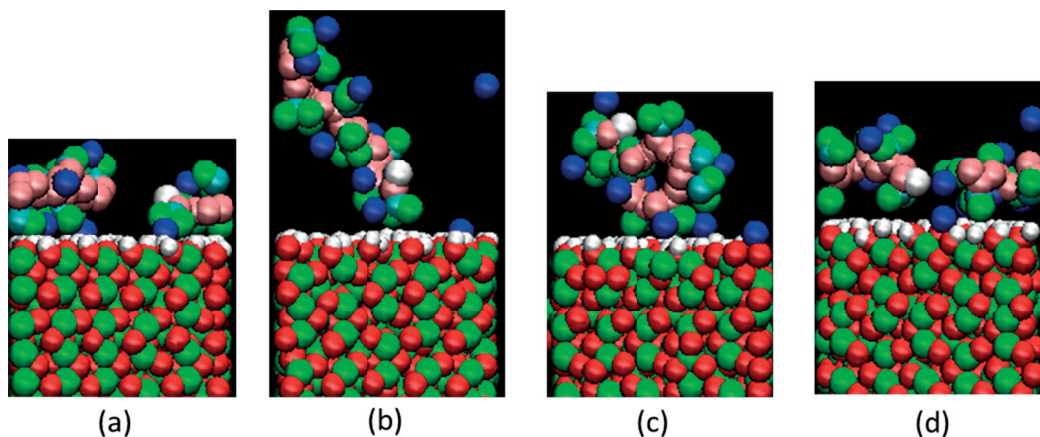


Figure 7.1. Conformations of the PAA molecule on hydroxylated alumina surface in vacuum at (a) $t=0$, (b) $t=0.017$ ns (tail configurations), (c) $t=0.059$ ns (loop configurations), and (d) $t=0.069$ ns (train configuration). Green atoms in the polymer molecule are hydroxyl O, pink are the backbone carbon atoms, blue are Na counter ions.

The MD simulations with water, using TIP3P water as well as De Leeuw water, show that (00.1) hydroxylated surface is not stable in water (Figure 7.2). While OH molecules detach from the surface with De Leeuw water, Al atoms leave the surface in TIP3P water. However, in a previous study [162] on stability of hydroxylated surfaces of alumina, hydroxylated surfaces were shown to be stable in vacuum. It shows that the surface-water interaction potential parameters are not adequate with both the water potentials. Simulations were run with interaction parameters of Dringen et al. [158], but the abnormal distortions and core-shell fusion of the surface oxygen atoms was observed.

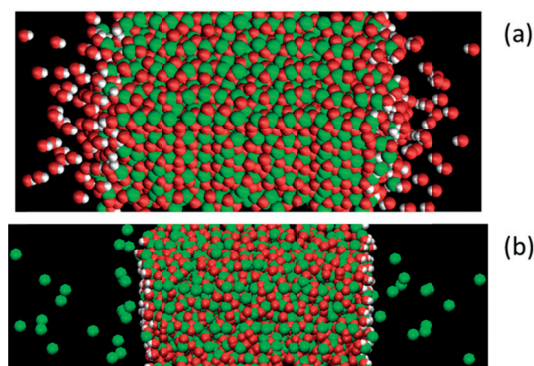


Figure 7.2. Unstable hydroxylated alumina surface in water, (a) hydroxyl atoms detach from the surface in MD simulations with De Leeuw water, while (b) Al atoms detach with TIP3P water. Al is green, H white and O atoms are in red.

However it should be noted here that the derived L-J parameters for the alumina surface species have very low value of epsilon of the order of 10^{-7} , which implies that the attractive part of the L-J potential is almost zero for the surface species. It might be working well for the alumina-polymer interaction since the surface-polymer interaction is dominated by the electrostatic potentials as has been reported in the literature [157,158]. Although methodology described by Dringen et al [158] works well for a fixed (i.e. frozen) alumina surface, it seems to be the main source of the error in the current approach with relaxing surfaces. Another approach to derive the cross potentials for surface species might be to use localized/specific description of the surface atoms as suggested by Heinz et al [167] to approach the physical reality at the surfaces. The Future work should be focused on developing the adequate force field for alumina-water interactions and thereafter, study of the adsorption behavior of commonly used dispersants and polymers on different alumina surfaces.

8. Conclusions & Outlook

The final chapter of the thesis gives my conclusions of the different aspects dealt within the thesis as well as an outlook towards the future. The chapter is arranged into 4 sections dealing first with cation segregation to surfaces and grain boundaries in alumina followed by anion segregation. This is the first time anion segregation at alumina interfaces has been treated with these methods. I then move on to treat the effects of Mg impurities of dopants on the diffusion of oxygen in bulk alumina, a key issue in answering the “conundrum” of diffusion in alumina. Attempts were made to set up the calculations for adsorption of dispersants on alumina surface; issues in the force field were identified. Finally the chapter is completed with a short outlook as to where the work carried out in this thesis can lead to in the future of atomistic modeling in ceramic oxide systems.

8.1. Cation Segregation

Segregation of cation dopants and anion impurities on alumina surfaces and grain boundaries (GBs) was studied using the energy minimization method. First, a detailed study of the segregation behavior was done on the coincidence site lattice (CSL) GBs (or twin GBs) in codoped (Y-La, La-Mg, Mg-Y) α -alumina. In addition, a general GB characterized using STEM-EDX analysis of transparent alumina samples, were also simulated using the near coincidence GB approach in order to link the experiments with the modeling and help validate the approach used in this work.

Segregation of the oversized cations was found to be energetically favorable for all the surfaces, GBs (CSL/general), doping combinations, and doping concentrations without any exception. However, codoping was found to be energetically more favorable than single doping only for the bivalent-trivalent combinations (La-Mg, Y-Mg) of the dopants on the twin GBs. The disparity in the ionic sizes and the availability of extra space due to the charge compensating oxygen vacancies were

found to be the key reasons for energetic gain. The segregation energy for the general GB was observed to be lower than the twin GBs which is not very intuitive given that the general GBs are more open and disordered in comparison to twin GBs and therefore, more available space for larger cations. But only few specific cation sites (25%) in the general GB region were found to be energetically favorable, whereas all the sites in the GB region were found to be conducive for the segregation in twin GBs. This suggests that grain boundary structure – coordination numbers and bonding also play a key role in the energetics. The effect of disparity in ionic sizes observed presents triple doping of alumina with different size cations, e.g. Mg-La-In, as an interesting proposition to explore in the future, to modify grain boundary composition, mobility and reduce grain growth - the ultimate goal of controlling microstructures from fundamental knowledge of what is happening at an atomistic level at the GBs.

Higher order GB complexion transitions were observed with increasing dopant concentration for twin GBs as well as the general GB, which will enhance the GB mobility and transport. An optimum dopant concentration of 4 atoms/nm² was identified to form the lowest order GB complexion (single layer adsorption) at the twin GBs, which produces solute pinning effect. General GB did not show any such GB complexion phase at any dopant concentration; but some of the lowest energy configurations might be missing due to the lower number of configurations calculated at each dopant concentration in this case. Therefore, more number of configurations needs to be calculated in order to resolve this issue as it is crucial in gaining a better understanding of optimum doping for grain growth control in the processing of transparent alumina. This is particularly the case as the majority of grain boundaries in a sintered alumina are expected to be general rather than CSL or twin type boundaries.

On one hand, presence of Mg encourages the creation of more favorable charge compensating O vacancies farther from the GB center region, increasing the bulk solubility and distribution of the trivalent dopant ions. On the other hand, higher coordination numbers of the trivalent dopants compared to the bivalent dopant shows the stronger covalent bonds between trivalent dopants and oxygen. Combination of these two factors can explain the enhanced GB strengthening of the codoped alumina than single doped alumina.

The present study of the codoping in alumina clearly identifies the different roles of the bivalent and trivalent dopant ions on the additional effects of the codoping in alumina, which will give better control over the microstructure and properties of alumina by exploiting specific effects of each dopant types. Enhanced understanding of the interplay between GB complexions and dopant concentration should lead to knowledge based grain boundary engineering in alumina. Finally, preliminary

calculations of the general GB done for the first time in alumina open up a new avenue for research which is more realistic and feasible given the ever increasing affordable computational power.

8.2. Anion Segregation

The issue of anion impurities in alumina was addressed for the first time in the present work. Atomistic modeling of the Cl segregation to the GBs and surfaces using energy minimization method together with the microstructural characterization of alumina GBs carried out in collaboration with an experimental group was able to show the effect of small amounts of Cl anion impurity on the alumina microstructure. Although small, probably around 200-300 ppm, the Cl contamination was similar to the dopant concentrations used to modify the sintering behavior. Higher order GB complexions were observed at even low Cl anion concentrations, which will enhance GB mobility and hence, promote the rapid grain growth. Also the higher coordination number of Cl-Al than O-Al suggests stronger adhesion of Cl on alumina surfaces, which makes it difficult to get rid of Cl at lower temperatures resulting in the possibility of having Cl entrapped in pores. Transparent alumina can ill afford both the artifacts: the rapid grain growth and the porous microstructure. Given the small margin for error in the production of advanced ceramics like transparent alumina, small modifications like these can bring tangible improvements in the performance. Therefore, anion impurities certainly need to be taken into account and experimental work needs to be conducted to verify the current findings, to try and eliminate some of the impurities

8.3. Oxygen Diffusion

The effect of Mg impurities on oxygen diffusion in alumina was studied in an attempt to reconcile the difference between experimental (~ 6 eV) and simulation activation energies (~ 2 eV) for oxygen diffusion in alumina. Combination of nudged elastic band and kinetic Monte Carlo methods was used to simulate the macroscopic diffusion of oxygen in alumina. The results were compared with the DFT results, which indicate a high error in the absolute values of the migration barriers. However, the general trends and the relative effect of Mg impurities were found to be coherent with different methods.

Substitutional Mg (Mg_{Al}) can form energetically favorable defect clusters with up to 3 oxygen vacancies (V_{O}), and with larger radii (>6 Å). The nearest neighbor V_{O} s were found to be most strongly bound with the Mg, with a binding energy of ~ 1.5 eV. Thus the presence of Mg_{Al} reduces the number of available mobile defects. Moreover, 2X higher migration barriers of jumps moving V_{O} away from Mg_{Al} and 4X lower migration barriers of the jumps moving V_{O} closer to Mg_{Al} , will kinetically favor the

large concentrations of V_{Os} around Mg_{Al} . Combining both the effects may account for an increase of 2-3 eV in the migration barriers of the diffusive jumps.

The presence of Mg and the increased vacancy-vacancy interaction due to clustering of defects causes destabilization of certain vacancy configurations. It will reduce the number of available diffusive pathways and thereby slow down the diffusion kinetics.

The conclusion of this study on Mg is that dopants and impurities can have a significant effect. Diffusion experiments carried out on “pure” alumina are not pure in the computational sense. Most of the experimental alumina samples contain 3 or 4 cation impurities at ppm level, which can have a significant effect as shown in the present work. Experiments are probably not looking at intrinsic diffusion in alumina but extrinsic because of the impurities. A more complex model which can deal with the higher length scale effects needs to be developed in order to capture the macroscopic effects of such cation impurities.

The effects of impurities are expected to be more significant in the grain boundary mass transport in polycrystalline alumina due to the increased concentration of cation dopants in the alumina GBs caused by the segregation of dopants. The present study lays down a guideline for the future research in the diffusion of alumina, whereby it is necessary to take into account the unavoidable cation impurities in alumina and to move towards simulating diffusion in grain boundaries where transport processes are likely to be modified the most.

8.4. Outlook

The atomistic modeling methods and techniques used in the present work are generic and can be applied to other problems in ceramic systems. Combination of nudged elastic band and kinetic Monte Carlo can be used to investigate the effect of other impurities on the oxygen diffusion in alumina. It can also be used to go one step further and simulate the oxygen diffusion in pure as well as doped alumina GBs. Kinetic Monte Carlo (KMC) simulations of pure and impurity containing alumina give identical results showing no effect of Mg on the macroscopic diffusion coefficient, possibly due to the fact that the effect of Mg has been taken into account only within a short cut off distance (6 Å). But it is very difficult to individually calculate the migration barrier of each jump for a long distance. Therefore, a fresh large scale approach is needed to take into account the long distance effects and artifacts due to the presence of the cation impurities.

With respect to segregation of dopants at grain boundaries more work needs to be done on more general grain boundaries to see how close the twin GBs that are less computationally expensive represent the more general behavior of GBs. The near

coincidence GB approach should be used in combination with molecular dynamics simulation method in order to get more accurate values for the segregation energies. Modeling of the triple doped grain boundaries should be an interesting topic to explore in the future as experimentally there is definitely an advantage but little or no high resolution analytical TEM has yet been carried out on such triple doped systems.

After the grain boundary segregation simulations the effect of anions can be at least as important as the controlled doping with cations. This leads to the need for an Experimental study to be done to understand the effect of anion impurities (Chlorides and sulphates) on the microstructure and properties of alumina. The simulations suggest it is very negative. Chlorine impurities can be removed from surfaces by washing with H_2O_2 solutions. Therefore, a comparative study on sintering and microstructural properties of as received and H_2O_2 treated alumina powder can be conducted.

In the end present work also demonstrates the strength and benefits of the atomistic modeling in the field of ceramics processing. It can help ceramic community in accessing length and time scales which were previously not possible using the experimental methods alone. It does not only help explaining fundamental mechanisms behind experimental observation but helps direct experimentalist towards experimental regions not thought about. The ultimate goal of the design of new materials and methods based on knowledge based approach is rapidly approaching and such simulations will play a greater and greater role in materials design and development in the future.

A1. DFT Calculation of Migration Barriers

DFT calculations were carried out using the Quantum ESPRESSO package [168] using ultra-soft pseudo-potentials [169] with Al 3s, 3p and O 2s, 2p as valence states. We employed the gradient corrected PBE [170] functional and expanded wave functions in plane-waves up to the kinetic energy of 25 Ry in conjunction with 200 Ry for the augmented density. Calculations were performed in a 2x2x1 supercell (120 atoms) of the hexagonal unit-cell and reciprocal space was sampled using a 4x4x2 gamma centered mesh. For calculations with vacancies, a total charge of +2e was imposed via a uniform background charge. This corresponds to removing the two extra electrons together with the oxygen atom, which is the situation in the classical calculations. We want to note that calculations without this charge adjustment result in much larger migration energies of ~4.3 eV for class 3 jumps, which is in agreement with other DFT calculations performed using the unadjusted setup [171]. Due to the computational cost, only 5 intermediate images were used for DFT NEB calculations.

A2. Force Field Parameters

A2.1. Lewis-Catlow Potential for Alumina

Potential

SPEC

O CORE 0.21

O SHEL -2.21

AL CORE 3.00

Y CORE 3.00

LA CORE 3.00

MG CORE 2.00

ENDS

BUCK

AL CORE O SHEL 1114.9 0.3118 0.0

Y CORE O SHEL 1345.1 0.3491 0.0

O SHEL O SHEL 22764.0 0.149 27.88

LA CORE O SHEL 1439.7 0.3651 0.0

MG CORE O SHEL 1428.5 0.29453 0.0

ENDS

HARM O CORE O SHEL 27.29

ENDS

A2.2. Binks Potential for Alumina

SPEC

O CORE 0.04

O SHEL -2.04

AL CORE 3.0

CL CORE 0.984

CL SHEL -1.984

ENDS

```

BUCK
AL CORE O SHEL 1725.00000 0.289700 0.000000 0.00 10.00
CL SHEL CL SHEL 3296.57000 0.328900 107.7000 0.00 10.00
O SHEL O SHEL 9547.96000 0.219200 32.00000 0.00 10.00
O SHEL CL SHEL 8286.91000 0.258500 62.20000 0.00 10.00
AL CORE CL SHEL 4724.01730 0.336424 0.000000 0.00 10.00
ENDS
HARM O CORE O SHEL 6.3
HARM CL CORE CL SHEL 17.52
ENDS

```

A2.3. PAA-Alumina-Water (TIP3P) Force Field

units eV

molecules 6

SURFACE_Oxygen

nummols 1650

atoms 2

O 15.5000 0.210

O(S) 0.5000 -2.210

shell 1

1 2 27.2900

Finish

SURFACE_Al

nummols 1200

atoms 1

AL 27.0000 2.875

Finish

HYDROXY_OH

nummols 150

atoms 3

OH 15.500 0.900

OH(S) 0.500 -2.300

H 1.008 0.400

shell 1 1

1 2 74.9200

bonds 1

mors 2 3 7.0525 0.9258 3.1749

finish

PAA

NUMMOLS 1

ATOMS 50

```

T 15.0350000 0.0000000
X 14.0270000 -0.0300000
C1 12.0110000 0.3700000
A 15.9999999 -0.6700000
A 15.9999999 -0.6700000
X 14.0270000 -0.0000000
X 14.0270000 -0.0300000
C1 12.0110000 0.3700000
A 15.9999999 -0.6700000
A 15.9999999 -0.6700000
X 14.0270000 -0.0000000
X 14.0270000 -0.0300000
C1 12.0110000 0.3700000
A 15.9999999 -0.6700000
A 15.9999999 -0.6700000
X 14.0270000 -0.0000000
X 14.0270000 -0.0300000
C1 12.0110000 0.3700000
A 15.9999999 -0.6700000
A 15.9999999 -0.6700000
X 14.0270000 -0.0000000
X 14.0270000 -0.0300000
C1 12.0110000 0.3700000
A 15.9999999 -0.6700000
A 15.9999999 -0.6700000
X 14.0270000 -0.0000000
X 14.0270000 -0.0300000
C1 12.0110000 0.3700000
A 15.9999999 -0.6700000
A 15.9999999 -0.6700000
X 14.0270000 -0.0000000
X 14.0270000 -0.0300000
C1 12.0110000 0.3700000
A 15.9999999 -0.6700000
A 15.9999999 -0.6700000
X 14.0270000 -0.0000000

```

```

X 14.0270000 -0.0300000
C1 12.0110000 0.3700000
A 15.9999999 -0.6700000
A 15.9999999 -0.6700000
X 14.0270000 -0.0000000
X 14.0270000 -0.0300000
C1 12.0110000 0.3700000
A 15.9999999 -0.6700000
A 15.9999999 -0.6700000
X 14.0270000 -0.0000000
X 14.0270000 -0.0300000
C1 12.0110000 0.3700000
A 15.9999999 -0.6700000
A 15.9999999 -0.6700000
CONSTRAINTS 19
1 2 1.5300000
2 6 1.5300000
6 7 1.5300000
7 11 1.5300000
11 12 1.5300000
12 16 1.5300000
16 17 1.5300000
17 21 1.5300000
21 22 1.5300000
22 26 1.5300000
26 27 1.5300000
27 31 1.5300000
31 32 1.5300000
32 36 1.5300000
36 37 1.5300000
37 41 1.5300000
41 42 1.5300000
42 46 1.5300000
46 47 1.5300000
BONDS 30
harm 3 4 65.08991035 1.220000
harm 3 5 65.08991035 1.220000
harm 8 9 65.08991035 1.220000
harm 8 10 65.08991035 1.220000
harm 13 14 65.08991035 1.220000
harm 13 15 65.08991035 1.220000

```

A2. Force field parameters

harm	18	19	65.08991035	1.220000
harm	18	20	65.08991035	1.220000
harm	23	24	65.08991035	1.220000
harm	23	25	65.08991035	1.220000
harm	28	29	65.08991035	1.220000
harm	28	30	65.08991035	1.220000
harm	33	34	65.08991035	1.220000
harm	33	35	65.08991035	1.220000
harm	38	39	65.08991035	1.220000
harm	38	40	65.08991035	1.220000
harm	43	44	65.08991035	1.220000
harm	43	45	65.08991035	1.220000
harm	48	49	65.08991035	1.220000
harm	48	50	65.08991035	1.220000
harm	2	3	27.43846194	1.522000
harm	7	8	27.43846194	1.522000
harm	12	13	27.43846194	1.522000
harm	17	18	27.43846194	1.522000
harm	22	23	27.43846194	1.522000
harm	27	28	27.43846194	1.522000
harm	32	33	27.43846194	1.522000
harm	37	38	27.43846194	1.522000
harm	42	43	27.43846194	1.522000
harm	47	48	27.43846194	1.522000
ANGLES	48			
harm	4	3	5	4.339534643 123.0000000
harm	9	8	10	4.339534643 123.0000000
harm	14	13	15	4.339534643 123.0000000
harm	19	18	20	4.339534643 123.0000000
harm	24	23	25	4.339534643 123.0000000
harm	29	28	30	4.339534643 123.0000000
harm	34	33	35	4.339534643 123.0000000
harm	39	38	40	4.339534643 123.0000000
harm	44	43	45	4.339534643 123.0000000
harm	49	48	50	4.339534643 123.0000000
harm	4	3	2	6.075555786 125.0000000
harm	9	8	7	6.075555786 125.0000000
harm	14	13	12	6.075555786 125.0000000
harm	19	18	17	6.075555786 125.0000000
harm	24	23	22	6.075555786 125.0000000
harm	29	28	27	6.075555786 125.0000000

```

harm 34 33 32 6.075555786 125.0000000
harm 39 38 37 6.075555786 125.0000000
harm 44 43 42 6.075555786 125.0000000
harm 49 48 47 6.075555786 125.0000000
harm 2 3 5 6.075555786 125.0000000
harm 7 8 10 6.075555786 125.0000000
harm 12 13 15 6.075555786 125.0000000
harm 17 18 20 6.075555786 125.0000000
harm 22 23 25 6.075555786 125.0000000
harm 27 28 30 6.075555786 125.0000000
harm 32 33 35 6.075555786 125.0000000
harm 37 38 40 6.075555786 125.0000000
harm 42 43 45 6.075555786 125.0000000
harm 47 48 50 6.075555786 125.0000000
harm 1 2 6 5.389438773 109.2800000
harm 2 6 7 5.389438773 109.2800000
harm 6 7 11 5.389438773 109.2800000
harm 7 11 12 5.389438773 109.2800000
harm 11 12 16 5.389438773 109.2800000
harm 12 16 17 5.389438773 109.2800000
harm 16 17 21 5.389438773 109.2800000
harm 17 21 22 5.389438773 109.2800000
harm 21 22 26 5.389438773 109.2800000
harm 22 26 27 5.389438773 109.2800000
harm 26 27 31 5.389438773 109.2800000
harm 27 31 32 5.389438773 109.2800000
harm 31 32 36 5.389438773 109.2800000
harm 32 36 37 5.389438773 109.2800000
harm 36 37 41 5.389438773 109.2800000
harm 37 41 42 5.389438773 109.2800000
harm 41 42 46 5.389438773 109.2800000
harm 42 46 47 5.389438773 109.2800000
DIHEDRALS 118
cos 1 2 3 4 0.00542055 -180.000000 6.00000000 1.00000000 1.00000000
cos 1 2 3 5 0.00542055 -180.000000 6.00000000 1.00000000 1.00000000
cos 6 2 3 4 0.00542055 -180.000000 6.00000000 1.00000000 1.00000000
cos 6 2 3 5 0.00542055 -180.000000 6.00000000 1.00000000 1.00000000
cos 2 6 7 8 0.02168222 0.00000000 3.00000000 1.00000000 1.00000000
cos 2 6 7 11 0.02168222 0.00000000 3.00000000 1.00000000 1.00000000
cos 6 7 8 9 0.00542055 -180.000000 6.00000000 1.00000000 1.00000000
cos 6 7 8 10 0.00542055 -180.000000 6.00000000 1.00000000 1.00000000

```

A2. Force field parameters

```

cos 11 7 8 9 0.00542055 -180.000000 6.00000000 1.00000000 1.00000000
cos 11 7 8 10 0.00542055 -180.000000 6.00000000 1.00000000 1.00000000
cos 7 8 9 5 0.02168222 180.000000 2.00000000 1.00000000 1.00000000
cos 10 8 9 5 0.02168222 180.000000 2.00000000 1.00000000 1.00000000
cos 7 11 12 13 0.02168222 0.00000000 3.00000000 1.00000000 1.00000000
cos 7 11 12 16 0.02168222 0.00000000 3.00000000 1.00000000 1.00000000
cos 11 12 13 14 0.00542055 -180.0000 6.00000000 1.00000000 1.00000000
cos 11 12 13 15 0.00542055 -180.0000 6.00000000 1.00000000 1.00000000
cos 16 12 13 14 0.00542055 -180.0000 6.00000000 1.00000000 1.00000000
cos 16 12 13 15 0.00542055 -180.0000 6.00000000 1.00000000 1.00000000
cos 12 13 14 10 0.02168222 180.0000 2.00000000 1.00000000 1.00000000
cos 15 13 14 10 0.02168222 180.0000 2.00000000 1.00000000 1.00000000
cos 12 16 17 18 0.02168222 0.000000 3.00000000 1.00000000 1.00000000
cos 12 16 17 21 0.02168222 0.000000 3.00000000 1.00000000 1.00000000
cos 16 17 18 19 0.00542055 -180.0000 6.00000000 1.00000000 1.00000000
cos 16 17 18 20 0.00542055 -180.0000 6.00000000 1.00000000 1.00000000
cos 21 17 18 19 0.00542055 -180.0000 6.00000000 1.00000000 1.00000000
cos 21 17 18 20 0.00542055 -180.0000 6.00000000 1.00000000 1.00000000
cos 17 18 19 15 0.02168222 180.0000 2.00000000 1.00000000 1.00000000
cos 20 18 19 15 0.02168222 180.0000 2.00000000 1.00000000 1.00000000
cos 17 21 22 23 0.02168222 0.000000 3.00000000 1.00000000 1.00000000
cos 17 21 22 26 0.02168222 0.000000 3.00000000 1.00000000 1.00000000
cos 21 22 23 24 0.00542055 -180.0000 6.00000000 1.00000000 1.00000000
cos 21 22 23 25 0.00542055 -180.0000 6.00000000 1.00000000 1.00000000
cos 26 22 23 24 0.00542055 -180.0000 6.00000000 1.00000000 1.00000000
cos 26 22 23 25 0.00542055 -180.0000 6.00000000 1.00000000 1.00000000
cos 22 23 24 20 0.02168222 180.0000 2.00000000 1.00000000 1.00000000
cos 25 23 24 20 0.02168222 180.0000 2.00000000 1.00000000 1.00000000
cos 22 26 27 28 0.02168222 0.000000 3.00000000 1.00000000 1.00000000
cos 22 26 27 31 0.02168222 0.000000 3.00000000 1.00000000 1.00000000
cos 26 27 28 29 0.00542055 -180.0000 6.00000000 1.00000000 1.00000000
cos 26 27 28 30 0.00542055 -180.0000 6.00000000 1.00000000 1.00000000
cos 31 27 28 29 0.00542055 -180.0000 6.00000000 1.00000000 1.00000000
cos 31 27 28 30 0.00542055 -180.0000 6.00000000 1.00000000 1.00000000
cos 27 28 29 25 0.02168222 180.0000 2.00000000 1.00000000 1.00000000
cos 30 28 29 25 0.02168222 180.0000 2.00000000 1.00000000 1.00000000
cos 27 31 32 33 0.02168222 0.000000 3.00000000 1.00000000 1.00000000
cos 27 31 32 36 0.02168222 0.000000 3.00000000 1.00000000 1.00000000
cos 31 32 33 34 0.00542055 -180.0000 6.00000000 1.00000000 1.00000000
cos 31 32 33 35 0.00542055 -180.0000 6.00000000 1.00000000 1.00000000
cos 36 32 33 34 0.00542055 -180.0000 6.00000000 1.00000000 1.00000000

```



```

cos 36 32 33 35 0.00542055 -180.0000 6.00000000 1.00000000 1.00000000
cos 32 33 34 30 0.02168222 180.0000 2.00000000 1.00000000 1.00000000
cos 35 33 34 30 0.02168222 180.0000 2.00000000 1.00000000 1.00000000
cos 32 36 37 38 0.02168222 0.000000 3.00000000 1.00000000 1.00000000
cos 32 36 37 41 0.02168222 0.000000 3.00000000 1.00000000 1.00000000
cos 36 37 38 39 0.00542055 -180.0000 6.00000000 1.00000000 1.00000000
cos 36 37 38 40 0.00542055 -180.0000 6.00000000 1.00000000 1.00000000
cos 41 37 38 39 0.00542055 -180.0000 6.00000000 1.00000000 1.00000000
cos 41 37 38 40 0.00542055 -180.0000 6.00000000 1.00000000 1.00000000
cos 37 38 39 35 0.02168222 180.0000 2.00000000 1.00000000 1.00000000
cos 40 38 39 35 0.02168222 180.0000 2.00000000 1.00000000 1.00000000
cos 37 41 42 43 0.02168222 0.000000 3.00000000 1.00000000 1.00000000
cos 37 41 42 46 0.02168222 0.000000 3.00000000 1.00000000 1.00000000
cos 41 42 43 44 0.00542055 -180.0000 6.00000000 1.00000000 1.00000000
cos 41 42 43 45 0.00542055 -180.0000 6.00000000 1.00000000 1.00000000
cos 46 42 43 44 0.00542055 -180.0000 6.00000000 1.00000000 1.00000000
cos 46 42 43 45 0.00542055 -180.0000 6.00000000 1.00000000 1.00000000
cos 42 43 44 40 0.02168222 180.0000 2.00000000 1.00000000 1.00000000
cos 45 43 44 40 0.02168222 180.0000 2.00000000 1.00000000 1.00000000
cos 42 46 47 48 0.04336445 0.000000 3.00000000 1.00000000 1.00000000
cos 46 47 48 49 0.02168222 -180.0000 6.00000000 1.00000000 1.00000000
cos 46 47 48 50 0.02168222 -180.0000 6.00000000 1.00000000 1.00000000
cos 47 48 49 45 0.02168222 180.0000 2.00000000 1.00000000 1.00000000
cos 50 48 49 45 0.02168222 180.0000 2.00000000 1.00000000 1.00000000
cos 2 3 5 9 0.02168222 180.000000 2.00000000 1.00000000 1.00000000
cos 4 3 5 9 0.02168222 180.000000 2.00000000 1.00000000 1.00000000
cos 7 8 10 14 0.02168222 180.000000 2.00000000 1.00000000 1.00000000
cos 9 8 10 14 0.02168222 180.000000 2.00000000 1.00000000 1.00000000
cos 12 13 15 19 0.02168222 180.0000 2.00000000 1.00000000 1.00000000
cos 14 13 15 19 0.02168222 180.0000 2.00000000 1.00000000 1.00000000
cos 17 18 20 24 0.02168222 180.0000 2.00000000 1.00000000 1.00000000
cos 19 18 20 24 0.02168222 180.0000 2.00000000 1.00000000 1.00000000
cos 22 23 25 29 0.02168222 180.0000 2.00000000 1.00000000 1.00000000
cos 24 23 25 29 0.02168222 180.0000 2.00000000 1.00000000 1.00000000
cos 27 28 30 34 0.02168222 180.0000 2.00000000 1.00000000 1.00000000
cos 29 28 30 34 0.02168222 180.0000 2.00000000 1.00000000 1.00000000
cos 32 33 35 39 0.02168222 180.0000 2.00000000 1.00000000 1.00000000
cos 34 33 35 39 0.02168222 180.0000 2.00000000 1.00000000 1.00000000
cos 37 38 40 44 0.02168222 180.0000 2.00000000 1.00000000 1.00000000
cos 39 38 40 44 0.02168222 180.0000 2.00000000 1.00000000 1.00000000
cos 42 43 45 49 0.02168222 180.0000 2.00000000 1.00000000 1.00000000

```

A2. Force field parameters

```

cos  44  43  45  49  0.02168222  180.0000  2.00000000  1.00000000  1.00000000
cos   1   2   6   7  0.02168222  0.00000000  3.00000000  1.00000000  1.00000000
cos   3   2   6   7  0.02168222  0.00000000  3.00000000  1.00000000  1.00000000
cos   3   5   9   8  0.21682287  180.000000  2.00000000  1.00000000  1.00000000
cos   6   7  11  12  0.02168222  0.00000000  3.00000000  1.00000000  1.00000000
cos   8   7  11  12  0.02168222  0.00000000  3.00000000  1.00000000  1.00000000
cos   8  10  14  13  0.21682287  180.000000  2.00000000  1.00000000  1.00000000
cos  11  12  16  17  0.02168222  0.000000  3.00000000  1.00000000  1.00000000
cos  13  12  16  17  0.02168222  0.000000  3.00000000  1.00000000  1.00000000
cos  13  15  19  18  0.21682287  180.0000  2.00000000  1.00000000  1.00000000
cos  16  17  21  22  0.02168222  0.000000  3.00000000  1.00000000  1.00000000
cos  18  17  21  22  0.02168222  0.000000  3.00000000  1.00000000  1.00000000
cos  18  20  24  23  0.21682287  180.0000  2.00000000  1.00000000  1.00000000
cos  21  22  26  27  0.02168222  0.000000  3.00000000  1.00000000  1.00000000
cos  23  22  26  27  0.02168222  0.000000  3.00000000  1.00000000  1.00000000
cos  23  25  29  28  0.21682287  180.0000  2.00000000  1.00000000  1.00000000
cos  26  27  31  32  0.02168222  0.000000  3.00000000  1.00000000  1.00000000
cos  28  27  31  32  0.02168222  0.000000  3.00000000  1.00000000  1.00000000
cos  28  30  34  33  0.21682287  180.0000  2.00000000  1.00000000  1.00000000
cos  31  32  36  37  0.02168222  0.000000  3.00000000  1.00000000  1.00000000
cos  33  32  36  37  0.02168222  0.000000  3.00000000  1.00000000  1.00000000
cos  33  35  39  38  0.21682287  180.0000  2.00000000  1.00000000  1.00000000
cos  36  37  41  42  0.02168222  0.000000  3.00000000  1.00000000  1.00000000
cos  38  37  41  42  0.02168222  0.000000  3.00000000  1.00000000  1.00000000
cos  38  40  44  43  0.21682287  180.0000  2.00000000  1.00000000  1.00000000
cos  41  42  46  47  0.02168222  0.000000  3.00000000  1.00000000  1.00000000
cos  43  42  46  47  0.02168222  0.000000  3.00000000  1.00000000  1.00000000
cos  43  45  49  48  0.21682287  180.0000  2.00000000  1.00000000  1.00000000
INVERSIONS   10
plan   3   2   4   5  1.73457829  0.00000000
plan   8   7   9  10  1.73457829  0.00000000
plan  13  12  14  15  1.73457829  0.00000000
plan  18  17  19  20  1.73457829  0.00000000
plan  23  22  24  25  1.73457829  0.00000000
plan  28  27  29  30  1.73457829  0.00000000
plan  33  32  34  35  1.73457829  0.00000000
plan  38  37  39  40  1.73457829  0.00000000
plan  43  42  44  45  1.73457829  0.00000000
plan  48  47  49  50  1.73457829  0.00000000
finish

```

NA_COUNTERIONS

nummols 10

atoms 1

NA 22.990 1.0000

Finish

WATER (TIP3P)

nummols 1158

atoms 3

OW 15.8000 -0.834

HW 1.0080 0.417

HW 1.0080 0.417

bonds 2

harm 1 2 23.9907488 0.9572

harm 1 3 23.9907488 0.9572

angles 1

harm 2 1 3 4.3382909 104.52

finish

vdw 48

AL O(S) buck 1114.9000 0.31180 0.0000

AL OH(S) buck 771.4000 0.31180 0.0000

AL OW lj 0.0000699632544 1.670688

O(S) O(S) buck 22764.0000 0.14900 27.8800

O(S) OH(S) buck 22764.3000 0.14900 13.9400

O(S) OW buck 22764.3000 0.14900 15.4600

O(S) H buck 396.2700 0.2500 0.0000

O(S) HW buck 396.2700 0.2500 0.0000

OH(S) OH(S) buck 22764.3000 0.1490 6.9700

OH(S) OW buck 22764.3000 0.14900 15.4600

OH(S) H buck 311.9700 0.2500 0.0000

OH(S) HW buck 311.9700 0.2500 0.0000

OW OW 12-6 25246.0590 25.8052 12.0000 6.0000

OW H buck 396.2700 0.2500 0.0000

H H mors 0.0000 1.5000 2.8405 1.1520

H HW mors 0.0000 1.5000 2.8405 1.2009

HW HW mors 0.0000 1.5000 2.8405 2.5040

O(S) T lj 0.0003095905362 1.932911

O(S) X lj 0.0003008556635 2.024411

O(S) C1 lj 0.0002101219686 1.844711

O(S) A lj 0.0002756145150 1.577411

A2. Force field parameters

```
OH(S) T   lj  0.0000141060247  6.026665
OH(S) X   lj  0.0000137080334  6.118165
OH(S) C1  lj  0.0000095738898  5.938465
OH(S) A   lj  0.0000125579587  5.671165
AL  T   lj  0.0000698256496  1.965383
AL  X   lj  0.0000678555695  2.056883
AL  C1  lj  0.0000473913160  1.877183
AL  A   lj  0.0000621626319  1.609883
OW  T   lj  0.0065828472425  3.445305
OW  X   lj  0.0063971169763  3.536805
OW  C1  lj  0.0044678394832  3.357105
OW  A   lj  0.0058604125060  3.089805
NA  O(S) buck 1226.840  0.3065  0.0000
NA  OH(S) buck 858.790  0.3065  0.0000
NA  OW buck 2334.720  0.2387  0.0000
T   T   lj  0.0065699  3.7400000
T   X   lj  0.0064268  3.8230000
T   A   lj  0.0058876  3.3845000
T   C1  lj  0.0049707  3.6518000
X   X   lj  0.0062044  3.9230000
X   A   lj  0.0056837  3.4760000
X   C1  lj  0.0043416  3.7433000
C1  C1  lj  0.0030264  3.5636000
C1  A   lj  0.0039767  3.2963000
A   A   lj  0.0052070  3.0290000
C1  NA  lj  0.0039767  2.9998000
A   NA  buck 410.99000  0.3065000  0.000000
close
```

A2.4. PAA-Alumina-Water (De Leeuw) Force Field

The potential parameters for intra polymer and intra surface interactions remain the same. Only cross potentials and the water potential parameters are listed below.

WATER (De Leeuw & Parker)

nummols 1592

atoms 4

OW 15.5000 1.250

OW(S) 0.5000 -2.050

HW 1.0080 0.400

HW 1.0080 0.400

shell 1 1

```

1 2 209.4496
bonds 8
mors 2 3 6.203713 0.923670 2.220030
mors 2 4 6.203713 0.923670 2.220030
mors 3 4 0.000000 1.500000 2.840499
coul 2 3 0.5
coul 2 4 0.5
coul 3 4 0.5
coul 1 3 1.0
coul 1 4 1.0
angles 1
harm 3 2 4 4.19978 108.693195
finish

vdw 46
AL O(S) buck 1460.300 0.2991 0.0
AL OH(S) buck 1022.300 0.2991 0.0
AL OW(S) buck 584.300 0.2991 0.0
O(S) O(S) buck 22764.3000 0.1490 27.88
O(S) OH(S) buck 22764.3000 0.1490 13.94
O(S) OW(S) buck 22764.3000 0.1490 15.46
O(S) H buck 396.2700 0.2500 0.00
OH(S) OH(S) buck 22764.3000 0.1490 6.97
OH(S) OW(S) buck 22764.3000 0.1490 15.46
OH(S) H buck 311.9700 0.2500 0.00
HW O(S) buck 396.27 0.2500 0.00
HW OH(S) buck 311.9700 0.2500 0.00
OW(S) OW(S) 12-6 39344.9800 42.15 12.0000 6.0000
OW(S) HW buck 396.27 0.2500 0.0
OW(S) H buck 396.27 0.2500 0.0
#OW(S) H 12-6 24.0000 6.00 9.0000 6.0000
#OW(S) HW 12-6 24.0000 6.00 9.0000 6.0000
O(S) T lj 0.0001824963711 1.92043800000000
O(S) X lj 0.0001773473682 2.01193800000000
O(S) C1 lj 0.0001238619798 1.83223800000000
O(S) A lj 0.0001624683023 1.56493800000000
OH(S) T lj 0.0000012953555 7.49980000000000
OH(S) X lj 0.0000012588080 7.59130000000000
OH(S) C1 lj 0.0000008791698 7.41160000000000
OH(S) A lj 0.0000011531967 7.14430000000000
AL T lj 0.0000555793294 1.94867000000000

```

A2. Force field parameters

```

AL  X  lj  0.0000540111989  2.0401700000000
AL  C1 lj  0.0000377222064  1.8604700000000
AL  A  lj  0.0000494797745  1.5931700000000
OW(S) T  lj  0.0007045108788  4.8304700000000
OW(S) X  lj  0.0006846336147  4.9219700000000
OW(S) C1 lj  0.0004781580682  4.7422700000000
OW(S) A  lj  0.0006271943146  4.4749700000000
NA  O(S) buck 1226.840  0.3065  0.0000
NA  OH(S) buck 858.790  0.3065  0.0000
NA  OW(S) buck 2334.720  0.2387  0.0000
T  T  lj  0.0065699  3.7400000
T  X  lj  0.0064268  3.8230000
T  A  lj  0.0058876  3.3845000
T  C1 lj  0.0049707  3.6518000
X  X  lj  0.0062044  3.9230000
X  A  lj  0.0056837  3.4760000
X  C1 lj  0.0043416  3.7433000
C1  C1 lj  0.0030264  3.5636000
C1  A  lj  0.0039767  3.2963000
A  A  lj  0.0052070  3.0290000
C1  NA lj  0.0039767  2.9998000
A  NA buck 410.99000  0.3065000  0.000000
Close

```

References

- [1] R Coble, 'Transparent Alumina and Method of Preparation' (US Patent Office, 1962), <http://www.google.com/patents?id=6NRtAAAAEBAJ&dq=3026210>.
- [2] A Krell et al., 'Transparent Sintered Corundum with High Hardness and Strength', *Journal of the American Ceramic Society* 86, no. 1 (2003): 12–18.
- [3] R Apetz and Michel P. B. Bruggen, 'Transparent Alumina: A Light-Scattering Model', *Journal of the American Ceramic Society* 86, no. 3 (2003): 480–486.
- [4] N Roussel et al., 'Highly Dense, Transparent α -Al₂O₃ Ceramics from Ultrafine Nanoparticles via a Standard SPS Sintering', *Journal of the American Ceramic Society* (2013).
- [5] M Stuer et al., 'Transparent Polycrystalline Alumina Using Spark Plasma Sintering: Effect of Mg, Y and La Doping', *Journal of the European Ceramic Society* 30, no. 6 (2010): 1335–1343.
- [6] BN Kim et al., 'Spark Plasma Sintering of Transparent Alumina', *Scripta Materialia* 57, no. 7 (2007): 607–610.
- [7] M Suárez et al., 'Grain Growth Control and Transparency in Spark Plasma Sintered Self-doped Alumina Materials', *Scripta Materialia* 61, no. 10 (2009): 931–934.
- [8] JGJ Peelen and R Metselaar, 'Light Scattering by Pores in Polycrystalline Materials: Transmission Properties of Alumina', *Journal of Applied Physics* 45, no. 1 (1974): 216.
- [9] M Stuer et al., 'Nanopore Characterization and Optical Modeling of Transparent Polycrystalline Alumina', *Advanced Functional Materials* 22, no. 11 (2012): 2303–2309.
- [10] C Pecharrromán et al., 'On the Transparency of Nanostructured Alumina: Rayleigh-Gans Model for Anisotropic Spheres', *Optics Express* 17, no. 8 (2009): 6899–6912.
- [11] Q Yang et al., 'Effect of La₂O₃ on Microstructure and Transmittance of Transparent Alumina Ceramics', *Journal of Rare Earths* 24, no. 1 (2006): 72–75.
- [12] J Cheng et al., 'Microwave Sintering of Transparent Alumina', *Materials Letters* 56, no. 4 (2002): 587–592.
- [13] H Schmidt et al., 'Synthesis and Processing of Nanoscaled Ceramics by Chemical Routes', *Le Journal de Physique IV* 03, no. C7 (1993): 10.
- [14] A Krell et al., 'Processing of High-Density Submicrometer Al₂O₃ for New Applications', *Journal of the American Ceramic Society* 86, no. 4 (2003): 546–53.
- [15] A Krell and J Klimke, 'Effects of the Homogeneity of Particle Coordination on Solid-State Sintering of Transparent Alumina', *Journal of the American Ceramic Society* 89, no. 6 (2006): 1985–1992.

-
- [16] A Krell, T Hutzler, and J Klimke, 'Transmission Physics and Consequences for Materials Selection, Manufacturing, and Applications', *Journal of the European Ceramic Society* 29, no. 2 (2009): 207–221.
- [17] P Bowen et al., 'Colloidal Processing and Sintering of Nanosized Transition Aluminas', *Powder Technology* 157, no. 1–3 (29 September 2005): 100–107.
- [18] G Tari, JMF Ferreira, and O Lyckfeldt, 'Influence of Magnesia on Colloidal Processing of Alumina', *Journal of the European Ceramic Society* 17, no. 11 (1997): 1341–1350.
- [19] P Biswas et al., 'Transparent Sub-micrometre Alumina from Lanthanum Oxide Doped Common Grade Alumina Powder', *Ceramics International* (2013).
- [20] A Krell, J Klimke, and T Hutzler, 'Advanced Spinel and Sub- μm Al_2O_3 for Transparent Armour Applications', *Journal of the European Ceramic Society* 29, no. 2 (2009): 275–281.
- [21] J Fang et al., 'Effect of Yttrium and Lanthanum on the Final-Stage Sintering Behavior of Ultrahigh-Purity Alumina', *Journal of the American Ceramic Society* 80, no. 8 (1997): 2005–2012.
- [22] GB Granger, C Guizard, and A Addad, 'Influence of Co-Doping on the Sintering Path and on the Optical Properties of a Submicronic Alumina Material', *Journal of the American Ceramic Society* 91, no. 5 (2008): 1703–1706.
- [23] S Lartigue and F Dupau, 'Grain Boundary Behavior in Superplastic Mg-doped Alumina with Ytria Codoping', *Acta Metallurgica Et Materialia* 42, no. 1 (1994): 293–302.
- [24] YZ Li et al., 'Codoping of Alumina to Enhance Creep Resistance', *Journal of the American Ceramic Society* 82, no. 6 (1999): 1497–1504.
- [25] J Cho et al., 'Effect of Yttrium and Lanthanum on the Tensile Creep Behavior of Aluminum Oxide', *Journal of the American Ceramic Society* 80, no. 4 (1997): 1013–1017.
- [26] M Stuer, PhD thesis (2012), Institute of Materials Science, École polytechnique fédérale de Lausanne.
- [27] P Bowen et al., 'Colloidal Processing of Nanoceramic Powders for Porous Ceramic Film Applications', *Key Engineering Materials* 206–213 (2002): 1977–1980.
- [28] PC Hidber, TJ Graule, and LJ Gauckler, 'Citric Acid - A Dispersant for Aqueous Alumina Suspensions', *Journal of the American Ceramic Society* 79, no. 7 (1996): 1857–1867.
- [29] PC Hidber, TJ Graule, and LJ Gauckler, 'Influence of the Dispersant Structure on Properties of Electrostatically Stabilized Aqueous Alumina Suspensions', *Journal of the European Ceramic Society* 17, no. 2–3 (1997): 239–249.
- [30] J Koral, R Ullman, and FR Eirich, 'The Adsorption of Polyvinyl Acetate', *The Journal of Physical Chemistry* 62, no. 5 (1958): 541–550.

-
- [31] Z Pan, A Campbell, and P Somasundaran, 'Polyacrylic Acid Adsorption and Conformation in Concentrated Alumina Suspensions', *Colloids and Surfaces A: Physicochemical and Engineering Aspects* 191, no. 1–2 (2001): 71–78.
- [32] S Fabris and C Elsässer, 'First-principles Analysis of Cation Segregation at Grain Boundaries in α -Al₂O₃', *Acta Materialia* 51, no. 1 (2003): 71–86.
- [33] JP Buban et al., 'Grain Boundary Strengthening in Alumina by Rare Earth Impurities', *Science* 311, no. 5758 (2006): 212–215.
- [34] S Lartigue et al., 'Dislocation Activity and Differences Between Tensile and Compressive Creep of Yttria Doped Alumina', *Materials Science and Engineering A* 164, no. 1–2 (1993): 211–215.
- [35] S Lartigue, C Carry, and L Priester, 'Multiscale Aspects of the Influence of Yttrium on Microstructure, Sintering and Creep of Alumina', *Journal of the European Ceramic Society* 22, no. 9–10 (2002): 1525–1541.
- [36] AH Heuer, 'Oxygen and Aluminum Diffusion in [alpha]-Al₂O₃: How Much Do We Really Understand?', *Journal of the European Ceramic Society* 28, no. 7 (2008): 1495–1507.
- [37] C Catlow et al., 'Defect Energetics in α -Al₂O₃ and Rutile TiO₂', *Physical Review B* 25, no. 2 (1982): 1006–1026.
- [38] PWM Jacobs and EA Kotomin, 'Defect Energies for Pure Corundum and for Corundum Doped with Transition Metal Ions', *Philosophical Magazine A* 68, no. 4 (1993): 695.
- [39] KPD Lagerlöf AH Heuer, 'Oxygen Self-diffusion in Corundum (α -Al₂O₃): a Conundrum', *Philosophical Magazine Letters* 79, no. 8 (1999): 619.
- [40] H Jónsson, G Mills, and KW Jacobsen, 'Nudged Elastic Band Method for Finding Minimum Energy Paths of Transition', in *Classical and Quantum Dynamics in Condensed Phase Simulations* (World Scientific, 1998), 385–404.
- [41] PP Ewald, 'The Calculation of Optical and Electrostatic Grid Potential', *Annual Physics* 64 (1921): 253–287.
- [42] BG Dick and AW Overhauser, 'Theory of the Dielectric Constants of Alkali Halide Crystals', *Physical Review* 112, no. 1 (1958): 90–103.
- [43] TXT Sayle et al., 'Computer Simulation of Thin Film Heteroepitaxial Ceramic Interfaces Using a Near-coincidence-site Lattice Theory', *Philosophical Magazine A* 68, no. 3 (1993): 565–573.
- [44] JR Shewchuk, *An Introduction to the Conjugate Gradient Method Without the Agonizing Pain*, 1994.
- [45] JD Head and MC Zerner, 'A Broyden—Fletcher—Goldfarb—Shanno Optimization Procedure for Molecular Geometries', *Chemical Physics Letters* 122, no. 3 (6 December 1985): 264–270.
- [46] BJ Alder and TE Wainwright, 'Studies in Molecular Dynamics. I. General Method', *The Journal of Chemical Physics* 31, no. 2 (1 August 1959): 459–466.

-
- [47] Nicos S. Martys and Raymond D. Mountain, 'Velocity Verlet Algorithm for Dissipative-particle-dynamics-based Models of Suspensions', *Physical Review E* 59, no. 3 (1999): 3733–3736.
- [48] H Jónsson, G Mills, and KW Jacobsen, 'Nudged Elastic Band Method for Finding Minimum Energy Paths of Transition', in *Classical and Quantum Dynamics in Condensed Phase Simulations* (World Scientific, 1998), 385–404.
- [49] D Sheppard, R Terrell, and G Henkelman, 'Optimization Methods for Finding Minimum Energy Paths', *The Journal of Chemical Physics* 128, no. 13 (2008): 134106.
- [50] A Laio and M Parrinello, 'Escaping Free-energy Minima', *Proceedings of the National Academy of Sciences* 99, no. 20 (2002): 12562–12566.
- [51] A Ishii, H Kimizuka, and S Ogata, 'Multi-replica Molecular Dynamics Modeling', *Computational Materials Science* 54 (2012): 240–248.
- [52] N Metropolis et al., 'Equation of State Calculations by Fast Computing Machines', *The Journal of Chemical Physics* 21, no. 6 (1953): 1087–1092.
- [53] R Coble, 'Transparent Alumina and Method of Preparation' (US Patent Office, 1962), <http://www.google.com/patents?id=6NRtAAAAEBAJ&dq=3026210>.
- [54] BN Kim et al., 'Microstructure and Optical Properties of Transparent Alumina', *Acta Materialia* 57, no. 5 (2009): 1319–1326.
- [55] R Apetz and MPB Bruggen, 'Transparent Alumina: A Light-Scattering Model', *Journal of the American Ceramic Society* 86, no. 3 (2003): 480–486.
- [56] M Stuer et al., 'Transparent Polycrystalline Alumina Using Spark Plasma Sintering: Effect of Mg, Y and La Doping', *Journal of the European Ceramic Society* 30, no. 6 (April 2010): 1335–1343.
- [57] A Krell et al., 'Transparent Sintered Corundum with High Hardness and Strength', *Journal of the American Ceramic Society* 86, no. 1 (2003): 12–18.
- [58] A Krell et al., 'Processing of High-Density Submicrometer Al₂O₃ for New Applications', *Journal of the American Ceramic Society* 86, no. 4 (2003): 546–53.
- [59] GC Wei, 'Transparent Ceramic Lamp Envelope Materials', *Journal of Physics D: Applied Physics* 38, no. 17 (September 2005): 3057–3065.
- [60] JGJ Peelen and R Metselaar, 'Light Scattering by Pores in Polycrystalline Materials: Transmission Properties of Alumina', *Journal of Applied Physics* 45, no. 1 (1974): 216.
- [61] J Fang et al., 'Effect of Yttrium and Lanthanum on the Final-Stage Sintering Behavior of Ultrahigh-Purity Alumina', *Journal of the American Ceramic Society* 80, no. 8 (1997): 2005–2012.
- [62] S Fabris and C Elsässer, 'First-principles Analysis of Cation Segregation at Grain Boundaries in α -Al₂O₃', *Acta Materialia* 51, no. 1 (8 January 2003): 71–86.
- [63] JP Buban et al., 'Grain Boundary Strengthening in Alumina by Rare Earth Impurities', *Science* 311, no. 5758 (13 January 2006): 212–215.

-
- [64] YZ Li et al., 'Codoping of Alumina to Enhance Creep Resistance', *Journal of the American Ceramic Society* 82, no. 6 (1999): 1497–1504.
- [65] S Lartigue et al., 'Dislocation Activity and Differences Between Tensile and Compressive Creep of Yttria Doped Alumina', *Materials Science and Engineering A* 164, no. 1–2 (1993): 211–215.
- [66] S Lartigue-Korinek, C Carry, and L Priester, 'Multiscale Aspects of the Influence of Yttrium on Microstructure, Sintering and Creep of Alumina', *Journal of the European Ceramic Society* 22, no. 9–10 (September 2002): 1525–1541.
- [67] H Song and RL Coble, 'Morphology of Platelike Abnormal Grains in Liquid-Phase-Sintered Alumina', *Journal of the American Ceramic Society* 73, no. 7 (1990): 2086–2090.
- [68] H Song and RL Coble, 'Origin and Growth Kinetics of Platelike Abnormal Grains in Liquid-Phase-Sintered Alumina', *Journal of the American Ceramic Society* 73, no. 7 (1990): 2077–2085.
- [69] W Swiatnicki, S Lartigue-Korinek, and JY Laval, 'Grain Boundary Structure and Intergranular Segregation in Al₂O₃', *Acta Metallurgica Et Materialia* 43, no. 2 (1995): 795–805.
- [70] C Elsässer and T Elsässer, 'Codoping and Grain-Boundary Cosegregation of Substitutional Cations in α -Al₂O₃: A Density-Functional-Theory Study', *Journal of the American Ceramic Society* 88, no. 1 (2005): 1–14.
- [71] KL Gavrilov et al., 'Silica and Magnesia Dopant Distributions in Alumina by High-Resolution Scanning Secondary Ion Mass Spectrometry', *Journal of the American Ceramic Society* 82, no. 4 (1999): 1001–1008.
- [72] SJ Dillon, M P Harmer, and G S Rohrer, 'Influence of Interface Energies on Solute Partitioning Mechanisms in Doped Aluminas', *Acta Materialia* 58, no. 15 (September 2010): 5097–5108.
- [73] S Lartigue Korinek and F Dupau, 'Grain Boundary Behavior in Superplastic Mg-doped Alumina with Yttria Codoping', *Acta Metallurgica Et Materialia* 42, no. 1 (1994): 293–302.
- [74] J Cho et al., 'Influence of Yttrium Doping on Grain Misorientation in Aluminum Oxide', *Journal of the American Ceramic Society* 81, no. 11 (1998): 3001–3004.
- [75] J Cho et al., 'Modeling of Grain-Boundary Segregation Behavior in Aluminum Oxide', *Journal of the American Ceramic Society* 83, no. 2 (2000): 344–352.
- [76] J Cho et al., 'Role of Segregating Dopants on the Improved Creep Resistance of Aluminum Oxide', *Acta Materialia* 47, no. 15 (1999): 4197–4207.
- [77] SJ Dillon et al., 'Complexion: A New Concept for Kinetic Engineering in Materials Science', *Acta Materialia* 55, no. 18 (October 2007): 6208–6218.
- [78] M P Harmer, 'Interfacial Kinetic Engineering: How Far Have We Come Since Kingery's Inaugural Sosman Address?', *Journal of the American Ceramic Society* 93, no. 2 (2010): 301–317.

-
- [79] S Galmarini et al., 'Atomistic Simulation of Y-Doped γ -Alumina Interfaces', *Journal of the American Ceramic Society* 91, no. 11 (2008): 3643–3651.
- [80] S Galmarini et al., 'Atomistic Modeling of Dopant Segregation in α -alumina Ceramics: Coverage Dependent Energy of Segregation and Nominal Dopant Solubility', *Journal of the European Ceramic Society* 31, no. 15 (December 2011): 2839–2852.
- [81] GW Watson et al., 'Atomistic Simulation of Dislocations, Surfaces and Interfaces in MgO', *J. Chem. Soc., Faraday Trans.* 92, no. 3 (1 January 1996): 433–438.
- [82] BG Dick and AW Overhauser, 'Theory of the Dielectric Constants of Alkali Halide Crystals', *Physical Review* 112, no. 1 (1 October 1958): 90–103.
- [83] GV Lewis and CRA Catlow, 'Potential Models for Ionic Oxides', *Journal of Physics C: Solid State Physics* 18, no. 6 (28 February 1985): 1149–1161.
- [84] RS Liu et al., 'Crystal Structures and Peculiar Magnetic Properties of α - And γ -Al₂O₃ Powders', *Modern Physics Letters B* 11, no. 26–27 (1997): 1169–1174.
- [85] R Lizárraga et al., 'Structural Characterization of Amorphous Alumina and Its Polymorphs from First-principles XPS and NMR Calculations', *Physical Review B* 83, no. 9 (14 March 2011): 094201.
- [86] WC Mackrodt and PW Tasker, 'Segregation Isotherms at the Surfaces of Oxides', *Journal of the American Ceramic Society* 72, no. 9 (1989): 1576–1583.
- [87] P Masri et al., 'Entropy of Segregation of Isovalent Impurity Cations at the Surface of an Ionic Crystal: MgO(100)Ca²⁺', *Surface Science* 173, no. 2–3 (2 August 1986): 439–454.
- [88] J Cho et al., 'Influence of Yttrium Doping on Grain Misorientation in Aluminum Oxide', *Journal of the American Ceramic Society* 81, no. 11 (January 2005): 3001–3004.
- [89] GD West, JM Perkins, and MH Lewis, 'Characterisation of Fine-grained Oxide Ceramics', *Journal of Materials Science* 39, no. 22 (2004): 6687–6704.
- [90] S J Dillon and M P. Harmer, 'Demystifying the Role of Sintering Additives with "Complexion"', *Journal of the European Ceramic Society* 28, no. 7 (2008): 1485–1493.
- [91] N Shibata et al., 'Atomic-scale Imaging of Individual Dopant Atoms in a Buried Interface', *Nature Materials* 8, no. 8 (August 2009): 654–658.
- [92] R Apetz and MPB Bruggen, 'Transparent Alumina: A Light-Scattering Model', *Journal of the American Ceramic Society* 86, no. 3 (2003): 480–486.
- [93] A Krell et al., 'Processing of High-Density Submicrometer Al₂O₃ for New Applications', *Journal of the American Ceramic Society* 86, no. 4 (2003): 546–53.
- [94] RM Cannon, W. H. Rhodes, and A. H. Heuer, 'Plastic Deformation of Fine-Grained Alumina (Al₂O₃): I, Interface-Controlled Diffusional Creep', *Journal of the American Ceramic Society* 63, no. 1–2 (1980): 46–53.

-
- [95] DH Fan et al., 'Anion Impurities in Porous Alumina Membranes: Existence and Functionality', *Microporous and Mesoporous Materials* 100, no. 1–3 (23 March 2007): 154–159.
- [96] MH Leipold and CM Kapadia, 'Effect of Anions on Hot-Pressing of MgO', *Journal of the American Ceramic Society* 56, no. 4 (1973): 200–203.
- [97] R Dittmann, E Wintermantel, and T Graule, 'Sintering of Nano-sized Titania Particles and the Effect of Chlorine Impurities', *Journal of the European Ceramic Society* 33, no. 15–16 (December 2013): 3257–3264.
- [98] F Nabiei, Masters' Thesis (2013), Institute of Materials Science, EPFL, Switzerland.
- [99] T Nakagawa et al., 'Yttrium Doping Effect on Oxygen Grain Boundary Diffusion in [alpha]-Al₂O₃', *Acta Materialia* 55, no. 19 (November 2007): 6627–6633.
- [100] SJ Dillon and MP Harmer, 'Demystifying the Role of Sintering Additives with "Complexion"', *Journal of the European Ceramic Society* 28, no. 7 (2008): 1485–1493.
- [101] I Milas, B Hinnemann, and EA Carter, 'Structure of and Ion Segregation to an Alumina Grain Boundary: Implications for Growth and Creep', *Journal of Materials Research* 23, no. 05 (2008): 1494–1508.
- [102] AA Tsyganenko and PP Mardilovich, 'Structure of Alumina Surfaces', *Journal of the Chemical Society, Faraday Transactions* 92, no. 23 (1 January 1996): 4843–4852.
- [103] M Stuer et al., 'Nanopore Characterization and Optical Modeling of Transparent Polycrystalline Alumina', *Advanced Functional Materials* 22, no. 11 (2012): 2303–2309.
- [104] AH Heuer, 'Oxygen and Aluminum Diffusion in [alpha]-Al₂O₃: How Much Do We Really Understand?', *Journal of the European Ceramic Society* 28, no. 7 (2008): 1495–1507.
- [105] C Catlow et al., 'Defect Energetics in α -Al₂O₃ and Rutile TiO₂', *Physical Review B* 25, no. 2 (January 1982): 1006–1026.
- [106] PWM Jacobs and EA Kotomin, 'Defect Energies for Pure Corundum and for Corundum Doped with Transition Metal Ions', *Philosophical Magazine A* 68, no. 4 (1993): 695.
- [107] KPD LAGERLOF and AH HEUER, 'Oxygen Self-diffusion in Corundum (alpha-Al₂O₃): a Conundrum', *Philosophical Magazine Letters* 79, no. 8 (1999): 619.
- [108] KPD Lagerlöf and RW Grimes, 'The Defect Chemistry of Sapphire ([alpha]-Al₂O₃)', *Acta Materialia* 46, no. 16 (9 October 1998): 5689–5700.
- [109] U Aschauer, P Bowen, and SC Parker, 'Oxygen Vacancy Diffusion in Alumina: New Atomistic Simulation Methods Applied to an Old Problem', *Acta Materialia* 57, no. 16 (2009): 4765–4772.
- [110] KPR Reddy and AR Cooper, 'Oxygen Diffusion in Sapphire', *Journal of the American Ceramic Society* 65, no. 12 (1982): 634–638.

-
- [111] KPD Lagerlof, TE Mitchell, and AH Heuer, 'Lattice Diffusion Kinetics in Undoped and Impurity-Doped Sapphire (α -Al₂O₃): A Dislocation Loop Annealing Study', *Journal of the American Ceramic Society* 72, no. 11 (November 1989): 2159–2171.
- [112] H Haneda and C Monty, 'Oxygen Self-Diffusion in Magnesium- or Titanium-Doped Alumina Single Crystals', *Journal of the American Ceramic Society* 72, no. 7 (1 July 1989): 1153–1157.
- [113] RH Doremus, 'Diffusion in Alumina', *Journal of Applied Physics* 100, no. 10 (30 November 2006): 101301–101301–17.
- [114] H Yoshida, S Hashimoto, and T Yamamoto, 'Dopant Effect on Grain Boundary Diffusivity in Polycrystalline Alumina', *Acta Materialia* 53, no. 2 (10 January 2005): 433–440.
- [115] T Nakagawa et al., 'Yttrium Doping Effect on Oxygen Grain Boundary Diffusion in $[\alpha]$ -Al₂O₃', *Acta Materialia* 55, no. 19 (November 2007): 6627–6633.
- [116] T Matsudaira et al., 'Oxygen Permeability in Cation-doped Polycrystalline Alumina Under Oxygen Potential Gradients at High Temperatures', *Acta Materialia* 59, no. 14 (August 2011): 5440–5450.
- [117] S Galmarini et al., 'Atomistic Modeling of Dopant Segregation in A-alumina Ceramics: Coverage Dependent Energy of Segregation and Nominal Dopant Solubility', *Journal of the European Ceramic Society* 31, no. 15 (December 2011): 2839–2852.
- [118] A Tewari et al., 'Atomistic Modeling of the Effect of Codoping on the Atomistic Structure of Interfaces in A-alumina', *Journal of the European Ceramic Society* 32, no. 11 (August 2012): 2935–2948.
- [119] JH Harding, KJW Atkinson, and RW Grimes, 'Experiment and Theory of Diffusion in Alumina', *Journal of the American Ceramic Society* 86, no. 4 (April 2003): 554–59.
- [120] FG Will, HG DeLorenzi, and KH Janora, 'Conduction Mechanism of Single-Crystal Alumina', *Journal of the American Ceramic Society* 75, no. 2 (1992): 295–304.
- [121] D Prot and C Monty, 'Self-diffusion in α -Al₂O₃. II. Oxygen Diffusion in "undoped" Single Crystals', *Philosophical Magazine A* 73, no. 4 (1996): 899–917.
- [122] M Le Gall, B Lesage, and J Bernardini, 'Self-diffusion in α -Al₂O₃ I. Aluminium Diffusion in Single Crystals', *Philosophical Magazine A* 70, no. 5 (1994): 761.
- [123] A Laio and Michele Parrinello, 'Escaping Free-energy Minima', *Proceedings of the National Academy of Sciences* 99, no. 20 (10 January 2002): 12562–12566.
- [124] AF Voter, 'Introduction to the Kinetic Monte Carlo Method', *Radiation Effects* 235 (2005): 1–23, doi:10.1007/978-1-4020-5295-8_1.
- [125] BG Dick and AW Overhauser, 'Theory of the Dielectric Constants of Alkali Halide Crystals', *Physical Review* 112, no. 1 (1 October 1958): 90–103.
- [126] GV Lewis and CRA Catlow, 'Potential Models for Ionic Oxides', *Journal of Physics C: Solid State Physics* 18, no. 6 (28 February 1985): 1149–1161.

-
- [127] RS Liu et al., 'Crystal Structures and Peculiar Magnetic Properties of α - And γ - Al_2O_3 Powders', *Modern Physics Letters B* 11, no. 26–27 (1997): 1169–1174.
- [128] DJ Binks, Ph.D. thesis, University of Surrey, 1994.
- [129] JD Gale and AL Rohl, 'The General Utility Lattice Program (GULP)', *Molecular Simulation* 29, no. 5 (2003): 291–341.
- [130] ER Cope and MT Dove, 'Pair Distribution Functions Calculated from Interatomic Potential Models Using the *General Utility Lattice Program*', *Journal of Applied Crystallography* 40, no. 3 (15 May 2007): 589–594.
- [131] H Jónsson, G Mills, and KW Jacobsen, 'Nudged Elastic Band Method for Finding Minimum Energy Paths of Transition', in *Classical and Quantum Dynamics in Condensed Phase Simulations* (World Scientific, 1998), 385–404.
- [132] H Eyring, 'The Activated Complex in Chemical Reactions', *The Journal of Chemical Physics* 3, no. 2 (1 February 1935): 107–115.
- [133] E Wimmer et al., 'Temperature-dependent Diffusion Coefficients from Ab Initio Computations: Hydrogen, Deuterium, and Tritium in Nickel', *Physical Review B* 77, no. 13 (11 April 2008): 134305.
- [134] J Carrasco, N Lopez, and F Illas, 'First Principles Analysis of the Stability and Diffusion of Oxygen Vacancies in Metal Oxides', *Physical Review Letters* 93, no. 22 (24 November 2004): 225502.
- [135] Y Lei et al., 'Density Functional Calculation of Activation Energies for Lattice and Grain Boundary Diffusion in Alumina', *Physical Review B* 87, no. 21 (19 June 2013): 214105.
- [136] F Pietrucci et al., 'EPR G-tensor of Paramagnetic Centers in Yttria-stabilized Zirconia from First-principles Calculations', *Physical Review B* 73, no. 13 (21 April 2006): 134112.
- [137] F Pietrucci et al., 'Vacancy-vacancy Interaction and Oxygen Diffusion in Stabilized Cubic ZrO_2 from First Principles', *Physical Review B* 78, no. 9 (10 September 2008): 094301.
- [138] J. P. Bujan et al., 'Grain Boundary Strengthening in Alumina by Rare Earth Impurities', *Science* 311, no. 5758 (13 January 2006): 212–215.
- [139] Christian Elsässer and Traude Elsässer, 'Codoping and Grain-Boundary Cosegregation of Substitutional Cations in γ - Al_2O_3 : A Density-Functional-Theory Study', *Journal of the American Ceramic Society* 88, no. 1 (2005): 1–14.
- [140] Sandra Galmarini et al., 'Atomistic Simulation of Y-Doped α -Alumina Interfaces', *Journal of the American Ceramic Society* 91, no. 11 (2008): 3643–3651.
- [141] Abhishek Tewari et al., 'Atomistic Modeling of the Effect of Codoping on the Atomistic Structure of Interfaces in α -alumina', *Journal of the European Ceramic Society* 32, no. 11 (August 2012): 2935–2948.

-
- [142] S. Lartigue and L. Priester, 'INFLUENCE OF DOPING ELEMENTS ON THE GRAIN BOUNDARY CHARACTERISTICS IN ALUMINA', *Le Journal de Physique Colloques* 49, no. C5 (October 1988): C5-451-C5-456.
- [143] Danièle Bouchet, Frédéric Dupau, and Sylvie Lartigue-Korinek, 'Structure and Chemistry of Grain Boundaries in Yttria Doped Aluminas', *Microscopy Microanalysis Microstructures* 4, no. 6 (1993): 13 pages.
- [144] SYLVIE LARTIGUE and LOUISETTE PRIESTER, 'Grain Boundaries in Fine-Grained Magnesium-Doped Aluminas', *Journal of the American Ceramic Society* 71, no. 6 (1988): 430-437.
- [145] J. Cho et al., 'Influence of Yttrium Doping on Grain Misorientation in Aluminum Oxide', *Journal of the American Ceramic Society* 81, no. 11 (1998): 3001-3004.
- [146] S. Lartigue-Korinek, C. Carry, and L. Priester, 'Multiscale Aspects of the Influence of Yttrium on Microstructure, Sintering and Creep of Alumina', *Journal of the European Ceramic Society* 22, no. 9-10 (September 2002): 1525-1541.
- [147] Mehmet A. Gülgün, Valery Putlayev, and Manfred Rühle, 'Effects of Yttrium Doping [alpha]-Alumina: I, Microstructure and Microchemistry', *Journal of the American Ceramic Society* 82, no. 7 (1999): 1849-1856.
- [148] A. P. Sutton and R. W. Balluffi, *Interfaces in Crystalline Materials* (OUP Oxford, 1995).
- [149] Farhang Nabiei, Masters' Thesis (2013), Institute of Materials Science, EPFL, Switzerland.
- [150] N. Shibata et al., 'Atomic-scale Imaging of Individual Dopant Atoms in a Buried Interface', *Nature Materials* 8, no. 8 (August 2009): 654-658.
- [151] Shen J. Dillon and Martin P. Harmer, 'Demystifying the Role of Sintering Additives with "Complexion"', *Journal of the European Ceramic Society* 28, no. 7 (2008): 1485-1493.
- [152] C. M. Wang et al., 'Structural Features of Y-saturated and Supersaturated Grain Boundaries in Alumina', *Acta Materialia* 48, no. 10 (14 June 2000): 2579-2591.
- [153] M Palacios et al., 'Repulsion Forces of Superplasticizers on Ground Granulated Blast Furnace Slag in Alkaline Media, from AFM Measurements to Rheological Properties', *Materiales de Construcción* 62, no. 308 (26 November 2012): 489-513.
- [154] J Davies and JGP Binner 'The Role of Ammonium Polyacrylate in Dispersing Concentrated Alumina Suspensions', *Journal of the European Ceramic Society* 20, no. 10 (September 2000): 1539-1553.
- [155] H Kamiya et al., 'Effect of Polymer Dispersant Structure on Electrosteric Interaction and Dense Alumina Suspension Behavior', *Journal of the American Ceramic Society* 82, no. 12 (1999): 3407-3412.
- [156] P Bowen et al., 'Colloidal Processing and Sintering of Nanosized Transition Aluminas', *Powder Technology* 157, no. 1-3 (29 September 2005): 100-107.

-
- [157] GV Franks and Y Gan, 'Charging Behavior at the Alumina-Water Interface and Implications for Ceramic Processing', *Journal of the American Ceramic Society* 90, no. 11 (2007): 3373–3388.
- [158] R Dringen et al., 'Adsorption and Reduction of Glutathione Disulfide on α -Al₂O₃ Nanoparticles: Experiments and Modeling', *Langmuir* 27, no. 15 (2 August 2011): 9449–9457.
- [159] KK Das and P Somasundaran, 'Flocculation-dispersion Characteristics of Alumina Using a Wide Molecular Weight Range of Polyacrylic Acids', *Colloids and Surfaces A: Physicochemical and Engineering Aspects* 223, no. 1–3 (21 August 2003): 17–25.
- [160] PC Hidber, TJ Graule, and LJ Gauckler, 'Influence of the Dispersant Structure on Properties of Electrostatically Stabilized Aqueous Alumina Suspensions', *Journal of the European Ceramic Society* 17, no. 2–3 (1997): 239–249.
- [161] H Gocmez, 'The Interaction of Organic Dispersant with Alumina: A Molecular Modelling Approach', *Ceramics International* 32, no. 5 (2006): 521–525.
- [162] NH de Leeuw and Stephen C. Parker, 'Effect of Chemisorption and Physisorption of Water on the Surface Structure and Stability of alpha-Alumina', *Journal of the American Ceramic Society* 82, no. 11 (1999): 3209–2316.
- [163] SL Mayo, BD Olafson, WA Goddard, 'DREIDING: a Generic Force Field for Molecular Simulations', *The Journal of Physical Chemistry* 94, no. 26 (1 December 1990): 8897–8909.
- [164] WL Jorgensen et al., 'Comparison of Simple Potential Functions for Simulating Liquid Water', *The Journal of Chemical Physics* 79, no. 2 (15 July 1983): 926.
- [165] NH de Leeuw and SC Parker, 'Molecular-dynamics Simulation of MgO Surfaces in Liquid Water Using a Shell-model Potential for Water', *Physical Review B* 58, no. 20 (15 November 1998): 13901–13908.
- [166] S Kerisit and Stephen C Parker, 'Free Energy of Adsorption of Water and Metal Ions on the [1014] Calcite Surface', *Journal of the American Chemical Society* 126, no. 32 (18 August 2004): 10152–10161.
- [167] H Heinz et al., 'Force Field for Mica-Type Silicates and Dynamics of Octadecylammonium Chains Grafted to Montmorillonite', *Chemistry of Materials* 17, no. 23 (1 November 2005): 5658–5669.
- [168] P Giannozzi et al., 'QUANTUM ESPRESSO: a Modular and Open-source Software Project for Quantum Simulations of Materials', *Journal of Physics: Condensed Matter* 21, no. 39 (30 September 2009): 395502.
- [169] D Vanderbilt, 'Soft Self-consistent Pseudopotentials in a Generalized Eigenvalue Formalism', *Physical Review B* 41, no. 11 (15 April 1990): 7892–7895.
- [170] JP Perdew, K Burke, and M Ernzerhof, 'Generalized Gradient Approximation Made Simple', *Physical Review Letters* 77, no. 18 (28 October 1996): 3865–3868.

[171] E Wimmer et al., ‘Temperature-dependent Diffusion Coefficients from Ab Initio Computations: Hydrogen, Deuterium, and Tritium in Nickel’, *Physical Review B* 77, no. 13 (11 April 2008): 134305.

Abhishek Tewari

Graduate Student
Laboratory of Powder Technology
Institute of Materials Science
EPFL Switzerland

Phone : +41-78 67 67 254
Email: abhish1985@gmail.com
url: <http://people.epfl.ch/abhishek.tewari>
Nationality: Indian
Date of Birth: 19/05/85



Research Area

Atomistic Modelling, Transparent Ceramics, Tribology.

Education

- 2009 - 13 **Ph.D., EPFL** (École Polytechnique Fédérale de Lausanne, Switzerland) (Dr. Paul Bowen)
- Institute of Materials Science & Engineering
 - **Thesis:** Atomistic Modelling of Processing Issues for Transparent Polycrystalline Alumina
- 2007 - 09 **M.Tech., IIT Kanpur** (Indian Institute of Technology Kanpur, India) (Dr. Bikramjit Basu)
- Dept. of Materials Science & Engineering
 - **Thesis:** Analytical Models for Tribomechanical and Tribochemical Wear of Ceramics
 - CGPA: 9.7 / 10
- 2003 - 07 **B.Tech., IIT Kanpur**
- Dept. of Materials Science & Engineering

Publications

1. A Tewari, U Aschauer, P. Bowen, "Atomistic modeling of effect of Mg on oxygen vacancy diffusion in α -alumina." (under review).
2. "Grain boundary segregation of anion impurities and its effect on grain boundary atomistic structure" (under preparation)
3. "Atomistic modeling of cation doped α -alumina *general* grain boundaries" (under preparation)
4. A Tewari, "Load Dependence of Oxidative Wear in Metal/Ceramic Tribocouples in Fretting Environment", *WEAR* 289 (2012), 95-103.
5. A Tewari, S Galmarini, M Stuer, P Bowen, "Atomistic Modelling of the Effect of Codoping on the Atomistic Structure of Interfaces in α -Alumina", *Journal of the European Ceramic Society* 32 (2012), 2935-48.
6. F Bondioli, V Cannillo, A M Ferrari, A Tewari, "Synthesis and Thermal Stability of Hydroxyapatite-Coated Zirconia Nanocomposite Powders", *Synthesis and Reactivity in Inorganic, Metal-Organic, and Nano-Metal Chemistry* 42 (2012), 128-134.
7. S Galmarini, U Aschauer, A Tewari, Y Aman, C Van Gestel, P Bowen, "Atomistic modelling of dopant segregation in α -alumina ceramics: coverage dependent energy of segregation and nominal dopant solubility", *Journal of the European Ceramic Society* 31 (2011), 2839-2852.
8. A Tewari, B Basu, R Bordia, "Model for fretting wear of brittle ceramics", *Acta Materialia* 57 (2009), 2080-87.
9. A Dubey, S D Gupta, R Kumar, A Tewari, B Basu, "Time constant determination for electrical equivalent of biological cells", *Journal of Applied Physics* 105 (2009), 084705-1-8.

Atomistic Modelling Experience

- **Methods:** Molecular Statistics (Energy Minimization), Molecular Dynamics, Nudged Elastic Band, Metadynamics, Kinetic Monte Carlo.
- **Topics:** Surface/grain boundary segregation, defect calculations, solid state diffusion, surface adsorption, phonon frequency calculations, and force field development.
- **Simulation Packages:** DL POLY, GULP, Materials Studio.
- **Programming Language:** C/C++ (good), Java (intermediate).

Conferences and Workshops

- **Invited talk** on “Atomistic Modeling of the Role of Sintering Additives in the Processing of Transparent Polycrystalline α -Alumina” in 3rd international conference on alumina ALUMINAS-2013 in Kolkata, India (7-9 March, 2013).
- 3 oral presentations and 6 poster presentations in 8 international conferences and workshops across Europe, United States, Singapore and India including TMS-2012 and ICMAT-2011.

PhD Research Summary

Understanding the fundamental atomistic mechanisms pertaining to the synthesis of transparent polycrystalline alumina is the broad aim of my PhD thesis. The three main issues which my research work deals with are,

- Grain boundary segregation of dopants and anion impurities using energy minimization method.
- Solid state oxygen diffusion in alumina using combination of nudged elastic band/metadynamics and kinetic monte carlo.
- Adsorption of organic dispersants on alumina surfaces using molecular dynamics.

Teaching and Project Experience

2009-12 Teaching at EPFL

- Co-supervised a masters' thesis on TEM characterization of doped transparent alumina GB's.
- Lecturer, for 'Modelling of Materials' topic in masters' course on 'Powder Technology'.
- Teaching assistant for bachelor level course on 'Ceramic processing: classification, dispersion, pressing and slip casting' in 3 semesters.

2007-09 Teaching at IIT Kanpur

- Teaching assistant for 2 bachelor level courses ('Nature and Properties of Materials' and 'Manufacturing processes') in materials science department.
- Technical Assistant for operation of Scanning Electron Microscopy instrument (Autumn 2008).

May-July 2006 Summer Internship at University of Modena & Reggio Emilia, Italy (Dr. Federica Bondioli)

- Successfully developed the synthesis method for zirconia coated hydroxyapatite (HAp) nano composite powders for biomedical applications.
- Modified the ultrasonification step to achieve uniform distribution of the zirconia reinforcement by avoiding its uncontrolled agglomeration during the precipitation of HAp in presence of zirconia.

Academic Achievements

- Published a single author paper in *Wear* 289 (2012).
- Was offered the prestigious Felix scholarship for graduate studies at Oxford University in 2009.
- Stood 2nd in the masters' batch of materials science & engineering of 2009.

Extra-Curricular Activities

- General Secretary, Games & Sports Council, Students' Gymkhana, IIT Kanpur (2008-09).
- Captain, Institute athletics team, IIT Kanpur (2006-07).
- Chaired the organizing committee of biannual research day of doctoral school of materials science at EPFL in 2011.
- Won university level athletics competitions (100m, 200m, 400m, and hurdles)